MICROSTRUCTURAL EVOLUTION AND MECHANICAL BEHAVIOR IN NICKEL BASED ALLOYS FOR VERY HIGH TEMPERATURE REACTOR

BY

KUN MO

DISSERTATION

Submitted in partial fulfillment of the requirements
for the degree of Doctor of Philosophy in Nuclear Engineering
in the Graduate Collage of the
University of Illinois at Urbana-Champaign, 2011

Urbana, Illinois

Doctoral Committee:

Professor James F. Stubbins, Chair and Director of Research
Professor Brent J. Heuser
Professor Rizwan Uddin
Professor Pascal Bellon

ABSTRACT

Under the Gen IV advanced reactor development program, the Very High Temperature Reactor (VHTR) is the lead concept. Design and development steps are currently underway to construct a high-temperature reactor as the next generation nuclear plant (NGNP) at Idaho National Laboratory (INL). A major limitation of this system is the development and qualification of high-temperature materials for structural applications. Such materials must possess good high-temperature resistance. Among candidate materials, Alloy 617 and Alloy 230 are considered the most promising structural materials for the VHTR. In order to gain a better understanding of material performance during a high-temperature and long-term service life, various material tests and experiments were conducted to investigate the fundamental deformation mechanisms of the alloys and their long-term degradation process during thermal aging.

First, mechanical properties of both alloys were studied by performing tensile tests at three different strain rates and at temperatures up to 1000ºC. This range covers time-dependent (plasticity) to time-independent (creep) deformations. At temperatures from 300 to 700ºC, the yield strength was found to be temperature independent as a result of additional strain hardening provided by *dynamic strain aging*. However, higher temperatures (>800ºC) activated additional deformation mechanisms, including dislocation creep and dynamic recrystallization, leading to a significant decrease in material strength. Consequently, the fracture mechanisms changed from inclusion particle cracks at temperatures up to 700ºC to triple junction cracks from 800 to 1000ºC. Through a strain-rate sensitivity analysis, the results of tensile tests were extended to approximate the alloys' long-term flow stresses. According to the comparison with these estimated flow stresses, the allowable design stresses for either alloy in American Society of Mechanical Engineers (ASME) B&PV Code did not provide adequate degradation estimation for the long-term service life. However, rupture stresses for Alloy 617, developed in ASME code case N-47-28, can generally satisfy the safety margin estimated in the study following the strain-rate sensitivity analysis.

Nevertheless, additional studies on material development are necessary in order for current VHTR conceptual designs to eventually meet design parameters defined by rupture stresses. Additionally, the effect of orientation on Alloy 617 was studied to provide proper guidance for engineering design and alloy development. Mechanical fibering, consisting of an alignment of inclusion particles and matrix crystals, was found to contribute to the mechanical anisotropy of Alloy 617 with varying performances across the studied temperature range.

Second, long-term thermal aging experiments (up to 3,000 hours) were performed to investigate the dynamic process of microstructure evolution and, consequently, mechanical property degradation at 900 and 1000°C for both Alloy 617 and Alloy 230. This microstructural evolution was found to be characterized by diffusion-controlled precipitation and coarsening of carbide particles (mainly $M_{23}C_6$ and M_6C). The kinetics of particle coarsening was studied though the measurement of volume increase of intergranular particles. The results of the mechanical tests were in good agreement with microstructure observations. Both hardness measurements and tensile tests showed a typical aging process characterized by short-term strengthening and long-term softening. Generally, both alloys aged at 900ºC attained higher yield and tensile strengths with a longer hardening time compared to samples aged at 1000ºC. Alloy 230 exhibited a longer age-hardening duration compared to Alloy 617, due to a lower diffusibility of Tungsten atoms (primary solute element in Alloy 230). Beyond the mechanical tests at room temperature, the long-term aging degradation for high-temperatures tensile properties was found to be comparable to the degradation for low-temperatures properties.

Lastly, an advanced measurement technique, high-energy synchrotron radiation, was applied to Alloy 230 to investigate the deformation process during *in-situ* loading. The small volume fractions of carbides (i.e. ~6% of M_6C in Alloy 230), which are difficult to detect using lab-based X-ray machines or neutron scattering facilities, were successfully examined using high-energy X-ray diffraction. The loading processes of the austenitic matrix and the carbide were separately studied by analyzing their different lattice strain evolutions, and thus,

the response of each phase to the applied tensile load was clarified. Elastic anisotropy for various polycrystal planes (hkl) was also measured through various reflections for the austenitic matrix. The measured lattice strain can be converted to flow stress by a factor of Young's modulus calculated by Kröner's self-consistent method. The lattice strain measured from the (311) reflection is extensively studied, since it responds almost linearly to the applied stress in both the elastic and plastic regimes. The lattice strain evolution for carbides is different than that for the matrix. During the transition from the elastic regime to the plastic regime, carbide particles experience a dramatic loading process, and the internal stress reaches a critical value. The internal stress for the particles then begins to slowly decrease while the linear stress increases for the matrix. This indicates a continued particle fracture process during plastic deformations of the matrix. Finally, a high-energy diffraction technique was developed that combines synchrotron X-ray radiation and pressurized creep tubes and allows macroscopic creep strain and lattice strain to be simultaneously measured by a single X-ray exposure. A typical creep curve with an evidently identified secondary and tertiary creep was obtained by analyzing the X-ray diffraction patterns. *In-situ* observations of the development of dislocation densities and lattice strain make it possible to track the onset of accelerated creep void nucleation, growth and coalescence.

ACKNOWLEDGEMENTS

I would like to express my deepest appreciation to my advisor and committee chair, Dr. James F. Stubbins, for his excellent advising, inspiring discussion and guidance in research during my thesis work. Without Dr. Stubbins' consistent support in both academic and general fields, this dissertation would not have been possible. I would also like to thank Dr. Brent J. Heuser for his guidance during my Ph.D. study, particularly in the early stages of my graduate work. I would also like to thank Dr. Rizwan Uddin and Dr. Pascal Bellon, for being my committee members and giving invaluable suggestions on my dissertation.

I am very grateful for my fellow doctoral students, Xiang Chen, Hsiao-ming Tung, Weiying Chen, Di Yun, Ling Zou, Nan Li, Jiawei Tan, Hyunsu Ju, Jianwei Hu and Xiao Pan, who all provided kind help, sincere comments and emotional support. I would also like to thank Dr. Gianfranco at the University of Pisa for conducting preliminary microstructure examinations for the studied materials.

A special thanks goes to Dr. Meimei Li and Dr. Jon Almer for their help and support during synchrotron experiments at Advanced Photon Source. I also would like to think Lee Flower and Henry White from Haynes International Inc. for providing Haynes® 230 samples. I particularly would like to thank Jon Hansen for helping me edit my thesis, and Carlos Altamirano, Alyssa Ruiz and Michael Collins for serving as laboratory assistants.

Lastly, I would like to express my appreciation to my family: my parents and my wife. Without their love and encouragement, this dissertation would not have happened.

The work was supported by the US Department of Energy under grants DE-FC07-07ID14819 and DOE NEUP 09-516. The microstructural analysis was carried out in part in the Frederick Seitz Materials Research Laboratory Central Facilities, University of Illinois, which are partially supported by the U.S. Department of Energy under grantsDE-FG02-07ER46453 and DE-FG02-07ER46471. Use of the Advanced Photon Source was supported by the U. S. Department of Energy, Office of Science, Office of Basic Energy Sciences, under Contract No. DE-AC02-06CH11357.

To my wife, Qing

TABLE OF CONTENTS

LIST OF FIGURES

LIST OF TABLES

CHAPTER 1

INTRODUCTION

Hydrogen is considered to be a clean energy carrier that can replace fossil fuels in industries worldwide [1]. This potential use of hydrogen promotes the Very High Temperature Reactor (VHTR) as one of the most promising Gen-IV nuclear systems, with its dual capacities of thermochemical hydrogen production and high efficiency electricity generation [2]. By taking advantage of a high outlet temperature, hydrogen can be generated either by steam reformation from natural gas or through the iodine-sulfur (I-S) process. Additionally, the net plant efficiency of the VHTR has improved to over 50% at 1000ºC, compared with 33% for current light water reactors (LWRs) [3]. Fig. 1.1 shows a schematic of the original VHTR design proposed in the Generation IV international forum [3].

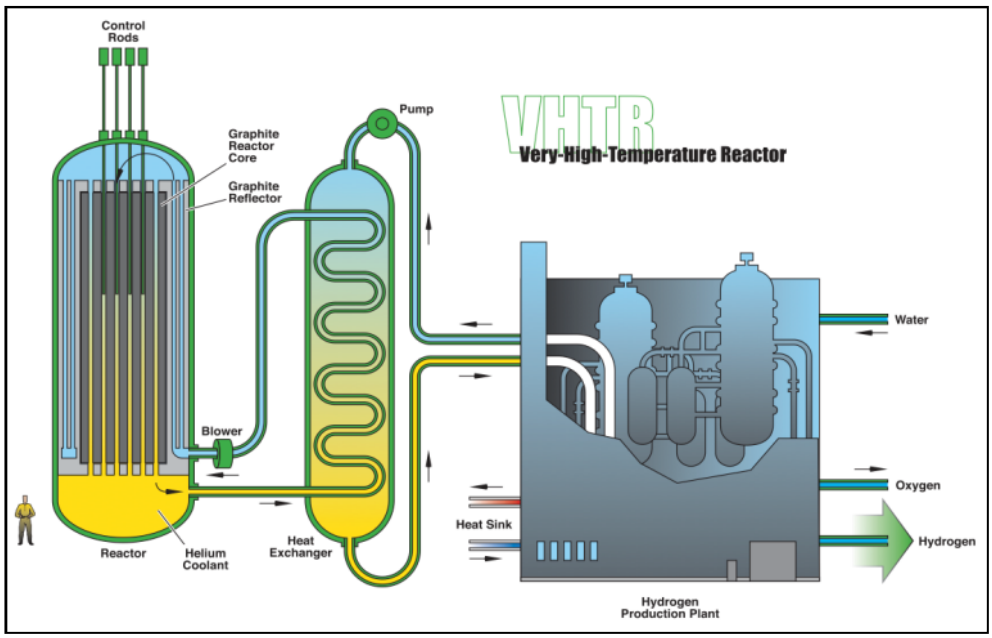

Fig. 1.1. Schematic of the VHTR [3]

In order to take advantage of the enormous benefits of the VHTR, effective structural components must be designed and utilized. However, the operating conditions in the reactor

system pose a great challenge for these components, particularly the intermediate heat exchanger (IHX), which requires the structural materials to withstand a high-pressure (~7MPa) and an aggressive atmosphere (corrosion and carburization/decarburization) for over 60 years [4]. Thus, various high-temperature material and design problems must be addressed for the implementation of the VHTR as an energy source. Firstly, the helium gas used as a coolant in the reactor system is expected to become contaminated by minor impurity gases (primarily H_2O, H_2, CH_4, CO, O_2, N_2 and CO_2) induced from external leakage (containing H_2O, H_2 and O_2) and reactions with the hot graphite core (generating H_2O, H_2, CH_4, CO and O_2) [5]. Despite a low content level (~10s ppm), these impure gases will further react with metallic structural materials, due to the high system temperature, and cause oxidation and carburization/decarburization in the materials. This interaction can significantly shorten the service life of the components. Also, similar to other high-temperature environments (e.g. aircraft gas turbines), creep, fatigue and creep-fatigue damages are unavoidable in the VHTR. These damages can be induced from: (1) internal high-pressure operations in the reactor system during long-term service, (2) thermal stresses caused by a large temperature gradient between the inlet and outlet of the heat exchanger and (3) relatively large deformations during various thermal transients [6]. These material issues are the main concerns for the design of reactor components. Lastly, the current ASME design limits do not consider the long-term aging effect on potential structural materials. Current engineering designs based on intrinsic material properties may underestimate the material degradation process during long-term, high-temperature operation.

Alloy 617 and Alloy 230 are solid-solution strengthened nickel alloys that are considered two of the most promising structural materials for building the intermediate heat exchanger of the VHTR. Both alloys display good strength at high-temperatures with exceptional corrosion resistance to a variety of reducing and oxidizing environments. Alloy 617 was first introduced in the early 1970's by Special Metals [7] to achieve better high-temperature performance than previously developed Ni-Co-Cr alloys (e.g. Haynes 25 and Alloy 188). Alloy 617 has a lower Co content without alloying W. Because of desirable high-

temperature resistance, Alloy 617 was extensively studied by high-temperature gas-cooled reactor (HTGR) programs during the late 1970's and early 1980's [8-10]. Despite the termination of HTGR programs in the U.S. during the 1980's, Alloy 617 continued to be studied in many scientific communities [11]. As a primary concern for alloy performance at high temperatures, the corrosion resistance of Alloy 617 was investigated in air and simulated reactor environments [12-23]. Creep damage, another significant threat for the alloy in the VHTR, has also been extensively studied [11, 24-34].

Alloy 230 is solid-solution strengthened Ni-Cr-W alloy introduced in the early 1980's as a competitor of Alloy 617 [35]. Compared to Alloy 617, Alloy 230 has better creep and corrosion resistance at elevated temperatures and lower cobalt content. Thus, Alloy 230 has also been considered as a candidate structural material for Gen-IV reactor components. However, the essential disadvantage of applying this alloy lies in the deficiency of available data of high-temperature material properties compared to the competing candidate material, Alloy 617. Most of the known mechanical properties of Alloy 230, including tensile, fatigue and creep data, can be found in technical literature from the website of Haynes International, Inc. [36]

Nevertheless, neither Alloy 617 nor Alloy 230 was specifically developed for nuclear systems. So despite the fact that both alloys have existed for over 20 years, the fundamental studies concerning changes in material properties in long-term, high-temperature environments are still limited. During high-temperature operation in a reactor system, metallic structural materials inevitably undergo a process of microstructural evolutions and consequent changes in mechanical properties. Other damaging material mechanisms during high-temperature service, including corrosion, creep, fatigue and creep-fatigue, are also associated with aging degradation [8]. Therefore, aging experiments are necessary to investigate the dynamic process of microstructure evolution and make predictions about material degradation during a reactor's long-term operation.

Studies on the aging effect on Alloy 617 have been conducted since it was introduced. Mankins et al. studied the microstructure and mechanical properties after long-term aging and

pointed out that $M_{23}C_6$ was the major second phase during aging [37]. Precipitation behavior was further studied by Kirchhofer et al. [38] Kihara et al. studied the changes of microstructure and proposed the mechanism of precipitate ripening under external loading (creep) [39]. Wu et al. studied the microstructure of Alloy 617 during long-term aging at relatively low temperatures (< 900ºC) [40]. The aging effect on Alloy 617 at 800 and 1000ºC for up to 1000 hours was also studied by Wright [23]. On the other hand, few studies on aging effects in Alloy 230 are currently available. Ren and Swindeman reviewed the existing data and literature for aging effects in both alloys [8].

Beyond traditional mechanical and microstructural methods of material studies, state-of-the-art technologies (e.g. synchrotron radiation) can benefit research and development of the Next Generation Nuclear Plant (NGNP) program by providing insight to time-resolved material properties. High-energy X-ray diffraction is an advanced and unique technique that has recently been developed for some of the largest third-generation synchrotron light sources, i.e. European Synchrotron Radiation Facility (ESRF, FR), Advanced Photon Source (APS, USA) and SPring-8 (JP). Using X-ray sources with higher energy and intensity than traditional sources, a much larger penetration volume, sufficient enough to represent the bulk material properties, is obtained to study internal/residual stress evolution, texture development and changes in dislocation structures [41-45]. Hence, synchrotron radiation provides a great opportunity for non-destructive probing of prospective structural materials for the VHTR (e.g. Alloy 617 and Alloy 230) and study of their dynamic strain/stress development for various phases during *in-situ* loading. Both time-independent tensile properties and time-dependent creep deformation can be investigated using high-energy synchrotron X-ray diffraction.

The objective of this project is to study the major performance of the structural materials for the design and construction of the VHTR. The study addresses partial material properties for high-temperature applications so that material performance can be properly considered in the context of the design of components with complex stress states, long intended service lives and high-temperature operating environments. Another important goal

of the study is to apply the aforementioned advanced measurement technique, high-energy synchrotron X-ray diffraction, to analyze the fundamental deformation process for various phases during *in-situ* loading. In addition, this work is intended to combine two techniques, pressurized creep tube and high-energy X-ray diffraction, to develop a new measurement approach that allows macroscopic creep strain and microstructure development to be accessed simultaneously by a single x-ray exposure. The entire dissertation work has been completed and is reported in the following three steps:

1. Investigation of intrinsic material properties of Alloy 617 and Alloy 230:

   The mechanical properties of both alloys were studied by tensile testing at various strain rates and at temperatures up to 1000ºC. This range covers deformations from time-dependent (plasticity) to time-independent (creep). Through strain-rate sensitivity analysis, the results of mechanical tests can be extended to evaluate the long-term flow properties of the alloys. These properties can also be assessed through comparison with ASME allowable design limits. Microstructure studies, including TEM, SEM and EBSD, were performed not only to gain basic microstructural information (e.g. grain structure, phases compositions, etc.) for the as-received materials, but also to provide an insight of deformation processes at various temperature (e.g. texture development, dynamic recrystallizations, particle ruptures, etc.) for deformed specimens after tensile testing. Additionally, the effect of orientation on tensile properties of Alloy 617 was studied to attain conservative engineering design limits. Though step (1), a fundamental understanding of material properties of Alloy 617 and Alloy 230 was established and served as a foundation for the following steps.

2. Study of the long-term aging effect on Alloy 617 and Alloy 230:

   The long-term (up to 3,000 hours), high-temperature (900 and 1000°C) aging experiments were conducted to study the aging degradation process of the studied materials during plant operations. Mechanical tests (including tensile and hardness measurements) were performed to study material strength development during

high-temperature aging. Associated microstructure examinations (including TEM, SEM and EBSD) were carried out to clarify the microstructural development in different aging periods for both alloys. The focus of the microstructure analysis was placed on studying the dominant feature during the long-term aging: diffusion-controlled precipitation and coarsening of carbide particles (mainly $M_{23}C_6$ and M_6C types) that can be reflected by the strength development of the material. Though step (2), a fundamental understanding of microstructural stability and associated mechanical property changes during long-term thermal aging was developed.

3. Applications of high-energy synchrotron radiation to study tensile and creep deformations: The deformation process of Alloy 230 was explored using *in-situ*, high-energy synchrotron radiation. The high resolution of the synchrotron X-ray diffraction provides a unique measurement for small volume fractions of carbides in the studied material (i.e. ~6% of M_6C in Alloy 230), which are difficult to observe using lab-based X-ray machines or neutron scattering facilities. Thus, the roles and limitations of particles under external applied stresses were clarified through lattice strain/internal stress analysis. Meanwhile, elastic anisotropy for the polycrystalline austenitic matrix was studied by measuring responses from various *hkl* reflections. The next study was developing a high-energy diffraction technique using a combination of the synchrotron X-ray technique and pressurized creep tubes. This combined technique allows for macroscopic creep strain and microstructural development to be measured simultaneously by a single X-ray exposure. *In-situ* observations of diffraction peak broadening and lattice strain development make it possible to track the onset of accelerated creep void nucleation, growth and coalescence. This work for the first time serves as an *in-situ* non-destructive technique for studying small specimens with similar geometry and scale as the prospective VHTR components for actual applications.

CHAPTER 2

LITERATURE REVIEW

The VHTR has been considered one of the most promising next generation reactors because of its dual capacities of high efficiency electricity generation and thermochemical hydrogen production. However, since this high-temperature reactor is expected to operate at temperatures up to 1000ºC, existing technical issues, especially regarding the uncertainty of structural material capacity at high temperatures, impede the development of the pilot plant at Idaho National Laboratory (INL), which was expected to operate by the 2020's [2]. This issue has promoted various research and development programs to investigate fundamental material properties of candidate structural materials (e.g. Alloy 617 and Alloy 230). The recent development of synchrotron radiation techniques provides a unique, non-destructive capacity to probe the materials and study their fundamental properties. Accordingly, the literature review presented in this chapter will cover three key topics: (1) Gen-IV nuclear reactors, with a particular focus placed on the VHTR, (2) material characterizations for candidate structural materials of the VHTR and (3) applications of synchrotron radiation techniques, particularly high-energy X-ray diffraction, on material development.

2.1 GENERATION IV NUCLEAR SYSTEMS

Global energy demands are predicted to double by the year 2030. In an effort to limit the emission of greenhouse gases and reduce global warming, the development of green energy sources to replace traditional fossil fuels presents a significant and urgent worldwide objective. Nuclear power remains a prominent energy source for the future due to factors of reliability, safety and economic performance. Since the early 2000's, a new term, nuclear renaissance, has been extensively used to describe the nuclear industry revival as a result of renewed global interest. This increase in interest is driven by the essential advantage of

nuclear energy: satisfactory energy production with limited greenhouse gas emissions. Nevertheless, safety concerns remain for next generation nuclear systems that aim to provide secure, affordable and clean energy. The current state of the nuclear industry has triggered various research and development studies for Generation IV nuclear systems.

2.1.1 GENERAL GEN-IV REACTOR CONCEPTS

In the early 2000's, six nuclear reactor concepts were identified and selected for further development by the Generation IV International Forum (GIF), a consortium of 13 nations charged with planning the nuclear plants of tomorrow [46]. The six nuclear systems chosen as Generation IV reactor concepts employ a variety of reactor, energy conversion and fuel cycle technologies. The Gen-IV reactors display a wide diversity in reactor size and feature a combination of thermal and fast neutron spectra, closed and open fuel cycles and operating temperatures ranging from 500 to 1000ºC. In general, these new plants are expected to operate at higher temperatures than current generation reactors to improve efficiency and provide additional energy supply (e.g. hydrogen). Additionally, simplified safety features would be introduced in support of sophisticated backup systems and experienced operators.

Each type of the Gen-IV reactors possesses unique technical features and special benefits that set it apart from other reactor types. For example, the supercritical-water-cooled reactor (SWCR) is the only type of Gen-IV reactor that uses water as the coolant. The SWCR is set apart from traditional LWR currently in place, however, by the coolant temperature (~510-625ºC) and operating pressure (~25 MPa), both of which are much higher than normal operation conditions of LWR's. The SWCR is expected to operate at conditions above the supercritical condition (374ºC, 22.1 MPa) and, thus, achieve a high plant efficiency near 45%. Furthermore, compared to other Gen-IV reactors, the SWCR has a much larger technology base that obtained from existing LWR's and commercial supercritical-water-cooled fossil-fired power plants. According to each reactor type's technical maturity, the Generation IV systems are expected to become available for commercial introduction in the period between 2015 and 2030 or beyond. The overview of six Gen IV reactor concepts is shown in Table

2.1. More details on each type of nuclear system and its required research and development can be found in a report issued in 2002 under the title "A Technology Roadmap for Generation IV Nuclear Energy Systems" [3].

Table 2.1. Overview of Generation IV reactor concepts [3]

System	Size (MWe)	Operating temperature (ºC)	Pressure (MPa)	Energy output	System partner countries
VHTR	250	1000	7	Electricity and hydrogen	CA, EU, FR, JP, KR, CN, CH, US, ZA
GFR	200-1200	850	7	Electricity and hydrogen	EU, FR, JP, CH
SFR	300-1500	550	0.1	Electricity	EU, FR, JP, KR, US, CN
SCWR	1500	510-550	25	Electricity	CA, EU, JP
LFR	50-150 300-600 1200	550-800	0.1	Electricity and hydrogen	EU, JP
MSR	1000	700-800	0.1	Electricity and hydrogen	EU, FR

2.1.2 VERY HIGH TEMPERATURE REACTOR

Among all of the Gen-IV nuclear systems, the VHTR has been considered one of the most promising rector systems. This fact can be seen in Table 2.1 showing that all the active member countries of GIF are participants in the research and development of the VHTR. The unique and attractive feature of the VHTR is its dual capacities of high efficiency electricity generation and thermochemical hydrogen production [2]. By taking advantage of a high outlet temperature, hydrogen can either be generated by the reformation of steam from natural gas or from the iodine-sulfur (I-S) process [3]. In addition, the net plant efficiency of the VHTR can exceed 50% at 1000ºC, a major improvement from ~33% efficiency of current LWR's. However, the high-temperature operating environment poses great challenges for the selection, examination, and qualification of possible structural materials for reactor components, including gas ducts, pressure vessels, and intermediate heat exchangers (IHX) [3, 47]. In particular, the IHX is responsible for heat transfer from the primary helium loop to the

secondary loops used for electricity generation and hydrogen production, and the component is expected to experience high pressure (~7MPa) and an aggressive atmosphere (corrosion and carburization/decarburization) during plant operation [4]. Various material issues that occur at high temperatures would be unavoidable during the plant's long-term service life. These issues include a decrease of material strength and metallurgical stability during aging, environment-metal interaction, time-dependent deformation (creep), etc. From an engineering perspective, a large temperature gradient is a main potential threat to structural materials during high-temperature operation. First, the shape of the plates of the IHX will transform from rectangular to trapezoidal due to the temperature gradient from the inlet and outlet of the IHX [48]. This gradient induces thermal stresses in the IHX and results in material creep damage. Second, a thermal transient may induce fatigue behavior, which could dramatically reduce the service life of the material [6]. Furthermore, the compact type heat exchanger (e.g. printed circuit heat exchanger (PCHE)) was selected to replace the traditional shell-and-tube and helical coil types in pre-conceptual designs of high-temperature reactors in order to enlarge the heat transfer area and obtain a high efficiency [48]. (Table 2.2) The geometry of the IHX results in a design challenge to control the thermal gradient in the transverse direction of gas flow. An orientation effect from the material is therefore difficult to neglect in the design stage.

Because of the rigorous material requirements for building the VHTR, the principle design parameters, including the operating temperature and power output, were recently modified in new pre-conceptual designs. Table 2.2 shows several important design parameters for the VHTR, Fort St. Vrain HTGR and three pre-conceptual designs of high-temperature reactors (HTR's). It should be noted that all of the pre-conceptual designs select PCHE as the primary type of heat exchanger. Additionally, predicted outlet temperatures have been reduced from approximately 1000ºC to 950/900ºC in general. Despite this change, the stated challenges for structural materials of the intermediate heat exchanger still exist. Therefore, careful material tests, evaluations and screenings are necessary.

Table 2.2. Partial design parameters for the VHTR, Fort St. Vrain HTGR and pre-conceptual high-temperature reactors (HTR's) [3, 48]

Conditions or Features	Prospective VHTR	Fort St. Vrain HTGR	GT-MHR (General Atomics)	ANTARES (AREVA)	PBMR (Westinghouse)
Reactor Power Outlet (MWth)	600	842	550-600	565	500
Average power density ($MWth/m^3$)	6-10	6.3	6.5		4.8
Moderator	Graphite	Graphite	Graphite	Graphite	Graphite
Reactor type	Dependent	Prismatic	Prismatic	Prismatic	Pebble Bed
Plant design Life (years)	60	30	60	60	60
Coolant inlet Temperature (ºC)	640	406	590	500	400
Coolant outlet Temperature (ºC)	1000ºC	785	Up to 950	900	950
Coolant Pressure (MPa)	Dependent on process	4.8	7	5	9
Coolant flow rate(kg/s)	320 kg/s	428	320	240	193
IHX Design	Compact types	NA	PCHE	PCHE or Fin-Plate	PCHE
Secondary Fluid	He	Steam	He	He	He-N

2.2 STRUCTURAL MATERIALS FOR THE VHTR

The prospective structural materials for the heat exchangers are Inconel 617, Haynes 230, Incoloy 800H and Hastelloy XR [48]. Incoloy 800H (Alloy 800H) is the only iron based material among the candidate alloys. The approved temperature for Alloy 800H for nuclear applications is 760°C. Despite a lower allowable temperature compared to nickel based alloys, Alloy 800H is still considered as a structural material for components with a lower operation temperature (e.g. the secondary heat exchanger in the two stage design of IHX) [6, 48]. Hastelloy XR is a modified version of Hastelloy X, which has been used in IHX design for the Japanese High-Temperature Engineering Test Reactor (HTTR). Better corrosion resistance results in an impure helium environment have been reported for the Hastelloy XR compared to Inconel 617 (Alloy 617). However, inferior strength of Hastelloy XR at temperatures over 900ºC limits possible application in the VHTR [49]. Both Inconel 617 and Haynes 230 (Alloy 230) are solid-solution nickel-based alloys. With superior strength at

elevated temperatures, each alloy has been recognized as a primary candidate structural material for VHTR applications. The typical chemical composition for each alloy is shown in Table 2.3.

Table 2.3. Limiting chemical compositions in weight percentage for Alloy 617 and Alloy 230 [7, 36]

	Alloy 617	**Alloy 230**
Ni	44.5 min	Bal.
Cr	20.0-24.0	20.0-24.0
Co	10.0-15.0	5.0 max
Mo	8.0-10.0	1.0-3.0
Al	0.8-1.5	0.2-0.5
C	0.05-0.15	0.05-0.15
Fe	3.0 max	3.0 max
Mn	1.0 max	0.3-1.0
Si	1.0 max	0.25-0.75
S	0.015 max	0.015 max
Ti	0.6 max	0.1 max
Cu	0.5 max	0.5 max
B	0.006 max	0.015 max
P	-	0.03 max
La	-	0.05 max
W	-	13.0-15.0

2.2.1. ALLOY 617 & ALLOY 230

Alloy 617 is an austenitic Ni-Co-Cr alloy that was introduced in the early 1970's as a tungsten-free, nickel-based alloy with lower weight and cost compared to tungsten-containing alloys [11]. With a high content of Mo, Cr and Co, Alloy 617 shows exceptional creep strength and corrosion resistance at high temperatures. It has been regarded as one of the most promising candidate materials for high-temperature reactors since the early 1980's [49]. Since then, numerous studies central to all aspects of material properties have been conducted to examine whether Alloy 617 can meet the strenuous requirements of high-temperature reactor systems. Corrosion damage in a simulated HTR/VHTR atmosphere has been studied by Bates et al. [12], Graham [13], Christ et al. [14, 15], Jang et al. [16] and recently by Cabet et al. [17-21] Research on short-term and long-term corrosion in high-temperature air was reported by Jang et al. [16], Harper et al. [22], and Wright [23]. Creep damage assessment of Alloy 617 at high temperatures has been performed both in air [11, 24-29] and in a simulated reactor environment [30-32]. The changes of grain boundary characteristics and related intergranular

precipitates during creep were studied by Lillo et al. [33] and Schlegel et al. [34] using EBSD. Other mechanical properties, such as tensile, fatigue, creep-fatigue interactions and fatigue crack initiation and growth, have been analyzed in different environments as well [31, 50-54].

Alloy 230 is a relatively new solid-solution strengthened Ni-Cr-W alloy introduced in the early 1980's [35]. Compared to Alloy 617, Alloy 230 has better creep and corrosion resistance at elevated temperatures as well as a lower cobalt content. Even though the relatively high content of boron may cause material degradation under irradiation, Alloy 230 is still considered to be a potential structural material for the IHX of the VHTR [8]. Compared to Alloy 617, available experimental data for Alloy 230 is relatively limited. Oxidation studies in high-temperature air were performed by Whittenbergeer [55] at lower temperatures (<900ºC) and by Chien and Brown [56], Tawancy [57] and Liu et al. [58] at higher temperatures (>900ºC). In addition to Alloy 617, Cabet and Rouillard et al. also analyzed the corrosion degradation behavior of Alloy 230 [17-20, 59-61]. Kim et al. studied and compared the oxidation characteristics of Alloy 617 and Alloy 230 in air and in a simulated helium environment at 900 and 1000ºC [62]. Fatigue, creep and related crack growth behaviors of Alloy 230 were investigated by Lu et al. [63-66] Additionally, creep data can be found in technical literature from the website of Haynes International, Inc. [36]

The allowable design stresses for Alloy 617 and Alloy 230 can be found in section II, Part D and section VIII, Div. 1 of American Society of Mechanical Engineers (ASME) Boiler and Pressure Vessel (B&PV) Code, respectively. Fig. 2.1 shows the allowable design stresses for both alloys at temperatures ranging from 1000 to 1800ºF (538 to 982ºC). Compared to Alloy 617, Alloy 230 shows relatively high design stresses up to the temperature of 1200ºF (649ºC). However, the difference diminishes as temperature increases. It must be noted that neither alloy is well qualified under Section III, Division NH, which provides criterion for the design, fabrication, inspection, testing and certification of nuclear facility components [8]. Additional effort is required to achieve material qualification and code development for Alloy 617 and Alloy 230.

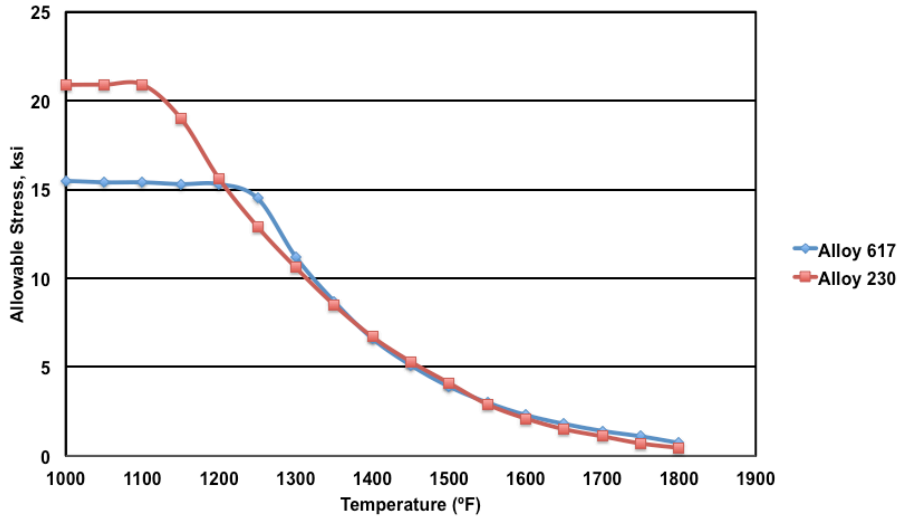

Fig. 2.1. Allowable design stresses of Alloy 617 and Alloy 230 (reproduced using data obtained from [67])

2.2.2 AGING EFFECT ON ALLOY 617 AND ALLOY 230

Many material damage mechanisms during high-temperature service, including creep, fatigue and creep-fatigue, are associated with aging degradation and process of microstructural evolution, including grain growth, phase transformation, precipitate ripening, etc. [8] Hence, aging experiments are necessary to develop a fundamental understanding of the dynamic process of microstructural evolution and to predict material degradation during a reactor's long-term operation. Studies pertaining to the aging effect of Alloy 617 have been carried out since it was introduced in the early 1970's. Mankins et al. studied the microstructure and mechanical properties of Alloy 617 after long-term aging and pointed out that $M_{23}C_6$ was the major precipitate during aging [37]. This precipitation behavior was confirmed by Kirchhofer et al. [38] Kihara et al. studied changes in microstructure and proposed the mechanism of precipitate ripening under load (creep) [39]. Wu et al. studied the microstructure of Alloy 617 during long-term aging at relatively low temperatures (< 900ºC) and developed the time-temperature transformation (TTT) diagram according to existing data [40]. The aging effect in Alloy 617 at 800 and 1000ºC was also studied by Wright [23]. His results indicate that tensile properties, including yield strength, ultimate tensile strength and ductility, as well as grain size of Alloy 617 are not significantly influenced by thermal aging

up to 1000 hours. Ren and Swindeman reviewed existing data and literature for the aging effect in both alloys [8, 9]. Compared to a large number of aging experiments completed on Alloy 617, few aging studies on Alloy 230 are currently available, particularly for the long-term aging effect. Increased focus on the aging effect for Alloy 230 is required to achieve material qualification for NGNP applications [8].

2.3 APPLICATIONS OF SYNCHROTRON X-RAY RADIATION IN MATERIAL RESEARCH

Synchrotron radiation is generated from an electron storage ring by accelerating electrons up to several GeV and results in X-rays with high brilliance and continuous spectrum [68]. Synchrotron radiation has been used extensively as a non-destructive technique in material research due to its unique properties, including high intensity, extended spectral range and high degree of polarization [69]. These benefits enable synchrotron radiation to be extremely useful in imaging and real-time experiments requiring "hard" X-rays (defined by a wave length of $\lambda \leq 2.5$Å).

Synchrotron X-ray scattering, as the one of the most significant and frequent applications of synchrotron X-ray measurement, has been widely used to investigate complex crystal structures, including single crystals, powders and fibers [70, 71], time-resolved and *in situ* material evolutions [72-74], material properties at high pressures [75-78] as well as localized material properties by decreasing the beam size to the sub-micron region (micro-diffraction) [79-82]. Another important technique is X-ray diffuse scattering that can be used for defect observations in metals, polymer crystallizations, etc. [83-85] Additionally, small/ultra-small angle X-ray scattering (SAXS/USAXS), based on the synchrotron source, has recently become a significant technique for microstructure characterizations in metallurgy (particularly for studying reinforced particles) [86, 87], nano-science [88, 89], polymer-science [90, 91] and biomaterials [92-94]. Beyond various X-ray scattering techniques, X-ray tomography [95, 96], X-ray fluorescence (XRF) [97, 98] and X-ray absorption spectroscopy [99, 100] have also been extensively studied and applied to various material studies.

2.3.1 HIGH-ENERGY X-RAY SCATTERING

Generally, the photons in an energy range from 40 to 120 keV can be defined as high-energy X-rays. High-energy X-rays have intrinsic benefits due to a long penetrated distance in studied materials. The intensity after travelling a distance of x can be calculated based on the modified Beer-Lambert law:

$$I_x = I_o e^{(\mu/\rho)\rho x}$$

In this relation, I_x represents the measured beam intensity, I_o is the original beam intensity, μ is the attenuation coefficient (in cm^{-1}), μ/ρ is the mass absorption coefficient, ρ is the material density and ρx is the area density (mass thickness). The mass absorption coefficient depends significantly on the incoming X-ray energy. An example showing the relationship between the mass absorption coefficient and photon energy for iron is given in Fig. 2.2 [101]. The mass absorption coefficient for iron decreases by a factor of over 100 from 10keV for a typical photon energy generated by a metal anode in a lab-based X-ray machine to 100keV for a typical high-energy photon generated by a synchrotron source. The peak/discontinuity in the curve is the K- absorption edge (Photoelectric effect).

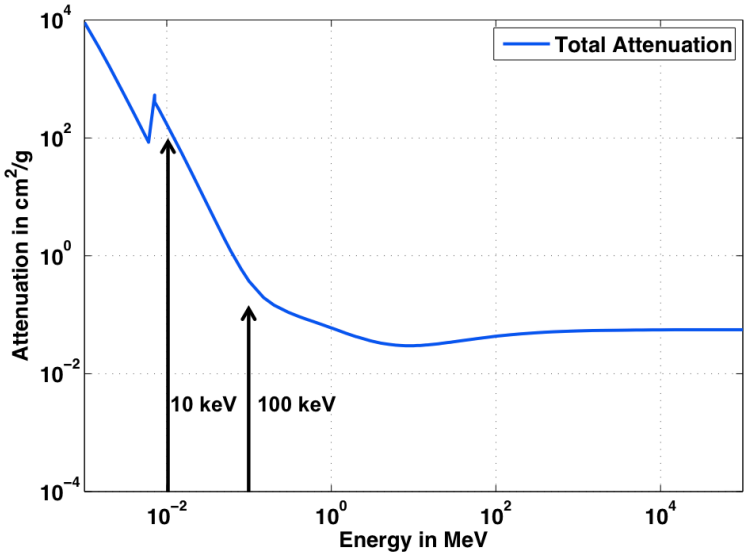

Fig. 2.2. Photon mass attenuation coefficient for iron (reproduced using data obtained from [101])

In the case of a lab-based X-ray tube that features characteristic X-rays for experimentation, the photon energy, E (keV) can be calculated by:

$E = 12.4/\lambda$

This formula is deduced from the relation: $E = hv = hc/\lambda$. Here, h is Planck's action constant, v is the frequency of the photon and λ (Å) is the wavelength of the photon. Assuming molybdenum is used as the anode and its characteristic $K\alpha_1$ radiation is selected for experimentation, an X-ray with energy of 17.48 keV could be generated. Table 2.4 shows a comparison of the penetration distance of two X-rays with different energy levels.

Table 2.4. X-ray penetration distances in copper and wrought iron [102]

Material	17.48 keV ($K\alpha_1$ radiation of Mo tube)	80 keV (high-energy Synchrotron X-ray)
Copper	0.10 mm	6.9 mm
Wrought Iron (0.01 % C)	0.16 mm	10.7 mm

It is apparent that the high-energy X-ray travels a much longer distance in metallic materials than the low-energy X-ray. With low penetration depth, lab-based X-rays can only measure the near-surface area, whereas the synchrotron radiation technique allows the high-energy X-ray to penetrate a much longer distance and obtain a larger material diffraction volume. Results of high energy XRD measurements are often comparable to those of neutron diffraction. Whereas neutron diffraction does feature large penetration depths, the process requires an extensive collection time of scattered neutrons [69, 103].

Recent applications of high-energy synchrotron X-ray have not only focused on traditional metals and alloys, but have also been broadened to examine coating materials, composites and biomaterials. Almer et al. applied the high-energy X-ray technique on various coating materials, analyzing the strain and texture of physical-vapor deposited metal nitride coatings [45] as well as the microstructure, stress and thermal stability of arc-evaporated Cr-C-N coatings [104-106]. Similar analysis on high strength, Cu/Nb multilayers has also been conducted by Aydiner et al. to investigate the material deformation mechanisms under tensile loading [107, 108]. The load partitioning that occurs between the matrix and the reinforced phase in metal matrix composites (MMC's) has been extensively studied using high-energy synchrotron X-ray diffraction [41, 42, 109, 110]. Additionally, Almer and Stock have

employed high-energy synchrotron X-ray radiation to study the internal stress development of cortical bone during *in situ* compression [111].

Recently, some fundamental questions central to the deformation mechanism of metals were investigated using high-energy synchrotron radiation. The evolution of dislocation cell structures that previously could only be seen using electron microscopy, was successfully observed by analyzing the diffraction pattern of a single grain of 99.99% pure copper during *in-situ* loading [44]. This work clears the way to study the self-organization process of dislocation structures during plastic deformation using X-ray diffraction. Another study conducted by Cheng et al. involved analyzing the crystalline scale effect on deformation mechanisms. The deformation process for nickel grains ranging from 10 to 1000 nm was studied using high-energy synchrotron X-ray and neutron scattering [43]. This work provided a methodology with which to study the question that has been debated for years: how a material deforms at small length scales (e.g. in nanocrystalline).

High-energy, wide angle X-ray scattering can be coupled with small angle scattering to provide microstructural information at a larger length scale. For example, the Q-value obtained by USAXS at sector 32 at the Advanced Photon Source can cover the range from 0.0001 to 0.1 $Å^{-1}$, corresponding to a feature size ranging from 2 to 600 nm [112]. Therefore, the void evolution as a result of continuous crack and de-cohesion of particles during a material's plastic deformations can be reflected by the changes in intensity of small angle scattering. A study combining wide and small angle X-ray scattering has been conducted by Pan et al. to observe *in-situ* void development as well as strain/stress evolution of the modeled ferritic/martensitic materials [86, 87]

2.3.2 RESIDUAL STRESS MEASUREMENT

Any mechanical or thermal processing can potentially cause inhomogeneity in materials and lead to residual stresses [113]. There exist three fundamental physical origins of residual stress: plastic flow, volume change and thermal dilatation. One or any combination of these sources placed on a material without complete relaxation would result in residual

stresses [69]. Residual stresses are important because they can cause great damage to engineering materials. For instance, metals and alloys can suffer stress corrosion cracking (SCC) in a corroded environment with applied stresses, such as residual stress [114]. Therefore, metallic components with residual stresses resulting from welding often experience SCC during operation in a corrosive atmosphere. On the other hand, deliberately induced residual stresses can partially improve material performance (e.g. strength). Therefore, complete understanding of the origin and impact of residual stresses is significant for the implementation of metal alloys in Gen-IV reactor systems.

Residual stresses are commonly categorized into three types according to length scale [115]. Fig. 2.3 provides a graphical explanation for the types of stresses:

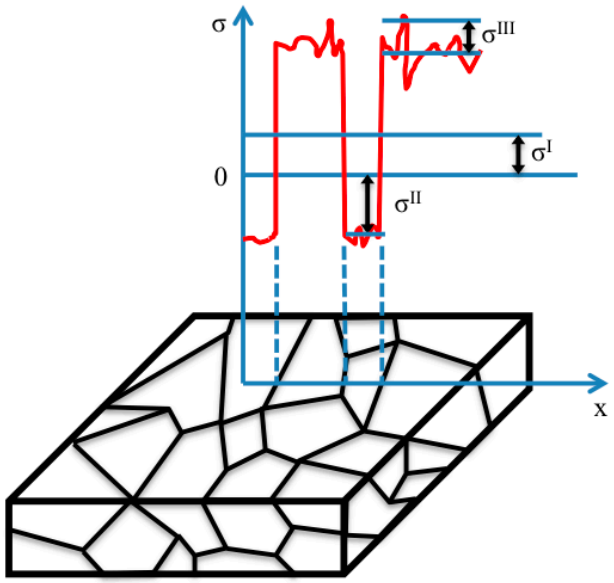

Fig. 2.3. Three orders of stresses (Type I, II and III)

Type I (σ^I): These residual stresses in the largest length scale cover a large number of crystal domains of the materials and show the overall effect from macroscopic plastic deformations or thermal treatments. Because the type I stresses are self-equilibrate over a macroscopic dimension that is composed of a large number of grains, type I stresses are also referred to *macrostresses*. These stresses can be interpreted by measuring the diffraction peak shift via X-ray diffraction experiments [69, 103, 113]. (Fig. 2.4)

Type II (σ^{II}): These residual stresses are homogenous within the region of small crystal domain, comparable to a grain structure whose length scale is often on the scale of tens to hundreds of a micron. These stresses universally exist in polycrystalline metals because of elastic misfits in grains with different orientations. Therefore, type II stresses are more significant in multi-phase materials because of their larger discrepancy among phases. Type II stresses are also known as *intergranular stresses*, although they are not directly associated with stress placed on grain boundaries [103].

Type III (σ^{III}): These residual stresses are homogeneous on the smallest length scale, which is near a few interatomic distances [69]. These stresses are often induced by small defects (e.g. dislocations or point defects) within a grain. Type II and III stresses are often collectively termed as *microstress* because of their much smaller length scale compared to the type I stresses. For high-energy synchrotron X-ray or neutron scattering measurements, penetration volumes are much larger than the characteristic volumes (proportional to the characteristic length scale) of the Type II and III stresses, so the *microstress* causes peak broadening rather than peak shift [103]. (Fig. 2.4)

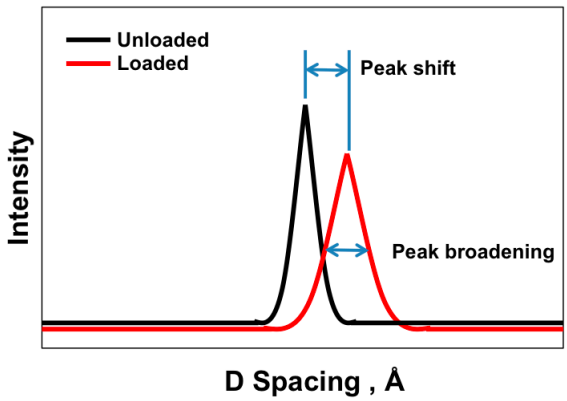

Fig. 2.4. A schematic showing peak shift and broadening caused by deformation

The focus of a material research project determines what stresses should be studied. A group that is studying composite materials may be interested in *microstress* in order to examine the interaction between phases and understand the process of reinforcement. In contrast, *macrostress* is generally more attractive for engineers and component designers.

Accurate *macrostress* measurement can aid in estimating component service life or reveal a method to increase material performance [103].

2.3.3 CREEP MEASUREMNT USING SYNCHROTRON RADIATION

Time-dependent deformation, or creep, is one of the most significant material issues limiting current design of advanced power systems (e.g. high-temperature reactor systems, advanced fossil energy systems or even fusion power systems) [4, 116]. The components in these systems are expected to operate reliably at elevated temperatures for long-term service life. This poses a great challenge for structural materials that require higher creep resistance for extended service lives. Meanwhile, a more advanced technique for material characterization is necessary for material development.

To date, most synchrotron studies on creep are focused on X-ray tomography to evaluate creep void evolutions. The capacity of synchrotron X-ray tomography allows micron-level creep voids to be measured during both *in-situ* and *ex-situ* loading [117-120]. Beckmann et al. investigated the preferred orientation of pores using synchrotron X-ray microtomography during *in-situ* creep loading [118]. The group observed a transient with an accelerated increase of microcracks during creep, which might be caused by the enhanced coalescence of pores. Cheong et al. conducted a similar study on austenitic Fe–Ni–Cr stainless steel to examine wedge-shaped voids in various creep stages [120].

In addition to showing creep void development, the local strain, ε, can be obtained via synchrotron microtomography by measuring the cross-section area of the sample before and after creep tests (A_0 and A^*):

$$\varepsilon = \ln(A_0 / A^*)$$

Thus, macroscopic creep strain and microscopic creep voids can be measured simultaneously using synchrotron microtomography [117, 119].

The limitations of applying synchrotron X-ray tomography to creep studies are apparent. First, only creep voids greater than a few microns in size can be readily measured. So the initial stage of creep, where pores can be very small, is difficult to characterize using

X-ray tomography. The situation can also become challenging for real-time measurement because the resolution of tomography is significantly dependent on the sample alignment, which can be disturbed during *in-situ* loading. Second, other than voids and cracks, X-ray tomography cannot provide any other microstructural information (e.g. dislocation development). During creep deformation, dislocations in metals experience a complex process involving rearrangement, glide, climb and changes in density. Pyzalla et al. recently conducted an experiment combining X-ray tomography and diffraction to investigate *in-situ* creep void growth and microstructure development simultaneously [121]. The dislocation density shown by the width of reflection peaks was found to decrease during the early stage of creep and stabilize in a short period of time. The results showed a definite process of dislocation development during creep: dislocation rearrangements as a result of high-temperature annealing followed by a thermally activated cross-slip and climb.

CHAPTER 3

MECHANICAL PROPERTIES AND MICROSTRUCTURE

In this chapter, the basic mechanical properties and microstructure of Alloy 617 and Alloy 230 are presented. The mechanical properties of both alloys were studied by performing tensile tests at three different strain rates and at temperatures up to 1000ºC. This range covers time-dependent (plasticity) to time-independent (creep) deformations. The microstructural examinations on both the as-received and fractured specimens (after tensile testing) clarified the deformation and fracture mechanisms of each alloy. Additionally, the effect of orientation on tensile properties of Alloy 617 was studied to attain its conservative engineering design limits. Finally, strain-rate sensitivity analysis for both alloys was conducted to approximate their long-term flow stresses. The results were extended to evaluate current ASME allowable design limits.

3.1 MICROSTUCTURE EXAMINATIONS

Alloy 617 and Alloy 230 were supplied by Haynes International as 1 inch and 1.5 inch thick plates, and each was hot worked and solution treated at 1177ºC for 37 min and 1191ºC for 3 hours, respectively. (Heat Number: 861758808 for Alloy 617 and 830587801 for Alloy 230.) The chemical composition is shown in Table 3.1.

Table 3.1. Chemical composition of Alloy 617 and Alloy 230 in average weight percent

Alloy	Al	B	C	Co	Cr	Cu	Fe	La
617	1.03	<0.002	0.08	12.2	22.1	0.017	1.104	-
230	0.38	0.004	0.11	0.29	21.7	0.04	1.4	0.014
	Mn	**Mo**	**Ni**	**P**	**S**	**Si**	**Ti**	**W**
617	0.064	9.46	52.86	0.002	<0.002	0.05	0.39	-
230	0.46	1.75	BAL	0.005	<0.002	0.4	<0.01	13.89

Microstructure analysis was performed using a JEOL 2100 Cryo TEM, JEOL 2010 LaB6 TEM and JEOL 7000F SEM coupled with EBSD capabilities. The TEM samples were prepared using electropolishing methods with a solution of 10% acetic acid in methanol at -

45°C and 22V. The SEM samples were etched for ~3 min using 10 ml acetic acid, 15 ml HCl and 10 ml HNO_3. The EBSD samples were polished with SiC abrasive paper down to 600 grit followed by 1μm and 0.3μm alumina solutions. Finally, the polishing process was completed with vibratory polishing with 0.02 μm colloidal silica.

The intrinsic particles in Alloy 617 are Cr rich $M_{23}C_6$, Mo rich M_6C and a small amount of Ti(C,N). [37] Similar to Alloy 617, Alloy 230 has intrinsic W rich M_6C. [35] Fig. 3.1(a) & (b) show the microstructure of Alloy 617 and Alloy 230, respectively. The inclusion particles in both alloys are induced from the hot rolling process and cannot be re-dissolved during solid solution annealing. Similar to the particles in a hot rolling steel, these carbides in Alloy 617 and Alloy 230 are strung as bands in the transverse planes and flattened in the rolling planes. Additionally, these carbide particles in Alloy 617 are not evenly distributed in the material, but instead spread as clusters in various areas. (Fig. 3.1(a)) Comparatively, the inclusion particles in Alloy 230 distribute more homogenously. (Fig. 3.1(b))

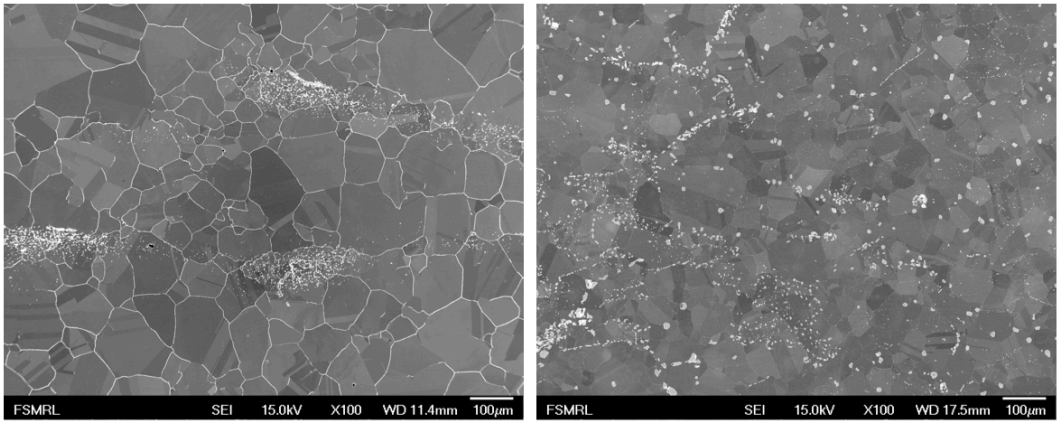

(a) (b)

Fig. 3.1. Microstructure of the materials in the as-received condition:
(a) Alloy 617 (b) Alloy 230

In addition to the large inclusion particles, many intergranular precipitates were observed in both alloys. (Fig. 3.2 and Fig. 3.3) In Alloy 617, these second phase particles are present as a thin film precipitating on grain boundaries and connected to large inclusion particles. (Fig. 3.2) In Alloy 230, this intergranular particle is dendritic, but it also connects to

large inclusion particles. (Fig. 3.3) Due to a small volume fraction, these intergranular particles have little impact on both alloys' mechanical properties.

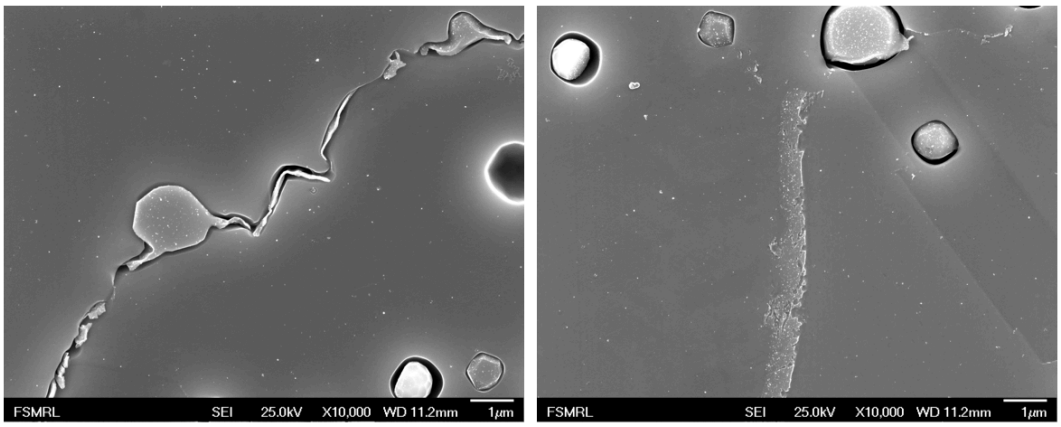

(a) (b)

Fig. 3.2. Intrinsic particles in Alloy 617 in the as-received condition: (a) Inclusion particles (b) Intergranular precipitates

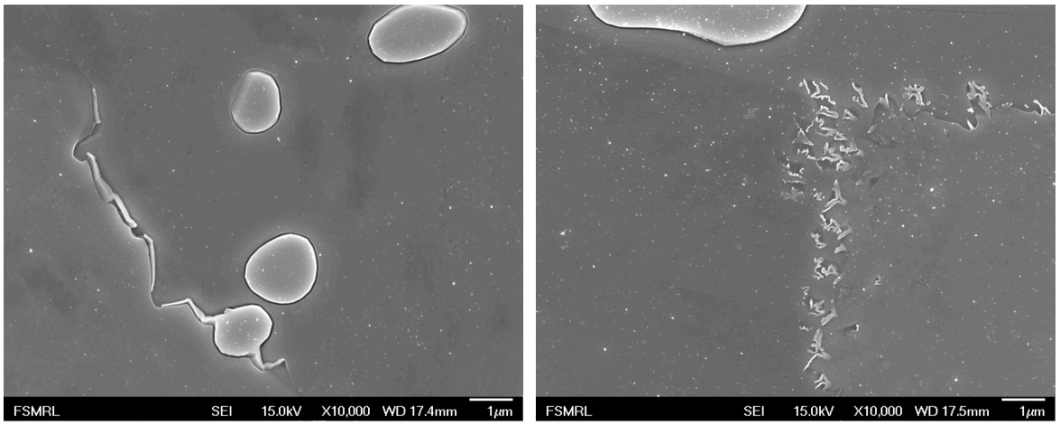

(a) (b)

Fig. 3.3. Intrinsic particles in Alloy 230 in the as-received condition: (a) Inclusion particles (b) Intergranular precipitates

The distribution of grain size in Alloy 617 is duplex: small grains with size ranging from 10 to 30 μm in the inclusion rich areas and large grains with size ranging from 40 to 100 μm in the inclusion free areas. During solid solution annealing, the inclusion particles exert a pinning pressure on grain boundaries and impede their movement/immigration (Zener pinning) so that the crystal growth is much slower in the inclusion rich areas. Hence, small grains are obtained in the inclusion rich areas after annealing, whereas coarse grains are found in the

inclusion free areas. (Fig. 3.1(a) and Fig. 3.4(a)) Nevertheless, particle distribution in Alloy 230 is more homogenous. This results in moderate grain size variation after solid solution annealing. The average grain size is ~70 μm in Alloy 230.

From EBSD analysis, ~60% and ~53% of the grain boundaries are twin boundaries (or coincidence site lattice (CSL) ∑3 grain boundary) for Alloy 617 and Alloy 230, respectively. The twin boundaries are shown as red lines in Fig. 3.4.

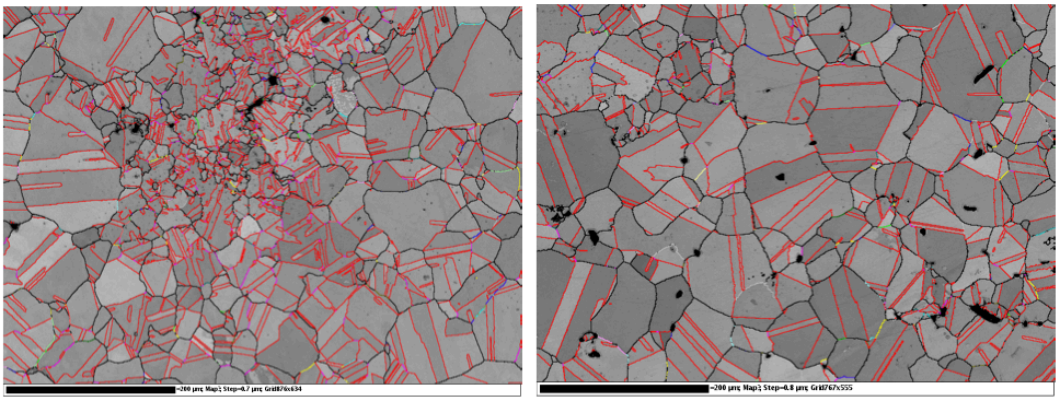

Fig. 3.4. EBSD and CSL boundary analysis of the materials in the as-received condition: (a) Alloy 617 (b) Alloy 230

3.2 MECHANICAL TESTS

The prospective design of IHX for the VHTR requires the thickness of the chosen material to be in the range from 0.2 to 2 mm. [5] Considering a compatible dimension, miniature specimens were used to study the alloys' tensile properties. (Fig. 3.5) The Alloy 617 specimens with the same geometry and dimensions have been employed to study the grain boundary engineering (GBE) and irradiation effects. [122] Another important reason for using miniature tensile specimens is that the material's strength in the plate thickness direction can be readily tested.

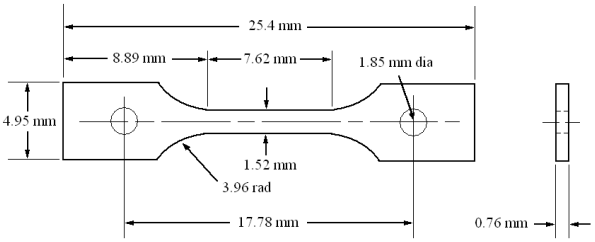

Fig. 3.5. Geometry and dimensions of tensile specimens.

Tensile specimens were cut along the long-transverse (LT) direction from the rolling plane. (Fig. 3.6) Tensile tests with a strain rate of ~10^{-3}/s were conducted at temperatures ranging from room temperature (RT) to 1000ºC using an INSTRON 1331 servo-hydraulic test system equipped with a high temperature furnace. Temperature was maintained for ~40 minutes after heating to the desired value to gain a stabilized and homogenous heat zone. The temperature variation was ±3ºC during testing.

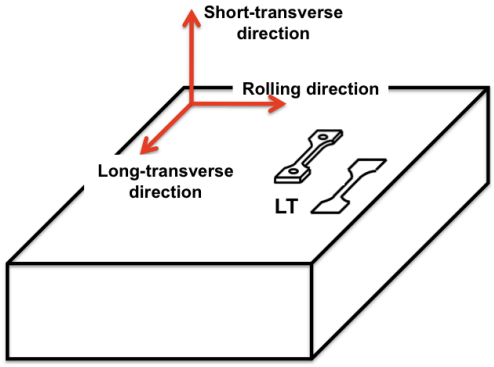

Fig. 3.6. In-plane sampling directions of tensile specimens.

Fig. 3.7(a) & (b) show the strain-stress diagram of Alloy 617 and Alloy 230, respectively. Generally, the alloys can withstand high stresses during tensile testing at temperatures up to 700ºC. Above 800ºC, the effect of strain hardening is significantly weakened. The stress rapidly decreases once it reaches the yield point. Particularly at 900 and 1000ºC, strain hardening can hardly be observed. Fig. 3.8 shows the measured tensile properties for Alloy 617 and Alloy 230. The strengths at various temperatures are analogous for both alloys. From RT to 800ºC, both alloys maintained a relatively high yield strength

(Y.S. >250 MPa) with a slight decline with increasing temperature. Similarly, the decrease in ultimate tensile strength (U.T.S.) from RT to 700ºC is moderate. At higher temperatures (>900ºC for Y.S. & >800ºC for U.T.S), both alloys were unable to withstand a large stress. (Fig. 3.7) Hence, a notable loss of strength was found for these temperatures. (Fig. 3.8)

It should be noted that the tensile responses for Alloy 617 using miniature specimens are analogous to properties found during experiments using standard size specimens [53, 123], indicating little if any size effects.

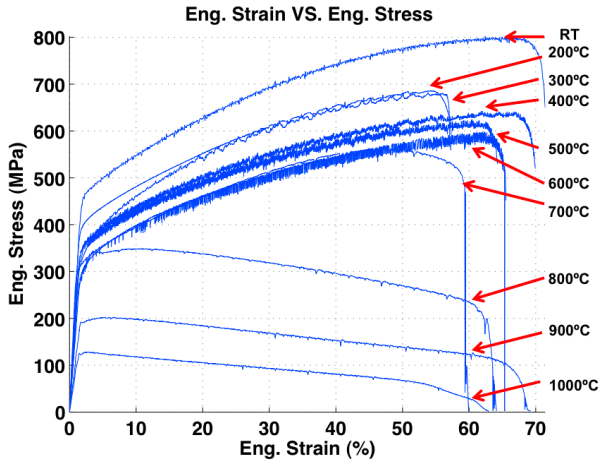

(a)

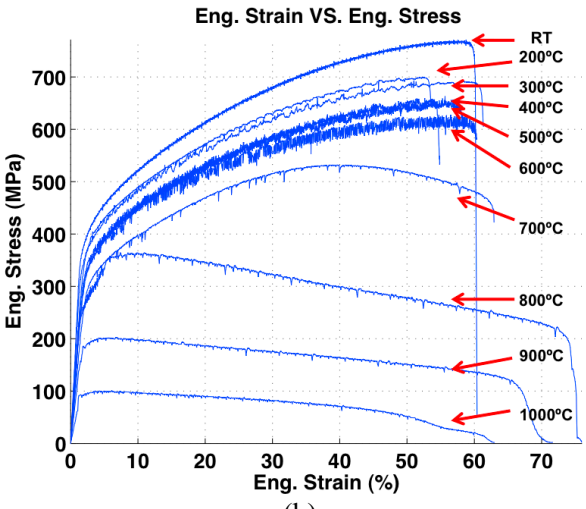

(b)

Fig. 3.7. Strain-stress diagrams of (a) Alloy 617 (b) Alloy 230

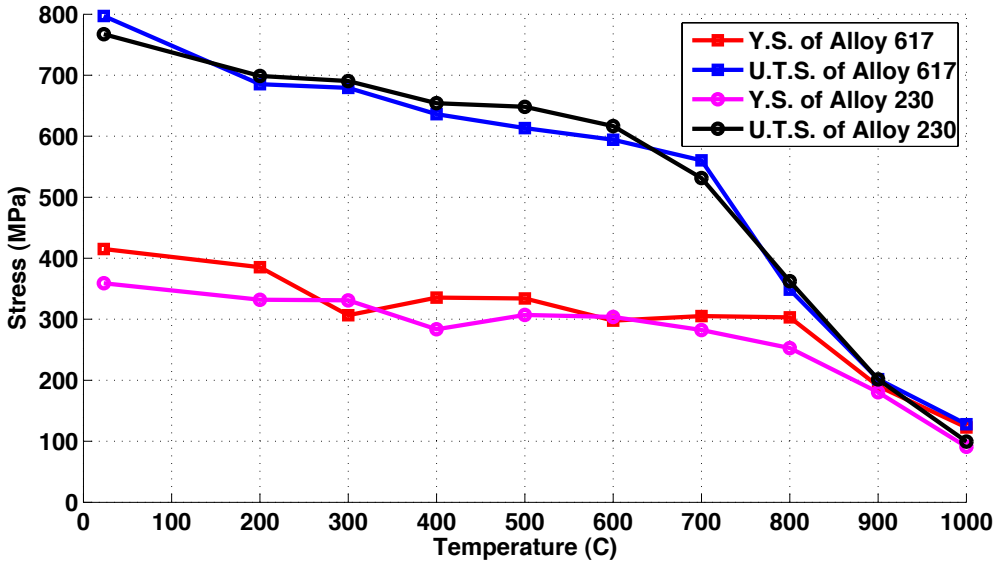

Fig. 3.8. Tensile properties (yield strength (Y.S.) and ultimate tensile strength (U.T.S.)) of Alloy 617 and Alloy 230 at various temperatures

3.2.1 TENSILE RESPONSE FROM ROOM TEMPERATURE TO 700ºC

At room temperature, the strain-stress curve is smooth and continuous without apparent serrations. With increasing testing temperature, the strain-stress curve becomes serrated and unstable. (Fig. 3.7) These serrated strain-stress curves can be described by the *Portevin-LeChatelier effect*. During plastic deformations, dislocations become locked by solute atoms (e.g. interstitial carbon atoms) and can only be released when sufficient external stress is applied. This "drag and release" process is displayed by the serrated flow in a strain-stress curve. Since the flow stress can temporarily increase during external loading, this phenomenon is called *dynamic strain aging*, which suggests that aging occurs during deformation. [124] For both alloys, the *dynamic strain aging* is evident at temperatures ranging from 300 to 600ºC. (Fig. 3.7) Fig. 3.9 shows the flow stresses at selected temperatures for both alloys. The amplitude for the stress oscillation is found to be slightly higher for Alloy 230 than Alloy 617. (Table 3.2) For both alloys, the amplitude of serrations is found to increase with studied temperature because of higher atom diffusibility attained at higher temperatures.

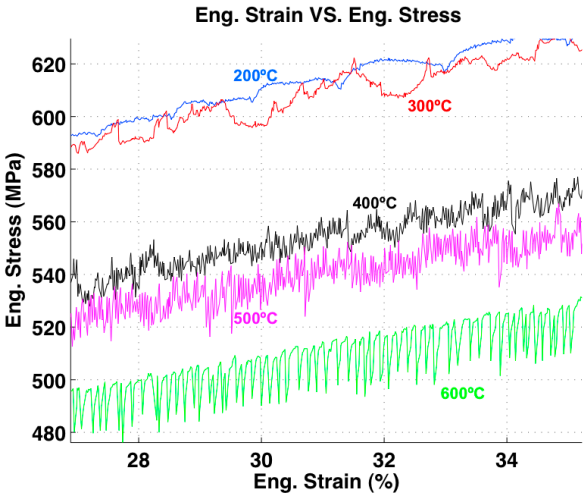

(a)

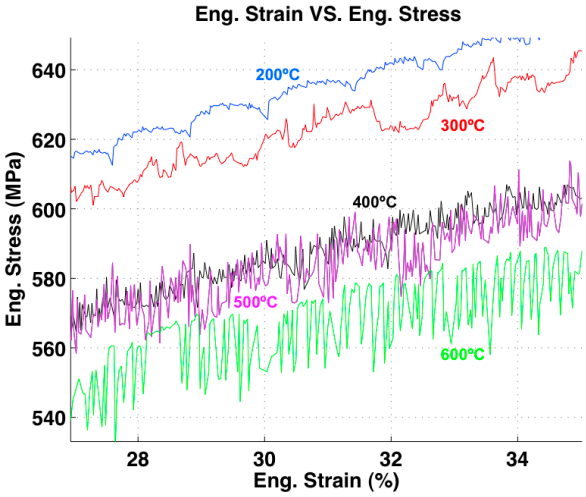

(b)

Fig. 3.9. *Portevin-LeChatelier effect* on (a) Alloy 617 (b) Alloy 230

Table 3.2. Amplitude of flow stress oscillations of Alloy 617 and Alloy 230 (in MPa)

Temperature (ºC)	300	400	500	600
Alloy 617	8	10	15	18
Alloy 230	8	10	16	20

3.2.2 Tensile Response from 800ºC to 1000ºC

The previous analysis of tensile response at intermediate temperatures cannot be applied to higher temperature regions (> 800ºC) because of the involvement of additional deformation mechanisms and the accompanying loss of strain hardening. For both alloys, 800°C can be considered the *equicohesive temperature*. [125] Above this temperature, grain

boundaries are unable to impede dislocation movement. Hence, matrix grains and grain boundaries have comparable strength. High-temperature creep induced by thermal assisted dislocation glide and climb becomes a major deformation mechanism. The changes in deformation behavior at different temperatures are evaluated from observations of fracture micromechanism. (Fig. 3.10) During tensile testing at temperatures below 800ºC, dislocations in the alloys do not have sufficient mobility to climb over carbide particles. Instead, they pile up on the interphase boundaries between matrix and carbide particles. (Fig. 3.11) Nevertheless, as the number of dislocations increases, sufficiently large stresses are generated and placed on the particles. Then, the particles begin to crack and produce voids during plastic deformation. (Fig. 3.10(a)) The coalescence of the crack voids finally results in pre-mature failure during testing. This can be seen in the strain-stress diagram for temperatures up to 600ºC (Fig. 3.7), which shows that elongation is small beyond the maximum stress (U.T.S) (i.e. little necking occurs). In contrast, dislocations attained a high thermal-activated mobility at elevated temperatures (>700ºC for Alloy 617 and Alloy 230). At these high temperatures, particle pinning is not as effective and efficient as at low temperatures because many dislocations with enhanced mobility are able to bypass the particles by dislocation creep or cross-slip. Furthermore, dislocation boundaries (incidental dislocation boundaries (IDB's) in the small scale or geometrically necessary boundaries (GNB's) in the large scale) can transform into low-angle grain boundaries during high-temperature deformation. This process of recrystallization releases the strained areas closed to the interphase boundaries, and thus decreases the stresses that are placed on the particles. As a result, few particle crack voids were observed at temperatures above 700ºC for both alloys. Instead, intergranular fracture initiated by triple junction cracks became the major fracture mechanism. (Fig. 3.10(b)) Intergranular fracture is a combined result of grain boundary sliding (controlled by dislocation creep) and grain boundary cavitation. Cavity formation was found to depend on the locally applied stresses and grain boundary surface energy that related to the coherence of the boundary. The cavity formation can be described by the critical radius for stable cavity development, r_c, where $r_c = 2\gamma_s/\sigma$, and γ_s is the grain boundary surface energy and σ is the

local tensile stress normal to the grain boundary. [114] Due to a relatively high strain rate and corresponding high stress level, grain boundary cavities formed and coalesced to produce grain boundary cracks. Failure finally occurred at wedge cracks located at grain boundary triple points. (Fig. 3.10(b))

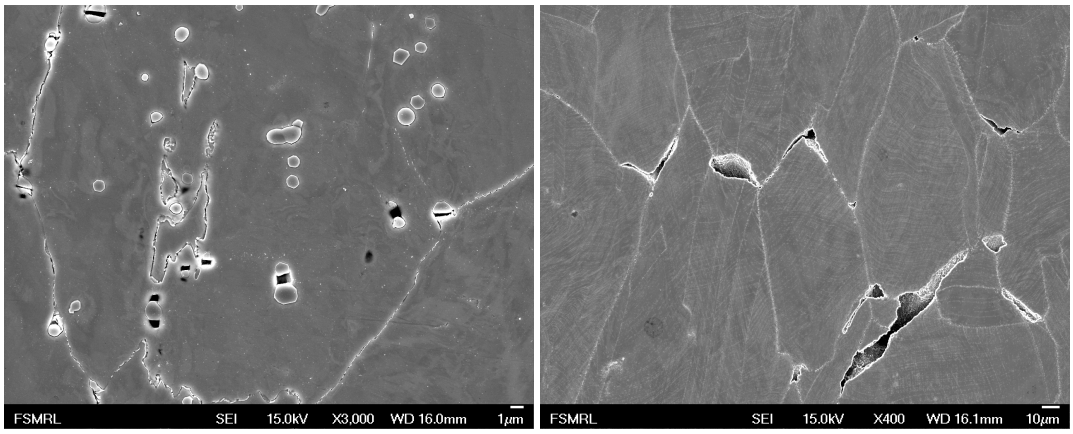

(a) (b)

Fig. 3.10. Fracture micromechanisms: (a) particle cracks at 200ºC (b) triple point cracks at 800ºC

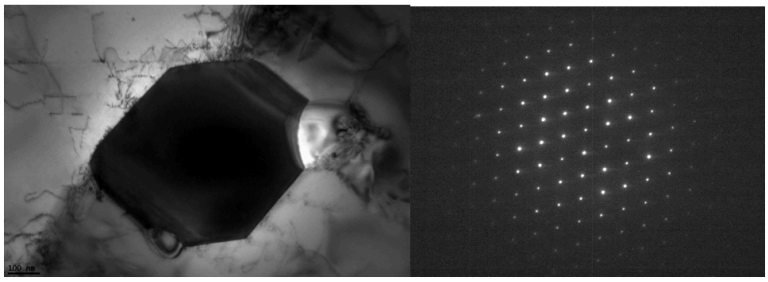

(a) (b)

Fig. 3.11. $M_{23}C_6$ in Alloy 617 with dislocations: (a) Bright field image (b) Diffraction pattern (B=[011])

Another important phenomenon that occurs during high-temperature deformation is dynamic recrystallization (DRX). Fig. 3.12 shows the SEM and EBSD analyses of a tensile specimen after testing at 800ºC. In order to differentiate between the recrystallized grains and inclusions and precipitates, both alloy matrix grains and carbides were scanned, recognized and mapped by EBSD. (Fig. 3.12(b) & Fig. 3.12(c)) A very small number of recrystallized grains with a size of ~1 μm or smaller were found in grain boundaries near a triple point

crack. No apparent recrystallization was seen in other areas. This indicates that dynamic recrystallization rarely occurs during plastic deformation at 800ºC.

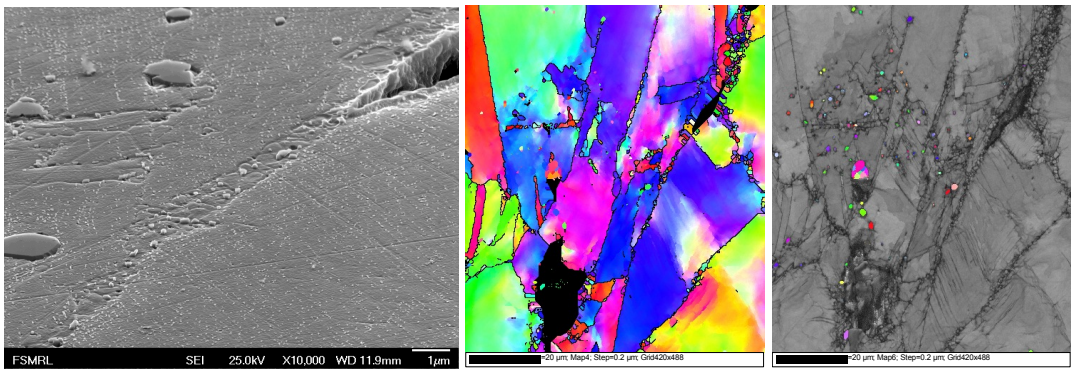

(a) (b) (c)

Fig. 3.12. DRX in the tensile test at 800ºC: (a) SEM image of a grain boundary with a crack (b) EBSD mapping showing the crystal orientations (c) EBSD sampling of the inclusion particles ($M_{23}C_6$)

Fig. 3.13 shows dynamic recrystallization during tensile testing at 1000ºC. Due to a higher temperature, both the number and the size of recrystallized grains are much larger compared to 800ºC. The recrystallized grains possess various crystal orientations, whereas the adjacent large grains attain a developed texture (e.g. <111>) after plastic deformation. Additionally, a great number of twin boundaries are generated during dynamic recrystallization due to low stacking fault energy (SFE) in Alloy 617. [126] Compared to a large fraction of recrystallized grains in the necking area (Fig. 3.13(b)), dynamic recrystallization that occurs 2 mm beyond the necking area is less intense (Fig. 3.13(a)) with a smaller number of recrystallized grains. This detail indicates the factor of strain on dynamic recrystallization: higher strain in the necking area promotes dynamic recrystallization. Fig 3.13(b) & (c) show a great number of fine grains that nucleated in an inclusion-rich area. The high volume fraction of carbide particles and small grain sizes strengthen this area by impeding dislocation movement. Hence, higher dislocation density and more subgrain structures are developed in an inclusion-rich area. During high-temperature deformation, subgrain structures can easily form new grains by the transformation of subgrain boundaries into low-angle grain boundaries. [127] In addition to the inclusion rich areas, original high-angle grain boundaries are another preferential region for dynamic recrystallization (the

'original' is used to differentiate the boundaries that existed before dynamic recrystallization from the boundaries formed by recrystallization).

During plastic deformation, a large number of original twin boundaries lose their coherence and develop into high ∑ or high angle boundaries. However, a very small number of recrystallized grains are found in these boundaries. This indicates that different DRX kinetics exist for different types of grain boundaries. Finally, although the strain was over 0.5 when the specimen ruptured, the recrystallized region was much smaller than the un-recrystallized area. This indicates that steady state recrystallized microstructure was not achieved.

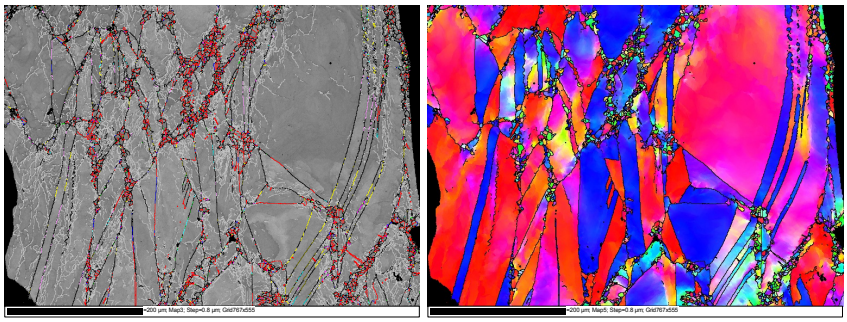

(a)

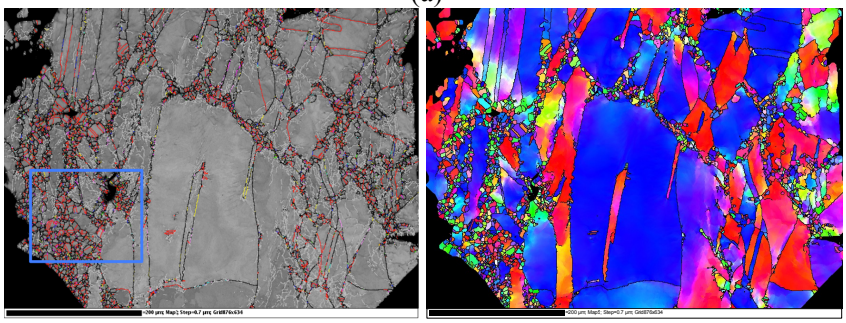

(b)

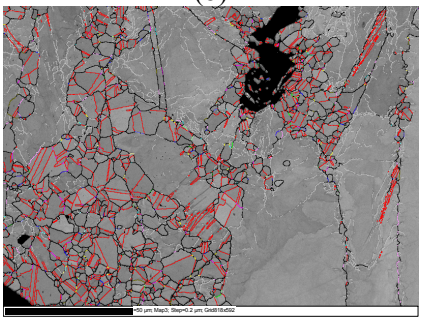

(c)

Fig. 3.13. DRX in the tensile test at 1000ºC: (a) 2 mm from the necking area (b) necking area (c) enlarged image of the selected area seen in (b)

3.3 EFFECT OF ORIENTATION

Although numerous studies have been conducted on the creep and corrosion resistance of Alloy 617 and Alloy 230, few researches have focused on the evaluation and characterization of the orientation effect on each alloy. The effect of orientation on mechanical properties is significant in terms of engineering design and safety, because the loss of strength in one direction can impact the integrity of required component shapes and cause localized failure. This effect can be exacerbated for components of the VHTR due to its harsh environment and long-term operation. [128] For instance, the recently proposed PCHE for use in the VHTR may induce a potential issue with respect to the mechanical directionality of the material. [48] Because of the block-shaped design of the PCHE, high-temperature material damages (e.g. creep or creep-fatigue) will not only occur along the gas flow channels, but they will also endanger the transverse direction of the heat exchanger. Unfortunately, the transverse/thickness direction usually possesses the weakest mechanical properties, so failure will be more likely to occur in this direction. Other components with special geometry in the VHTR, such as the thick wall tubes under high internal pressure [125], can also suffer the adverse effect of orientation with dramatically lowered strength in the transverse directions. It is therefore necessary for the engineering design of reactor components to measure the mechanical properties of a material in the transverse direction and clarify the source of anisotropy.

In order to study the effect of orientation, tensile testing on the plate form of Alloy 617 with various sampling directions was conducted at temperatures up to 1000ºC. The specimens were sampled from different orientations with respect to the long-transverse direction. (Fig. 3.14) Previous studies indicate that little or no deviation of mechanical properties exists between the rolling (longitude) and the long-transverse direction of Alloy 617. [129] Thus, the long-transverse direction was employed as a reference to study the mechanical anisotropy and associated microstructure gradients in Alloy 617.

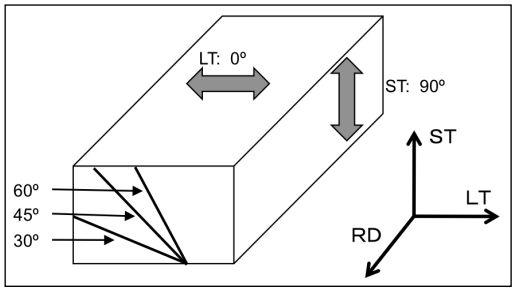

Fig. 3.14. In-plane sampling directions of tensile specimens

3.3.1 MECHANICAL ANISOTROPY

The results of tensile tests on Alloy 617 are presented in Fig. 3.15. The best tensile properties were observed from specimens in the long-transverse direction. Specimens in the other testing directions presented a comparatively lower strength. First, for specimens at 0º and 30º angles to the long-transverse direction, the difference in yield strength is ~60MPa from room temperature to 800ºC. The difference becomes much smaller for temperatures higher than 800ºC. Between 30º and 45º angles, the loss of yield strength is more moderate: ~20MPa on average from RT to 800ºC. Finally, yield strength does not show a noticeable change for the angles of 45º to 90º. Unlike the changes in yield strength, the ultimate tensile strength decreases at an approximately constant value from one angle to another. In other words, Alloy 617 shows a linear loss in tensile strength from the long-transverse (0º) to the short-transverse (90º) direction. It should be also noted that the loss in tensile strength is generally greater than the loss in yield strength.

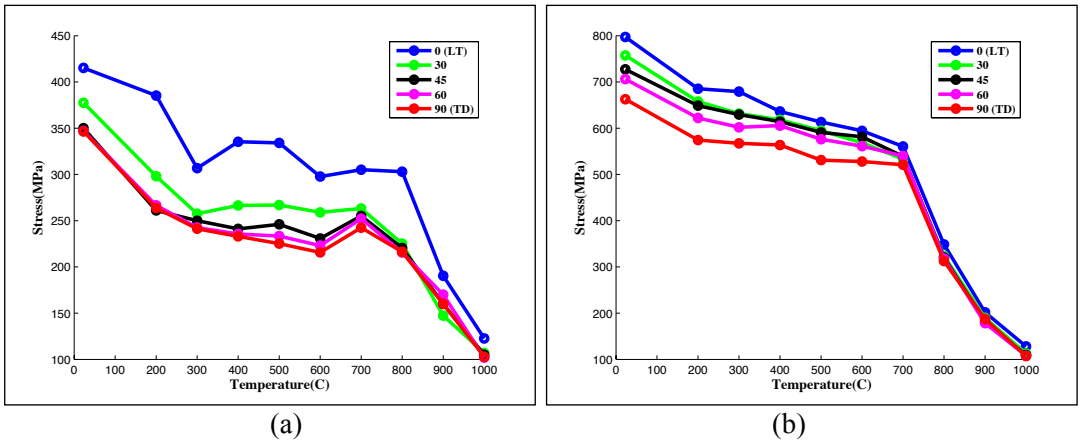

Fig. 3.15. Tensile properties versus temperature for various angles with the long-transverse direction: (a) Y.S. and (b) U.T.S.

Additionally, the temperature dependence of mechanical anisotropy is pronounced for Alloy 617. The difference in yield strength between the long-transverse and short-transverse directions is reduced from ~70MPa at room temperature to ~20MPa at 1000ºC. In tensile strength, the difference decreases from ~135MPa at room temperature to ~20MPa at 1000ºC. Note that the difference in magnitude of strength becomes much smaller for temperatures higher than 800ºC. (Fig. 3.15) Nevertheless, it is difficult to conclude that the effect of orientation diminishes as the temperature increases, because the absolute values of both the yield and tensile strength have already decreased. Therefore, a simple comparison of absolute strength values is insufficient to evaluate the anisotropy, since a small stress difference may be caused by a large fraction of strength reduction. Thus, in order to evaluate the strength as a fraction, the long-transverse strengths are employed as references. Hence, the relative Y.S. and U.T.S. can be expressed by equation 3-1 and 3-2, respectively.

$$\text{Relative Y.S.} = \frac{\text{Y.S. for a specific angle}}{\text{Y.S. in long - transverse direction } (\theta = 0º)} = \frac{\text{Y.S.}(\theta, \text{T})}{\text{Y.S.}(\theta = 0º, \text{T})} \qquad (3-1)$$

$$\text{Relative U.T.S.} = \frac{\text{U.T.S. for a specific angle}}{\text{U.T.S. in long - transverse direction } (\theta = 0º)} = \frac{\text{U.T.S.}(\theta, \text{T})}{\text{U.T.S.}(\theta = 0º,\ \text{T})} \qquad (3-2)$$

In the above equations, θ represents the angle from the long-transverse direction (θ = 0º(LT), 30º, 45º, 60º or 90º(ST)) and T is the studied temperature. Additionally, the mean value of the relative Y.S. and U.T.S. for all studied temperatures can be defined as:

$$\overline{\text{Relative Y.S.}} = \frac{\text{Mean value of Y.S. for a specific angle for all studied temperatures}}{\text{Mean value of Y.S. in long - transverse direction } (\theta = 0º) \text{ for all studied temperatures}} = \frac{\sum_{\text{T=RT}}^{1000ºC} \text{Y.S.}(\theta, \text{T})}{\sum_{\text{T=RT}}^{1000ºC} \text{Y.S.}(\theta = 0º, \text{T})}$$

$$\overline{\text{Relative U.T.S.}} = \frac{\text{Mean value of U.T.S. for a specific angle for all studied temperatures}}{\text{Mean value of U.T.S. in long - transverse direction } (\theta = 0º) \text{ for all studied temperatures}} = \frac{\sum_{\text{T=RT}}^{1000ºC} \text{U.T.S.}(\theta, \text{T})}{\sum_{\text{T=RT}}^{1000ºC} \text{U.T.S.}(\theta = 0º,\ \text{T})}$$

The mean values of relative strength are calculated to study the overall effect of orientation for the entire range of studied temperatures. Meanwhile, these mean values serve as standards of comparison for the relative Y.S. and U.T.S. at different temperatures.

Fig. 3.16 shows the results of the analysis of relative strength. Similar to the changes in absolute strength, the relative yield strength decreases rapidly once the sample orientation is not parallel to the rolling planes. The relative yield strength maintains a small value for angles between 45º and 90º. The relative tensile strength exhibits a linear relation with respect to the orientation with the long-transverse direction. These results agree well with the analysis of absolute strength at lower temperatures. However, the difference in relative strength between the long-transverse direction and the other studied angles at high temperatures does not diminish as observed for the trend in absolute strength. The loss in yield strength in the short-transverse direction is ~17% at both room temperature and 1000ºC, slightly less than the mean value of ~22% ('AVG' in Fig. 3.16(a)). The loss in tensile strength in the short-transverse direction at room temperature, 300ºC, and 1000ºC has a similar value of ~17%, which is also close to the mean value ('AVG' in Fig. 3.16(b)). Therefore, even though the difference in absolute strength between the long-transverse and short-transverse directions is much smaller at high temperatures, the difference in relative strengths is comparable to the value at low temperatures. This indicates that the effect of orientation on the mechanical properties at high temperatures is analogous to that at low temperatures.

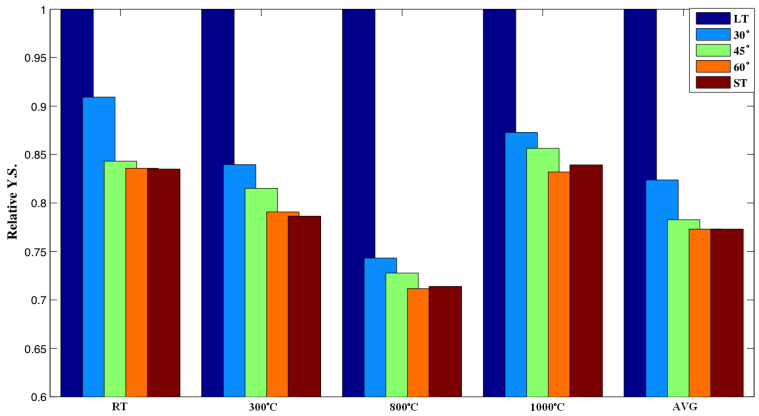

(a)

Fig. 3.16. Relative strengths of Alloy 617: (a) relative Y.S. (b) relative U.T.S

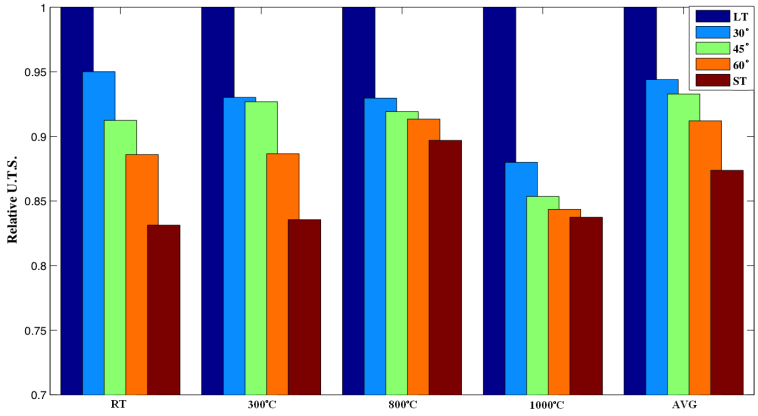

(b)

Fig. 3.16. Cont.

3.3.2 MICROSTRUCTURE ANISOTROPY

The triplanar montage generated from SEM images exhibits the microstructure gradients in the three principle directions. (Fig. 3.17) A great number of intrinsic carbide inclusions, composed of coarse $M_{23}C_6$ type carbides with a small amount of Ti(C,N), are presented as white spots in Fig. 3.17. These carbides are shown as bands on the transverse plane (TP) and longitudinal plane (LP) and grouped as clusters on the rolling plane (RP).

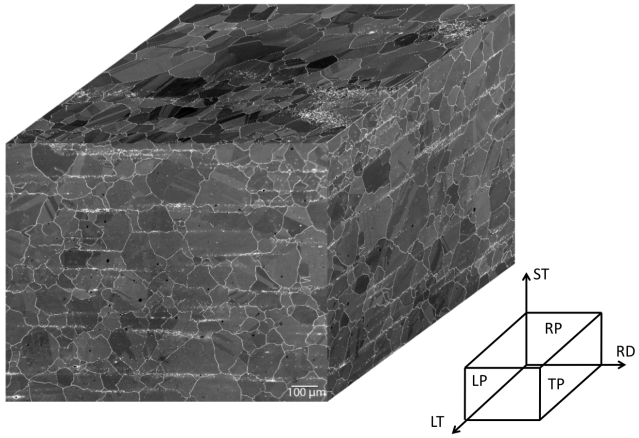

Fig. 3.17. Triplanar montage illustrating the grain structure and inclusions in the as-received condition. The rolling direction (RD), short transverse (ST) direction, long transverse (LT) direction, rolling plane (RP), transverse plane (TP) and longitudinal plane (LP) are noted.

The EBSD mappings for the rolling and transverse plane are shown in Fig. 3.18(a) & (b), respectively. Similar to the band-shaped distribution of inclusion particles (Fig. 3.17), the

alignment of crystals in the transverse plane appears to be parallel to the rolling plane. Most small grains are located near carbide bands. The lamellar-shaped inclusions and the associated fiber-shaped grain distributions are known as mechanical fibering. [114, 125] The EBSD analysis also shows that both coarse and fine grains are randomly oriented, indicating no intrinsic texture in the as-received Alloy 617. (Fig. 3.19)

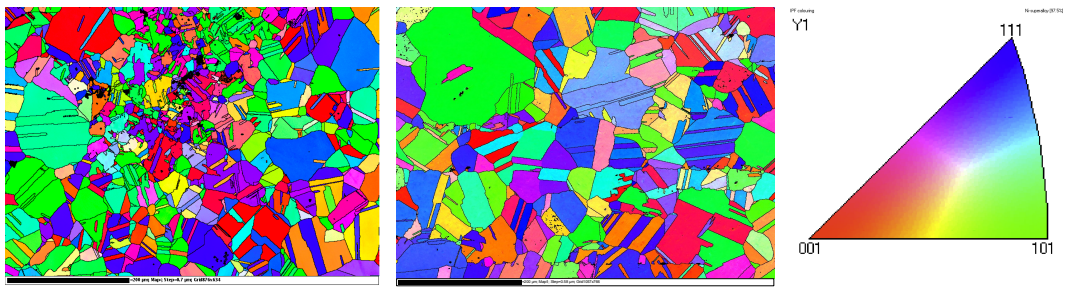

(a) (b) (c)

Fig. 3.18. EBSD analysis of Alloy 617 in the as-received condition: (a) rolling plane (b) transverse plane (c) legend

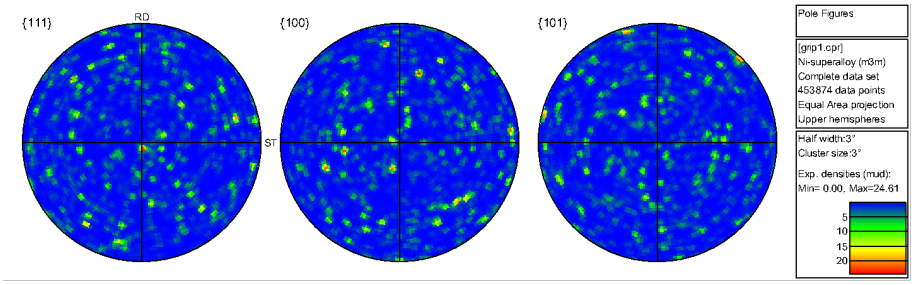

Fig. 3.19. Texture analysis for Alloy 617 in the as-received condition

Fig. 3.20 and Fig. 3.21 show the results of EBSD analyses for the long- and short-transverse specimens, respectively, those have been tensile tested at room temperature. The sampling area for each specimen is ~0.5 mm from the rupture edge. The crystallography in Fig. 20(a) and Fig. 21(a) shows that the dominant textures after plastic deformation are primary <111> and secondary <001> parallel to the tension direction (refer to the legend in Fig. 3.18(c)). A direct observation of the texture development in specimens comes from an intensity mapping in the pole figures. (Fig. 3.22) The long-transverse specimen showed a developed duplex texture: <111> + <001>. (Fig. 3.22(a)) In contrast, many more random

crystal orientations were observed in the short-transverse specimen, indicating that the material was not significantly deformed before rupture. (Fig. 3.22(b))

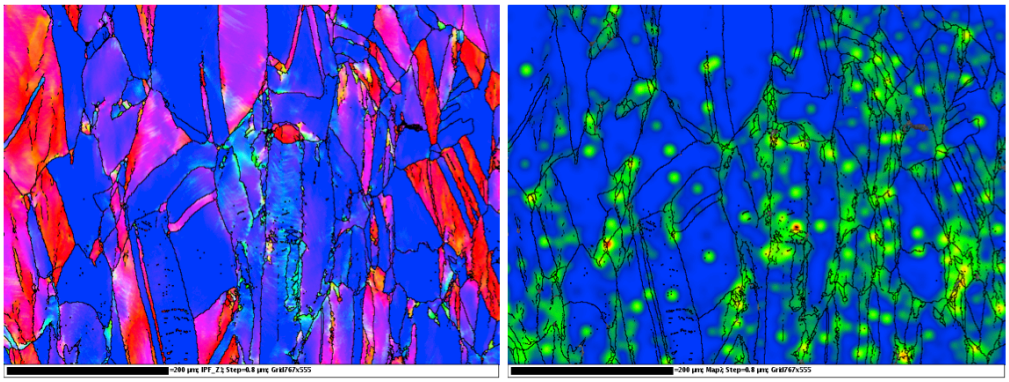

(a) (b)

Fig. 3.20. EBSD analysis for the long-transverse specimen after tensile testing at room temperature: (a) crystal orientation mapping (b) strain contouring

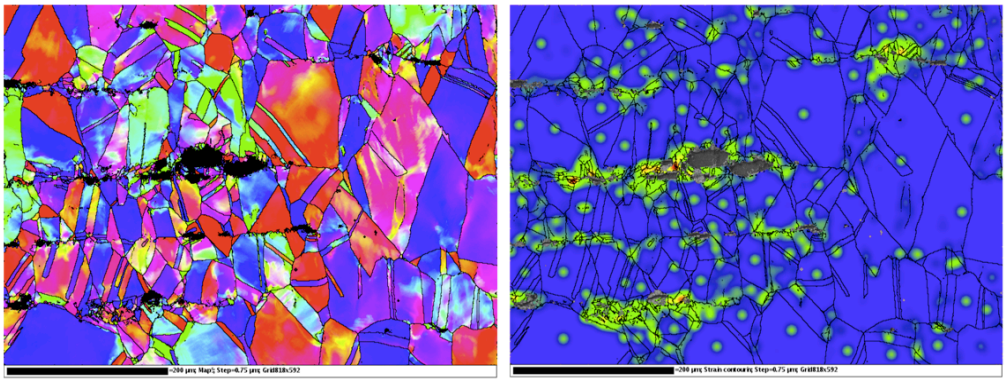

(a) (b)

Fig. 3.21. EBSD analysis for the short-transverse specimen after tensile testing at room temperature: (a) crystal orientation mapping (b) strain contouring

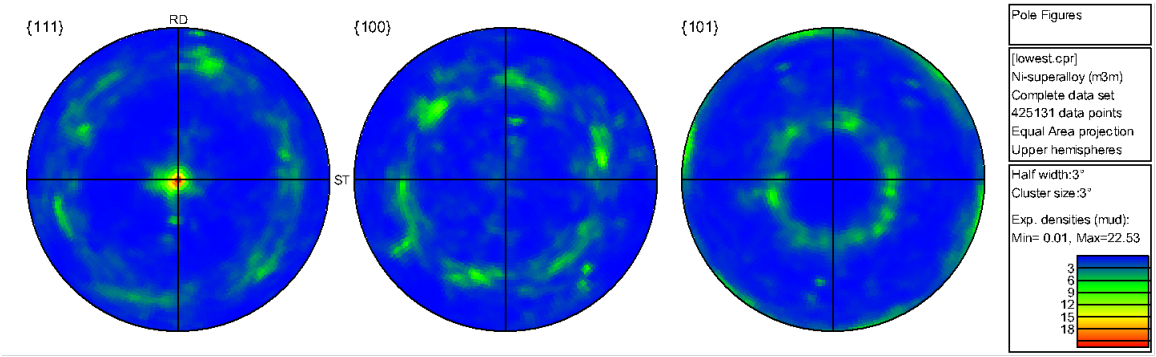

(a)

Fig. 3.22. Texture development after tensile testing at room temperature: (a) long-transverse direction (b) short-transverse direction

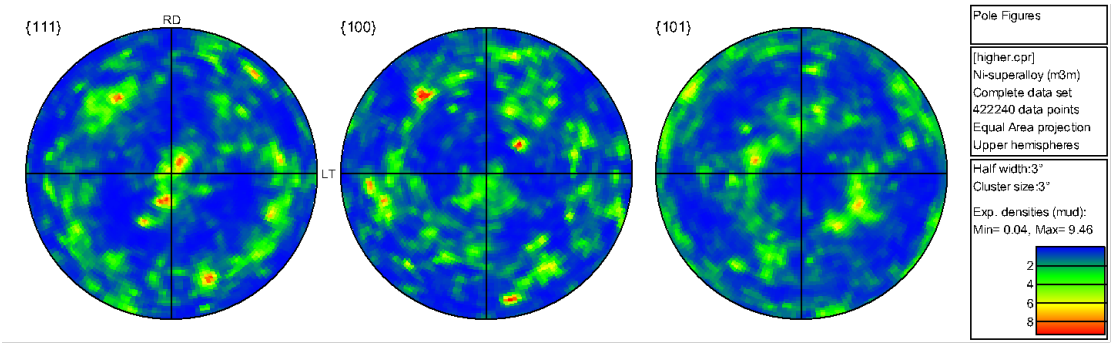

(b)

Fig. 3.22. Cont.

Beyond texture analysis, a more direct method, strain contouring, was employed to study orientation effects on deformation processes of Alloy 617. Based on the measurement of the maximum misorientation in a grain, strain contouring provides an estimate of the amount of strain in individual grains of a material. Detailed procedures for strain contouring can be found in ref. 130. The results of strain contouring for the long- and short-transverse specimens are shown in Fig. 3.20(b) and Fig. 3.21(b), respectively. The intensities of highly strained areas are represented by the red and green portions of the maps, with red signifying a greater intensity. Note that the highly strained areas are located close to the inclusion rich areas for both specimens. For the short-transverse specimen, the highly strained area is close to the large cracks generated by the rupture of the inclusion particles and thus appears perpendicular to the loading direction. (Fig. 3.21(b)) But for the long-transverse specimen, the highly strained area distributes parallel to the loading direction, because the inclusion rich area was slightly elongated along the loading direction during plastic deformation. (Fig. 3.20(b))

Following thermal aging for a specimen, microstructural analysis can provide additional information to understand the effect of orientation. Alloy 617 develops $M_{23}C_6$ type precipitates during high-temperature aging. These carbide particles nucleate, diffuse, and coarsen with aging before they finally stabilize in favorable nucleation sites (e.g. interphase and high-angle grain boundaries). [131, 132] (Detailed discussion of this aging effect will be given in the next chapter.) SEM images show that the grain boundaries of Alloy 617 become

decorated with continuous intergranular carbide “chains” following thermal aging. (Fig. 3.23) These chains were broken at grain boundaries during plastic deformation. Fig. 3.23 shows a specimen of Alloy 617 aged for 300 hours at 1000ºC before undergoing a tensile test at room temperature. The tension direction is parallel to the short-transverse direction (perpendicular to the inclusion bands in the picture). During the test, the intergranular carbide chains became disconnected in areas lying between two inclusion bands, indicating that the plastic deformation essentially localized in these areas. The disconnection of the carbide chains and corresponding grain boundary elongation confirm the EBSD microstructural analyses for the short-transverse specimen. These phenomena also reveal the fact that the only strongly deformed areas are the areas between inclusion bands, and the inclusion bands constrain the plastic flow and result in highly strained areas (with large misorientation relative to a whole grain) close to inclusion particles.

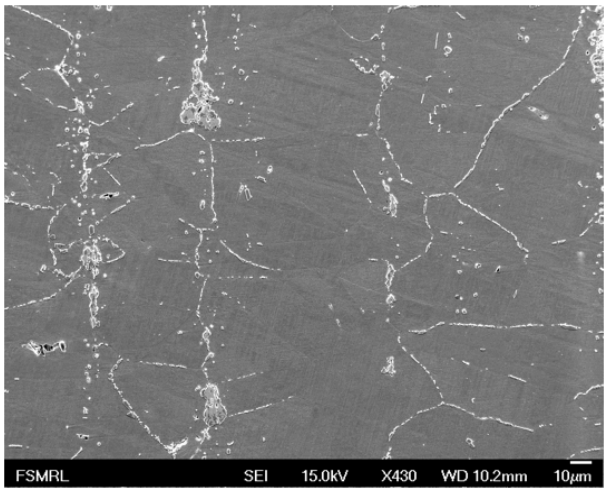

Fig. 3.23. SEM micrograph of a fractured sample of Alloy 617 aged at 1000ºC for 300 hours

Above 800ºC, the flow stress is found to rapidly decrease once the yield stress is reached. Strain hardening is weakened due to the enhanced dislocation mobility. Additional deformation mechanisms, including dislocation creep and dynamic recrystallization (DRX) are also induced at high temperatures. The effect of orientation on the deformation process for high temperatures is therefore different from that for low temperatures. At a high temperature (e.g. 1000ºC) strains near the inclusion particles can be released by additional deformation

mechanisms (e.g. dynamic recrystallization). However, the effect of orientation is not subsequently weakened according to the analysis of relative strengths. (Fig. 3.16) Fig. 3.24 shows the EBSD mapping of a short-transverse specimen after a tensile test at 1000ºC. Compared to a large fraction of recrystallized grains found in the long-transverse specimen (Fig. 3.13), recrystallized grains in the short-transverse specimen developed into another feature: a smaller number of grains with larger grain size. Nevertheless, similar to the long-transverse specimen, many recrystallized grains were found in the area close to the inclusion particles for the same reason given in section 3.2.2.

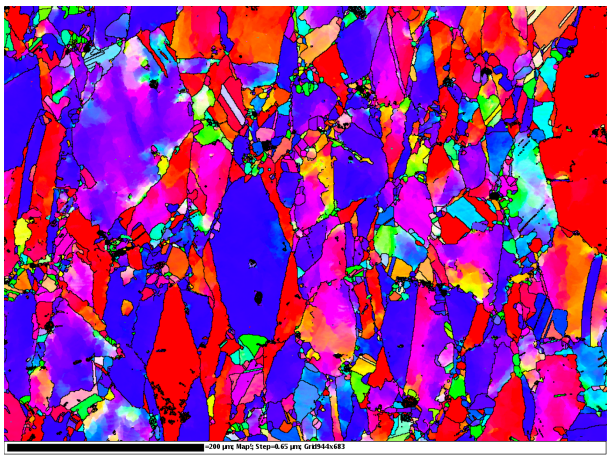

Fig. 3.24. Dynamic recrystallizations in a short-transverse specimen after tensile testing at 1000ºC

3.3.3 FRACTOGRAPHY

Fractography provides a direct approach to study the various fracture processes of specimens at various angles. Fig. 3.25 shows the fractography of specimens following tensile testing at room temperature. For the specimens at 0º and 30º angles with the long-transverse direction, each individual grain can be clearly indentified in the fracture surface, indicating an approximate intergranular fracture. (Fig. 3.25(a) & (b)) For the specimen at 45º, “dimples” with slightly elongated troughs arise due to microvoids generated by the shear stress acting on the carbide particles. (Fig. 3.25(c)) “Dimples” with equiaxed microvoids can be found in the specimens at 60º and 90º (the short-transverse direction). (Fig. 3.25(d) & (e)) These microvoids are formed in association with fractured inclusion particles and rapidly expand

under approximately uniaxial stresses. The results show that the impact of mechanical fibering is relatively small for low angles (0º and 30º), but becomes significant for higher angles (45º, 60º and 90º). The performed fractography analysis agrees well with mechanical tests and other microstructure analyses.

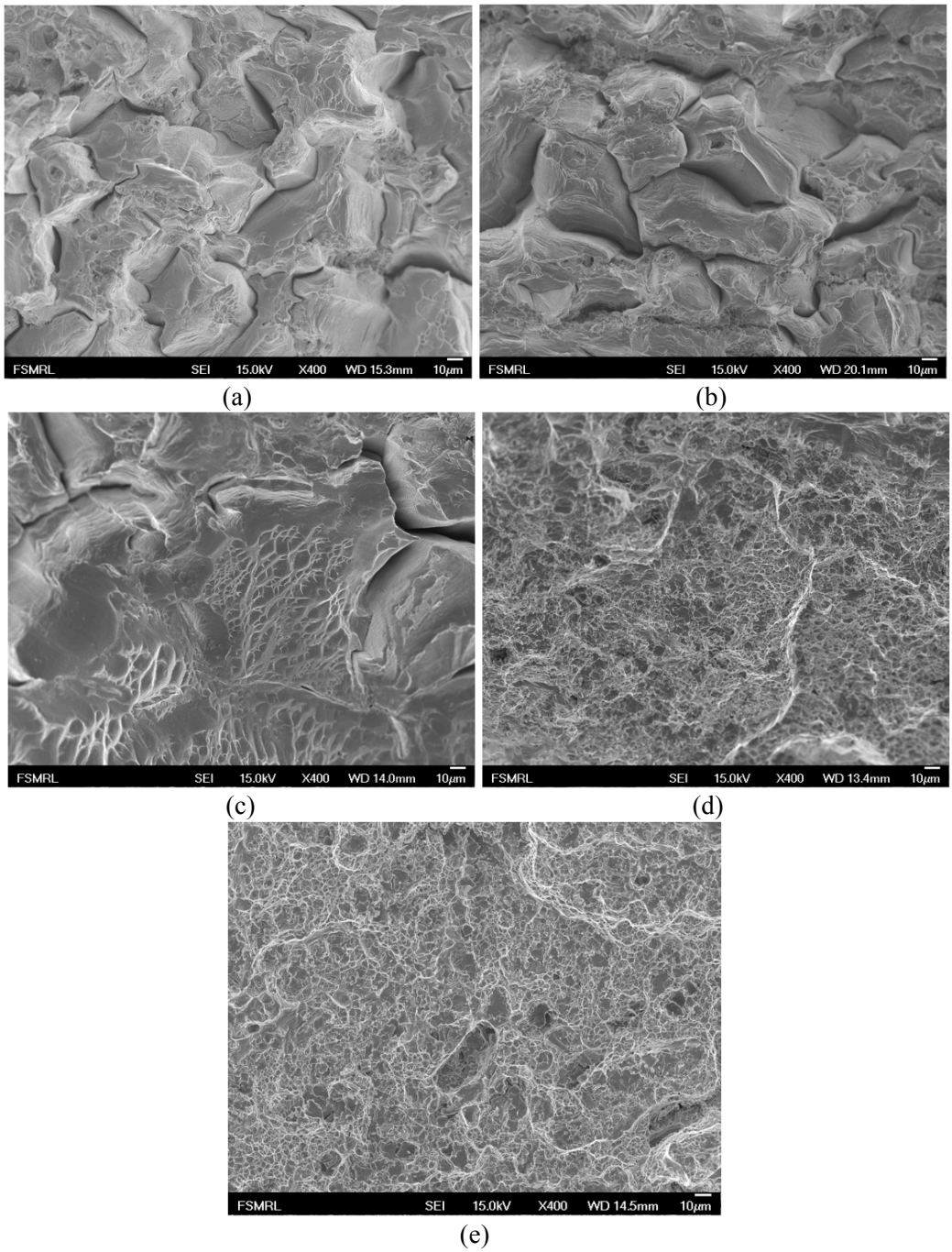

Fig. 3.25. Fractography after tensile testing at room temperature: (a) 0º (long-transverse direction) (b) 30º (c) 45º (d) 60º (e) 90º (short-transverse direction)

3.3.4 DISSCUSSION

Differences in yield strength in various directions indicate an intrinsic Bauschinger effect in the Alloy 617 plate. [133] Previous studies of hot-rolled aluminum alloy plates revealed a similar phenomenon, with little observed change in strength in the rolling and long-transverse directions, but a considerable loss of strength in the short-transverse direction. [133] A comparison of the relative strengths of Alloy 617, Alloy MA754 (an oxide dispersion strengthened nickel-based alloy), and two aluminum alloys is shown in Fig. 3.26. The data for Alloy MA754 is taken from a bar with a transverse section of 90 x 32 mm. [134] The data for aluminum alloys is taken from plates with thickness of ~2 to 2.5 inch. [133] The loss of relative yield strength in the short-transverse direction in Alloy 617 was found to be over 15%, which is larger than the values (<10%) for MA 754 and the aluminum alloys. Hence, the effect of orientation is an important issue in the plate form of Alloy 617 and must be taken into account during engineering design.

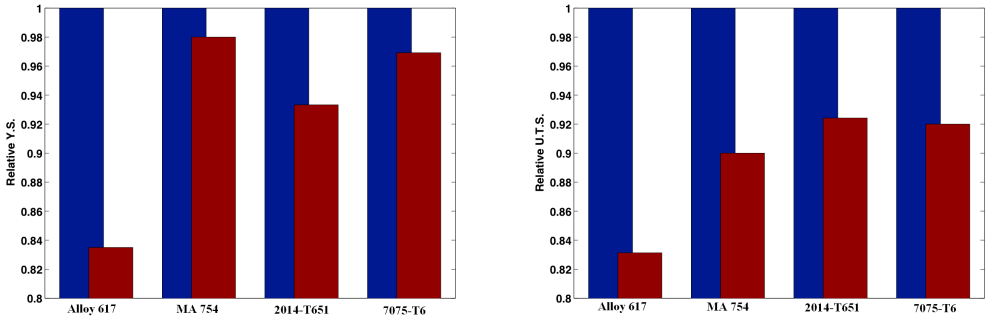

(a) (b)

Fig. 3.26. Relative strengths of various alloys at room temperature: (a) Y.S. (b) U.T.S

Two main sources of anisotropic material properties can typically be found in polycrystalline materials. [135] The first source is material texture produced by strong deformation (e.g. cold work) that develops a preferred crystal orientation, such as (110)<112> rolling texture (α brass type) in the sheet form of face-centered cubic (FCC) metals. [125] The second source is mechanical fibering composed of an alignment of inclusion particles and matrix crystals. Compared to cold rolled products, hot rolled metals and alloys generally have more isotropic mechanical properties. Solid solution annealing after hot work also helps to

minimize residual stresses. Therefore, no obvious texture is observed in the as-received Alloy 617. (Fig. 3.19) Instead, significant mechanical fibering is found in the plate form of Alloy 617 and results in the directionality of mechanical properties. During hot rolling, the inclusion particles were generated with asymmetric shapes and spatial distributions. The growth of recrystallized grains was subsequently restricted by inclusion particles, and thus the new grains presented a specific alignment. Additionally, the inclusion particles were not re-dissolved during solid solution annealing. As a result, the microstructure characterized by inclusion and crystal fibers, or mechanical fibering, was preserved after solid solution treatment. Therefore, this microstructure that is composed of carbide bands in the transverse direction can be found extensively in the plate form of Alloy 617. [33, 34, 40, 136, 137]

Mechanical fibering in Alloy 617 also contributes to an anisotropic microstructure that is developed during tensile testing. The high volume fraction of carbide particles impedes the dislocation movement and consequently causes dislocation pileups and a high density of subgrain structures surrounding the particles. Therefore, as seen in strain contouring, the highly strained areas are concentrated on the interphase boundaries. (Fig. 3.20(b) & Fig. 3.21(b)) In the short-transverse direction, this phenomenon is amplified due to the steep strain gradient. The region between two inclusion bands can be easily deformed, whereas the area close to inclusion is hardened by grain and interphase boundaries. Hence, the plastic deformation is localized. This can be seen in an aged specimen of Alloy 617 where intergranular carbide chains were disconnected between two carbide bands as a result of localized deformations. (Fig. 3.23) However, the situation changes for elevated temperatures. Due to the thermal-enhanced mobility of dislocations and atoms, subgrain boundaries can transform into grain boundaries and develop new grains. The number, size, and distribution of recrystallized grains are dependent on plastic strain. The highly strained area during plastic deformations, which is also the inclusion rich area in Alloy 617, is subjected to increased dynamic recrystallization. This explains why the dynamic recrystallized grains are distributed in the same way as the strain contouring at low temperatures. (Fig. 3.20(b) & Fig. 3.21(b))

Another important result of mechanical fibering is the initiation of pre-mature failure by the ligaments of carbides bands in a tension loading. This was found to only occur at temperatures lower than 700ºC. At higher temperatures, fracture was initiated by triple junction cracks from grain boundary sliding. The early rupture of the short-transverse specimens can be observed by its undeveloped texture. During the plastic deformation of Alloy 617 at low temperatures, crystallographic planes tend to rotate to form <111> or <100> textures to minimize easy glide. The amount of crystals oriented to be parallel to the <111> or <100> direction (texture development), can be used to examine the level of plastic deformations. A fully developed texture in the long-transverse specimen of Alloy 617 indicates that the material experienced a strong deformation during tensile testing. (Fig. 3.22(a)) In contrast, the texture was found to be undeveloped in the short-transverse specimen, seen as a relatively smooth intensity distribution in the pole figures. (Fig. 3.22(b))

Finally, the effect of orientation can also be magnified in the creep condition for Alloy 617. Totemeier and Lillo reported that specimens of MA 754 have a comparable tensile strength in the transverse direction to the strength value in the longitudinal direction; however, a markedly lower transverse strength was found in the creep condition. [134] Thus, the effect of orientation for the structure materials is important for long-term, high temperature environments in the VHTR, where creep damage will occur. Significant effort should be placed into minimizing the effect of orientation and even eliminating the source of anisotropy in Alloy 617. High temperature annealing is a simple method to remove the inclusion particles. Kihara et al. reported that all of the inclusion particles in Alloy 617 were dissolved following aging at 1200ºC for 20 hours. [39] However, the new grain size for the aged Alloy 617 was 0.36 mm, or more than twice the value of the as-received condition. Creep resistance increases as a result of increased grain size; however, the yield strength of the aged alloy likely decreases due to the loss of strengthening by the fine grains. The corresponding loss in yield strength may fail to meet American Society for Testing and Materials (ASTM) standards. [138] Hence, it will be a challenge task to remove inclusion particles from Alloy 617 by high temperature annealing and still maintain its strong mechanical properties.

The analysis of the orientation effect will be continued in Chapter 5. High-energy synchrotron radiation will be employed to study the anisotropic loading behavior of carbides and the γ matrix individually in Alloy 230.

3.4 EFFECT OF STRAIN RATE

The strain rate applied to a material during a tensile test can have a significant impact on flow stress. The strain rate is defined as $\dot{\varepsilon} = d\varepsilon / dt$ and is expressed in units of s^{-1}. For most metallic materials, a higher strain rate generally results in a higher flow stress. In the other words, increasing the strain rate in mechanical tests can increase the yield stress, and vice versa. [125] This strain rate dependence of flow stress is controlled by the applied temperature. Generally, metallic materials are more sensitive to strain rate at higher temperatures. Since Alloy 617 and Alloy 230 are expected to be used at high temperatures, up to 1000ºC, the effect of strain rate must be well examined before any practical application can take place.

3.4.1 STRAIN RATE SENSTIVITY ANALYSIS

The true stress (σ_t) and true strain (ε_t) can be found in terms of engineering stress (σ_e) and engineering strain (ε_e) by:

$$\sigma_t = \sigma_e(1+\varepsilon_e) \qquad (3-3)$$

$$\varepsilon_t = \ln(1+\varepsilon_e) \qquad (3-4)$$

The true strain rate, $\dot{\varepsilon}_t$, is the rate of change in true strain (ε_t) with respect to time (t), and is defined by:

$$\dot{\varepsilon}_t = \frac{d\varepsilon_t}{dt} = \frac{d[\ln(L/L_0)]}{dt} = \frac{dL/dt}{L} = \frac{v}{L}, \qquad (3-5)$$

where v is the crosshead velocity, L is the instantaneous gage length, and L_0 is the initial gage length. Most tensile tests are conducted at a constant engineering strain rate ($\dot{\varepsilon}_e$), so it is more convenient to relate the true strain rate and engineering strain rate by:

$$\dot{\varepsilon}_t = \frac{v}{L} = \frac{d\varepsilon_e / dt}{(1+\varepsilon_e)} = \frac{\dot{\varepsilon}_e}{1+\varepsilon_e} \qquad (3-6)$$

When the applied engineering strain is small (e.g. ε_e = 0.002), the difference between $\dot{\varepsilon}_e$ and $\dot{\varepsilon}_t$ is negligible. Hence, $\dot{\varepsilon}_t$ can be replaced by $\dot{\varepsilon}_e$ when studying the effect of strain rate on the yield stress. In the following discussion, the general form $\dot{\varepsilon}$ is used to replace $\dot{\varepsilon}_e$ and $\dot{\varepsilon}_t$.

The relationship between flow stress and strain rate at a constant strain and temperature is given as:

$$\sigma_t = C(\dot{\varepsilon})^m, \qquad (3-7)$$

where *m* is the *strain-rate sensitivity* and *C* is a fitting constant. This equation can be rewritten as:

$$\frac{\sigma_1}{\sigma_2} = \left(\frac{\dot{\varepsilon}_1}{\dot{\varepsilon}_2}\right)^m, \qquad (3-8)$$

where σ_1 and σ_2 are the flow stresses during testing at strain rates of $\dot{\varepsilon}_1$ and $\dot{\varepsilon}_2$, respectively. Thus, *m* can be obtained to be:

$$m = \frac{\log(\frac{\sigma_1}{\sigma_2})}{\log(\frac{\dot{\varepsilon}_1}{\dot{\varepsilon}_2})} \qquad (3-9)$$

In order to obtain a sufficient data set to study the *strain-rate sensitivity*, tensile tests for Alloy 617 and Alloy 230 were conducted at two different strain rates: 0.01s^{-1} and 0.05s^{-1} in addition to previous tests completed at 0.001s^{-1}. Fig. 3.27 shows the strain-stress diagrams of Alloy 617 for three different temperatures: 200ºC, 800ºC and 1000ºC, representing low, high and very high temperatures. At 200ºC, the flow stress was found to be insensitive to applied strain rates. (Fig. 3.27(a)) Nevertheless, the flow stress substantially increased at 800 and 1000ºC while increasing the applied strain rate. This relationship shows the temperature dependence of the effect of strain rate for Alloy 617.

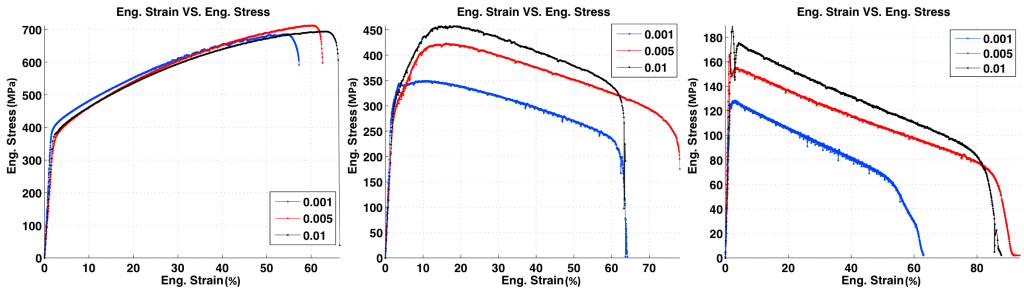

(a) (b) (c)

Fig. 3.27. Engineering strain-stress diagram for Alloy 617 at: (a) 200ºC (b) 800ºC (c) 1000ºC

The complete results for the tensile tests are given in APPENDIX A. The value of *m* is determined by measuring the slope of a plot of $\log(\dot{\varepsilon})$ versus $\log(\sigma)$. (Fig. 3.28) The measured *strain-rate sensitivities* for 0.2% flow stress for Alloy 617 and Alloy 230 are given in Table 3.3 and 3.4, respectively. For Alloy 617, the value of *m* is small (< 0.1) from room temperature to 800ºC. A notable increase in *m* occurs at 900 and 1000ºC with a value exceeding 0.17. For Alloy 230, the value of *m* is close to 0 for low temperatures. The only exception occurs at room temperature with a value of *m* of ~ 0.15. Similar to the Alloy 617, the *strain-rate sensitivities* for Alloy 230 are much higher at 900 and 1000ºC.

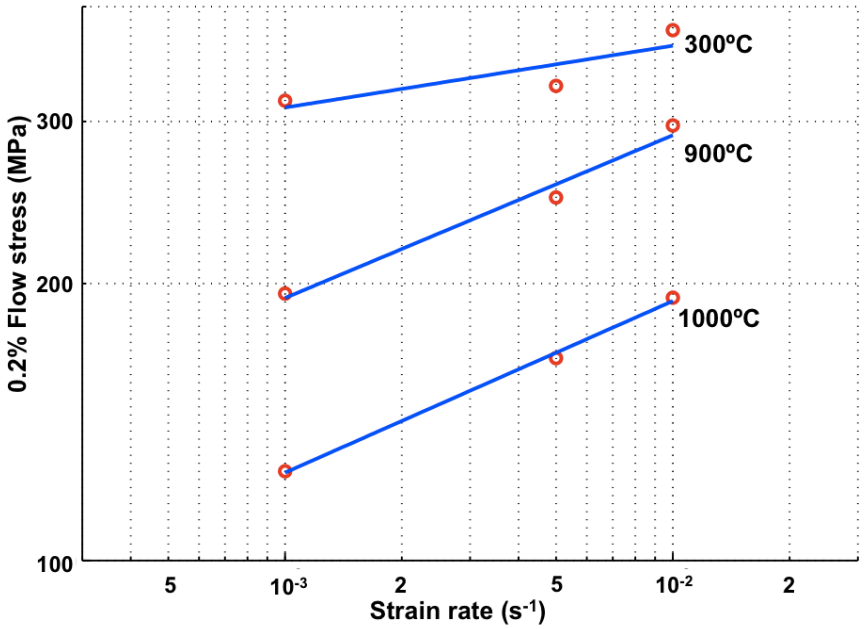

Fig. 3.28. 0.2% flow stress versus strain rate for Alloy 617.

Table 3.3. 0.2% flow stresses for Alloy 617 at temperatures from RT to 1000ºC

Temperature (ºC)	$\dot{\varepsilon}_t = 0.001$	$\dot{\varepsilon}_t = 0.005$	$\dot{\varepsilon}_t = 0.01$	m
RT	460	470	500	0.031
200	385	374	380	-0.00785
300	316	328	377	0.06
400	339	340	341	0.003
500	328	305	367	0.03
600	303	306	344	0.047
700	298	323	373	0.088
800	283	285	300	0.022
900	195	248	297	0.1772
1000	125	166	193	0.1866

Table 3.4. 0.2% flow stresses for Alloy 230 at temperatures from RT to 1000ºC

Temperature (ºC)	$\dot{\varepsilon}_t = 0.001$	$\dot{\varepsilon}_t = 0.005$	$\dot{\varepsilon}_t = 0.01$	m
RT	367	470	515	0.1483
200	350	397	360	0.023
300	336	330	352	0.014
400	305	380	350	0.07
500	336	340	305	-0.03
600	315	335	316	0.007
700	289	292	297	0.01
800	250	270	230	-0.02
900	190	255	250	0.1304
1000	93	150	205	0.34

As discussed in section 3.2, the flow stress rapidly decreases once it reaches the yield point at high temperatures (800-1000ºC). The true strain-stress diagram shows that the plastic flow becomes stabilized with an approximately constant flow stress during the plastic regime. (Fig. 3.29 & 3.30) This constant flow stress characterized by strain independence was found to be sensitive to the applied temperature and strain rate. Thus, the *strain-rate sensitivities* for the constant flow stress can be interpreted from the true strain-stress diagrams (Fig. 3.29 & 3.30). The results of the analysis are shown in Table 3.5 & 3.6 for Alloy 617 and Alloy 230, respectively.

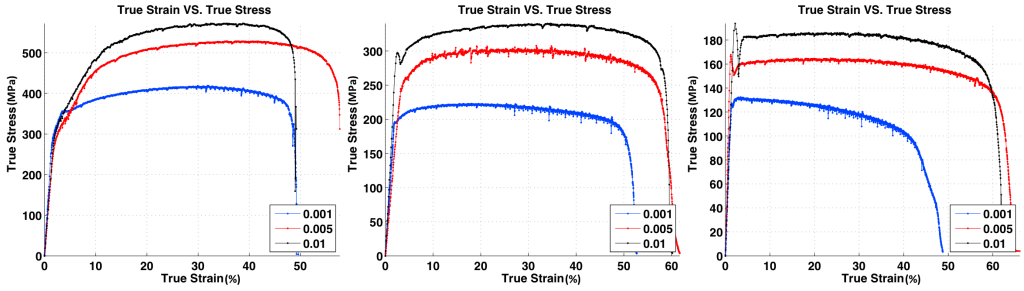

(a) (b) (c)

Fig. 3.29. True strain-stress curves for Alloy 617 at temperature: (a) 800ºC (b) 900ºC (c) 1000ºC

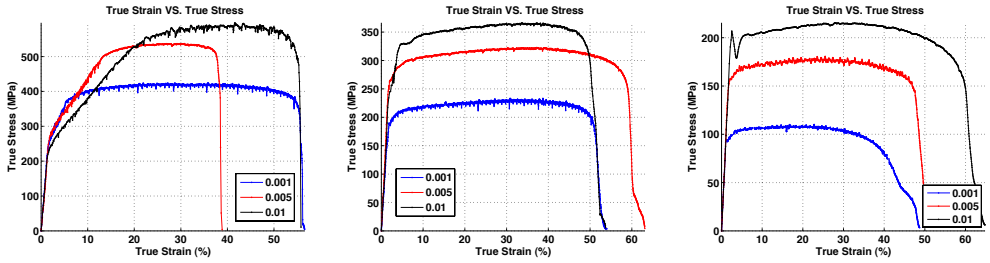

(a) (b) (c)

Fig. 3.30. True strain-stress curves for Alloy 230 at temperature: (a) 800ºC (b) 900ºC (c) 1000ºC

Table 3.5. Constant flow stress for Alloy 617 at temperatures from 800 to 1000ºC

Temperature (ºC)	$\dot{\varepsilon}_t = 0.001$	$\dot{\varepsilon}_t = 0.005$	$\dot{\varepsilon}_t = 0.01$	m
800	413	523	565	0.138
900	220	300	336	0.1855
1000	131	163	184	0.146

Table 3.6. Constant flow stress for Alloy 230 at temperatures from 800 to 1000ºC

Temperature (ºC)	$\dot{\varepsilon}_t = 0.001$	$\dot{\varepsilon}_t = 0.005$	$\dot{\varepsilon}_t = 0.01$	m
800	417	535	586	0.149
900	227	320	364	0.2065
1000	108	176	214	0.298

3.4.2 DISCUSSION

The measured *strain-rate sensitivities* are plotted in Fig. 3.31 (a) & (b) for Alloy 617 and Alloy 230, respectively. Note that the blue points are interpreted from constant flow stresses at high temperatures. For each alloy, the *strain-rate sensitivity* does not linearly increase with temperature. The value of *m* is small at low temperatures (RT to 700ºC),

showing a strain rate independence of flow stress for both alloys. The only exception is a higher value of *m* that occurs at room temperature for Alloy 230. This temperature independence of the strain-rate sensitivity is attributed to *dynamic strain aging*. As discussed in section 3.2, *dynamic strain aging* can cause abnormal work-hardening that can be reflected in irregularities in strain-stress diagrams (*the Portevin-LeChatelier effect*). Moreover, *dynamic strain aging* can cause flow stresses to be independent of both strain rate and temperature. [124] For the temperature intervals in which *dynamic strain aging* occurs, there is a maximum degree of work hardening that corresponds to a specific strain rate at one temperature. A specimen deformed at the intermediate strain rate can experience a higher degree of work hardening compared to specimens deformed either at a lower or a higher strain rate. This can be seen in the results of tensile testing in Table 3.3 & 3.4 (or the strain-stress diagrams in APPENDIX A). For some studied temperatures (e.g. 300ºC for Alloy 230), the flow stress at a strain rate of $0.005s^{-1}$ was found to be even higher than the stresses at a strain rate of $0.001s^{-1}$ and $0.01s^{-1}$. Due to this irregular strain rate independence, the *strain-rate sensitivities* are measured to be close to zero at temperatures below 800ºC for both alloys.

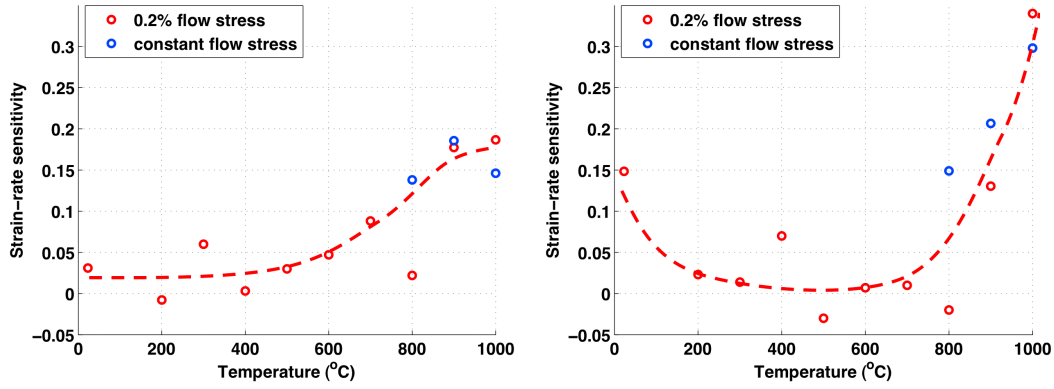

Fig. 3.31. Strain-rate sensitivity versus temperature up to 1000ºC for (a) Alloy 617 (b) Alloy 230. Note that the blue points are interpreted from constant flow stresses.

The *strain-rate sensitivity* for 0.2% flow stress was found to decrease at 800ºC, but increase considerably at 900 and 1000ºC. In fact, 800ºC is treated as a critical temperature for both Alloy 617 and Alloy 230, not only because it is the *equicohesive temperature*, but also due to the carbide precipitation that occurs at this temperature (Fig. 3.10(b)). The precipitate

hardening can be seen by comparing the strain-stress diagrams of 700 and 800ºC: the curves in the inelastic regions have a stiffer slope at 800ºC compared to 700ºC. (Fig. 3.32) The flow stress during early yielding is significantly impacted by precipitate hardening. Thus, the influence of applied strain rate is relatively weakened. (Fig. 3.32(b)) However, due to higher mobility, dislocations are able to climb over particles when the applied stress is sufficiently large. As a result, the plastic flow becomes stabilized after the alloys experience maximum stress. (Fig. 3.29(a) & 3.30(a))

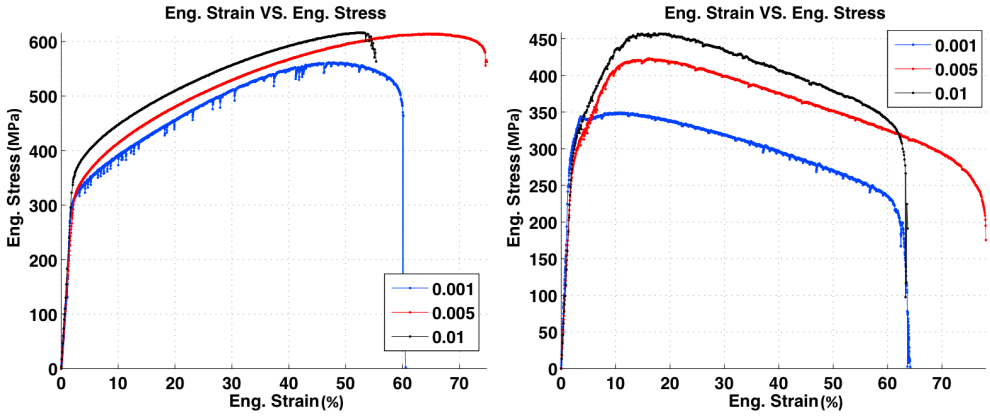

(a) (b)

Fig. 3.32. Engineering strain-stress diagrams for Alloy 617 at temperature: (a) 700ºC (b) 800ºC

Since the constant flow stresses observed at 800 to 1000ºC are nearly independent of strain, it is more convenient and accurate to interpret the *strain-rate sensitivities* from the constant flow stresses. For both alloys, the value of *m* under constant flow stresses increased with temperature except at 900ºC for Alloy 617. (Fig. 3.31) The *strain-rate sensitivity* is slightly higher at 900ºC compared to 1000ºC. (Fig. 3.32) The small difference can be caused by a measurement error, but more importantly, it suggests that the *strain-rate sensitivity* is very close for 900 and 1000ºC for Alloy 617. From the comparison between Fig. 3.31(a) and 3.31(b) (or Table 3.5 & 3.6), one should note that Alloy 230 is more sensitive to strain rate at high temperatures. Therefore, a small decrease in loading rate can cause a large reduction in strength in Alloy 230.

The *strain-rate sensitivity* has been found to be nearly a constant value for a wide range of strain rates. This has been found for the 6063 aluminum alloy: a constant *strain-rate*

sensitivity on the 0.2% flow stress in the strain rate ranging from 2×10^{-2} to 2×10^{-5} s^{-1}. [139] Therefore, it is possible to extend short-term material properties to approximate long-term loading response by using the *strain-rate sensitivity*. Based on equation 3-8 (assuming 1% total elongation according to the ASME limit), constant flow stresses during a long-term (up to 60 years) loading are calculated and shown in Table 3.7 & 3.8 for Alloy 617 and Alloy 230, respectively. The allowable stresses interpolated from the data obtained in the ASME codes are also provided for comparison. First of all, if the alloys are considered for use up to 60 years, current allowable stresses for the expected operation temperatures of the VTHR (800 to 1000ºC) are overestimated, except for the stress for Alloy 617 at 1000ºC. For Alloy 617, the allowable stresses are in fact higher than those for the estimated constant flow stresses for one year. This suggests that the alloy loading at a constant strain rate for one year (strain rate: $\sim 3 \times 10^{-10} s^{-1}$) can still maintain allowable stresses. However, when loading for a very long time (i.e. 60 years, strain rate: $\sim 5 \times 10^{-12} s^{-1}$), the material cannot withstand the allowable stresses, and instead it will rupture before the end of service life. This prognosis is even worse for Alloy 230 due to its higher value of *strain-rate sensitivity*. For a one-year estimation, the allowable stress is higher than the constant flow stress for 800 and 900ºC, but it is already lower than the value for 1000ºC. For an estimation of 10 years, the allowable stresses in all studied temperatures were found to be lower than their estimated stresses. The analysis suggests that current ASME allowable stresses for both alloys cannot be directly applied to high-temperature, long-term design. In fact, only a short-term application can use the established codes.

Table 3.7. Estimated constant flow stresses and ASME allowable stresses for Alloy 617

Temperature (ºC)	1 Year	10 Years	60 Years	ASME allowable
800	52.5 MPa	38.2 MPa	29.8 MPa	~31 MPa
900	13.7 MPa	9.0 MPa	6.4 MPa	~12.3 MPa
1000	14.6 MPa	10.4 MPa	8.0 MPa	~4.8 MPa

Table 3.8. Estimated constant flow stresses and ASME allowable stresses for Alloy 230

Temperature (ºC)	1 Year	10 Years	60 Years	ASME allowable
800	44.9 MPa	31.9 MPa	24.4 MPa	~32 MPa
900	10.4 MPa	6.4 MPa	4.4 MPa	~10.2 MPa
1000	1.3 MPa	0.6 MPa	0.4 MPa	~2.6 MPa

In addition to the evaluation of allowable stresses, the rupture stresses in the ASME code were also examined. The rupture stresses for Alloy 617 were developed in the ASME code case N-47-28. The interpolated rupture stresses for 1, 10 and 60 years are shown in Table 3.9. Generally, both estimated flow stresses and documented rupture stresses possess an analogous degradation tendency with time. For 800 and 1000ºC, the ASME rupture stresses are more conservative with lower values compared to the estimated flow stresses. In contrast, the ASME rupture stresses are lower than the estimated flow stresses at 900ºC, which can be attributed to measurement error. In general, the rupture stresses from the ASME code should be sufficiently conservative according to the *strain-rate sensitivity* analysis. One should note that there is a knockdown factor for rupture stress in the ASME code for engineering design. This design limit stands as '67% of rupture stress', which has been incorporated in the ASME B&PV Code, Section III, Subsection NH. Therefore, the permitted stresses for 60 years are only 7.3 and 3.0 MPa for 900 and 1000ºC after applying the knockdown factor. These permitted stresses are not adequate for long-term VHTR operation. Further engineering improvement and material development are needed to meet the requirements of the VHTR.

Table 3.9. Rupture stresses for Alloy 617 interpolated from Ref. 10 (ASME code case N-47-28)

Temperature (ºC)	1 Year	10 Years	60 Years
800	58 MPa	35 MPa	26 MPa
900	25 MPa	15 MPa	11 MPa
1000	11 MPa	6.8 MPa	4.5 MPa

CHAPTER 4

HIGH-TEMPERATURE AGING STUDY

Aging experiments can provide essential information for predicting material degradation during long-term, high-temperature applications. During long-term aging, the microstructure evolution, including grain growth, phase transformation and precipitate ripening, significantly influences the materials' mechanical properties [8]. For nickel alloys, precipitation and coarsening of secondary phases make up the dominant features of microstructure evolution during high-temperature aging. Since the type, size and coherence of precipitates depend on the composition of the material, the microstructure development during aging is unique for different alloys. In order to gain a better understanding of the high-temperature degradation process of the candidate materials for the IHX and provide practical data for its engineering design, long-term (up to 3000 hours) aging experiments were carried out to investigate the microstructural evolution for Alloy 617 and Alloy 230 at 900 and 1000ºC. Microstructural analysis showed a process of carbide particle precipitation, growth and maturation for both alloys. The corresponding changes in mechanical properties (hardness and tensile properties) on post-aging samples were also examined. The results agreed well with the expected microstructural development.

4.1 OVERVIEW

4.1.1. MICROSTRUCTURAL CHARACTERISTICS

High-temperature thermal aging of metallic materials often causes a microstructural evolution characterized by phase transformation, precipitate development, crystallite growth, etc. Phase transformation usually requires relatively high temperatures and fundamentally changes material properties. Similarly, significant grain growth only occurs at very high temperatures and results in decreased material strength. Both phase transformation and grain

growth generally occur during heat treatment in order to achieve a required nature of material and should be avoided in practical engineering applications.

Another typical microstructural development in thermal aging is nucleation and growth of second phase particles. Modern metallurgy often employs many different elements into commercial alloys in order to improve various material properties (e.g. alloying Al and Cr for corrosion resistance or W and Mo for high-temperature resistance). The alloying process required a solution treatment: heating the alloy into the single-phase field followed by a rapid quench. Thus, although the concentration of solute elements becomes supersaturated, and the phase diagram predicts mixtures with two or more phases, the alloy presents only a single phase due to the quench and a slow diffusivity of heterogeneous elements at low temperatures. Nevertheless, this insufficiency of atomic diffusion breaks down when the alloy is heated to higher temperatures below the solvus temperature. Significant thermal-enhanced diffusivity of the solute results in the precipitation of second-phase particles within matrix grains or at their respective grain boundaries. Depending on various equilibrium/thermal conditions, the precipitation can happen at a relatively wide range of temperatures and often involves the relevant temperature region for engineering applications.

The development of second-phase particles is often described as a process of nucleation, growth and coarsening. After the alloy is heated up to an aging temperature, the supersaturated elements begin to diffuse and coalesce into clusters. Then the fine, second-phase particles begin nucleating within the matrix grains or in their respective grain boundaries. Meanwhile, the newly formed particles grow at the expense of smaller particles. Once an equilibrium condition is achieved, the volume faction of the second-phase particles no longer increases, and the nucleation process is finished. Nevertheless, the particle growth continues in order to reduce the total free energy of the system by decreasing the total amount of interfacial area between phases. This process is known as Oswald ripening. The growth of the particles can last for a very long time with a decreasing coarsening rate until a relatively stable microstructure is achieved. This steady state condition can be considered the coarsening stage of thermal aging.

For Alloy 617 and Alloy 230, four types of particles were found in previous studies after certain heat treatments. [9] These particles are: $M_{23}C_6$, M_6C, Ti(N,C) & γ' (Ni_3Al). The former two types of particles are significant in the present study not only due to their prevalence over other types of particles in the materials, but also because they appear as precipitates during high-temperature (>900ºC) aging (particularly for the $M_{23}C_6$ type carbide). Due to the low fraction of titanium in both alloys (0.39% in Alloy 617 & <0.01% in Alloy 230), the amount of Ti (N,C) is so small that its impact on mechanical properties is almost negligible. Ti(N,C) can be detected in Alloy 617 by the observation of the color orange in optical microscopy, but it can hardly be found in Alloy 230 because of an even lower fraction of titanium. The typical dimensions of Ti (N,C) in the alloys is 10-100μm. γ' is the typical strengthening phase extensively found in nickel-based alloys. Many nickel-based superalloys (e.g. Inconel 718 and Haynes 282) are strengthened by additional aging treatment to obtain γ'. However, both Alloy 617 and Alloy 230 are solid-solution strengthening alloys that are not in purpose to employ γ' strengthening, although very small amounts of γ' have been reported in some aging studies of Alloy 617. [8] Moreover, γ' has never been found at temperatures higher than 900ºC in either alloy (also not found in the present study). The following discussion will focus on the $M_{23}C_6$ and M_6C carbides.

The $M_{23}C_6$ type carbide:

The $M_{23}C_6$ carbide was found in both Alloy 617 and Alloy 230 over the course of the study. This carbide has a complex, cubic structure with a large lattice parameter (> 1 nm). The structure of the $M_{23}C_6$ belongs to the space group $Fm\bar{3}m$, and the basic crystal structure is face-centered cubic (FCC). Fig. 4.1 shows the typical structure of the $M_{23}C_6$ carbide. It should be noted that although $M_{23}C_6$ is a chromium rich carbide, the rest of the composition of M can be made up of different metallic atoms, depending on the alloying elements in the material. In other words, partial contents of Cr in the original form of $M_{23}C_6$ (i.e. $Cr_{23}C_6$) can be substituted with Ni, Fe, Mn, Mo, W, etc. when these elements have been alloyed in the

material. Hence, the lattice parameter of $M_{23}C_6$ is not a fixed value, but instead falls in a range of 1.048-1.08 nm for Alloy 617. [40]

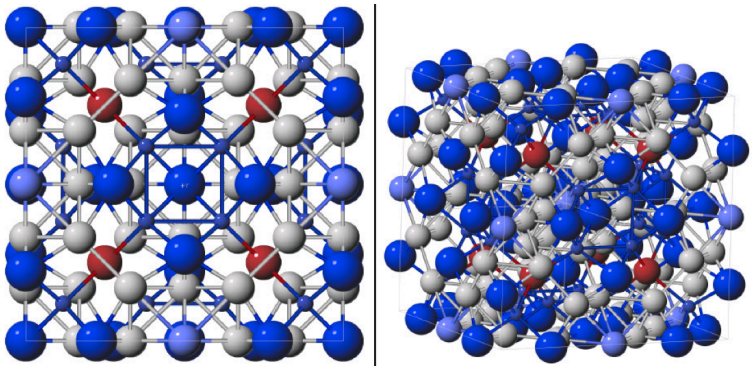

Fig. 4.1. Typical structure of $M_{23}C_6$ ($Cr_{12}Ni_8Fe_2Mn_1C_6$). In the diagram, large blue spheres: C atoms, small blue spheres: Ni atoms, red spheres: Fe atoms, light blue spheres: Mn atoms and gray spheres: Cr atoms. (pictures provided by the Center for Computational Materials Science of the United States Naval Research Laboratory). [140]

The M_6C type carbide:

The M_6C carbide was also found in both Alloy 617 and Alloy 230 during experimentation. Similar to the $M_{23}C_6$ carbide, the M_6C carbide also has a complex, cubic structure and a large lattice parameter. The structure of this carbide belongs to the space group $Fd\bar{3}m$, and the basic crystal structure is diamond cubic. Fig. 4.2 shows the typical structure of M_6C. Depending on the material composition, the contents of M in M_6C can be rich in Fe, Mo, Co, W, etc. The M_6C carbides in Alloy 617 and Alloy 230 were found to be rich in Mo and W, respectively. The lattice constant of the M_6C carbide is within a range of 1.085-1.175 nm for Alloy 617. [40] Compared to the $M_{23}C_6$ carbide, M_6C has a better thermal stability at high temperatures (800 to ~1200ºC). This property can be seen at equilibrium phases calculated by Thermocalc® [9, 10] showing that the $M_{23}C_6$ carbide is stable at temperatures up to 780ºC, but transforms into M_6C at higher temperatures (up to ~1200ºC, the solid solution temperature).

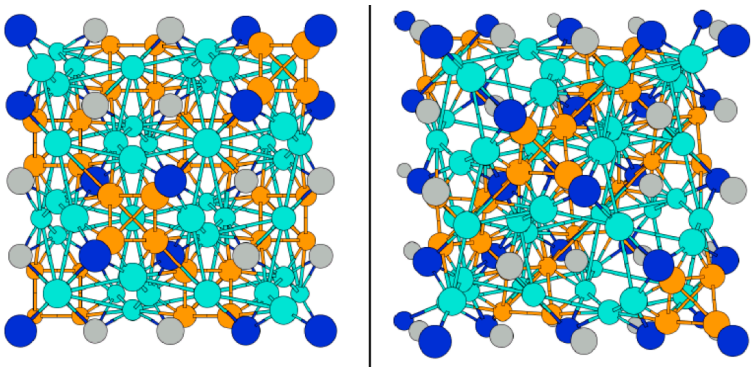

Fig. 4.2. Typical structure of M_6C ($W_3Fe_2CrC_6$). In the diagram, cyan spheres: W atoms, blue spheres: C atoms, orange spheres: Fe atoms and gray spheres: Cr atoms [140]

Both $M_{23}C_6$ and M_6C particles have been found in various alloys with moderate to high chromium content, including nickel-based alloys [131] and low carbon steels [112, 141]. Conventionally, both types of particles are believed to both add and detract from material performance. During high-temperature deformations, these particles can inhibit grain-boundary sliding (Zener pining) and increase the rupture strength of the material. However, premature failures can also be initiated by the fracture or decohesion of the particles. [142] Both $M_{23}C_6$ and M_6C type carbides have a high thermal stability at high temperatures in Alloy 617 and Alloy 230. The particles formed during heat treatment can withstand a temperature up to 1000ºC (even higher for M_6C). The thermal stability can be seen in calculated TTT diagrams [40] and equilibrium phase diagrams [9, 10]. It should be noted that $M_{23}C_6$ and M_6C carbides can react and transform according to the following chemical equation:

$$M_6C + M' \leftrightarrow M_{23}C_6 + M'', \qquad (4-1)$$

where, M' and M'' are substitute elements (e.g. Cr, Mo, Co, Fe, etc.)

In Alloy 617 and Alloy 230, the lattice constants for $M_{23}C_6$ and M_6C carbides are comparable, both of which are ~1.08 nm, or about three times the lattice constant of the γ matrix (~0.36 nm). Therefore, these particles can develop a cube-on-cube orientation with the host matrix (i.e. (100) carbide // (100) matrix, [001] carbide // [001] matrix). (Fig. 4.3) This semi-coherent structure is more pronounced for $M_{23}C_6$ than M_6C because of a slightly larger

lattice misfit of the M_6C to the host matrix that often results in a loss of coherence of interphase boundaries (IPBs).

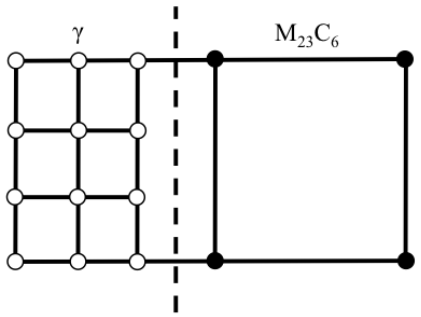

Fig. 4.3. Cube-on-cube structure of the γ matrix and the $M_{23}C_6$ carbide. The dashed line shows the partial coherent interphase boundaries.

4.1.2. MECHANICAL PROPERTIES

The microstructural development during thermal aging inevitably changes a material's mechanical properties. A typical example is the time-dependence of material strength. Material strength increases with time during the early aging stage and then decreases with further aging. The changes in material strength involve different dislocation-particle interaction mechanisms related to the nature of particles (e.g. type, coherency, dimension, density, etc.) in alloys.

Fig. 4.4 shows two typical strengthening mechanisms based on dislocation-particle interaction. The first strengthening mechanism is dislocation cutting. (Fig. 4.4(a)) Some small and highly coherent particles (e.g. GP-I, GP-II and θ' in aged Al-Li alloys) are found to be deformable: dislocations are able to cut though them when sufficient stress is applied. The equation governing this strengthening contribution was found to be:

$$\tau = CG\varepsilon^{3/2}(fr/b)^{1/2}, \qquad (4-2)$$

Where, τ = stress required for dislocation passing the particle

ε = misfit strain (proportional to difference in lattice parameter of the two phases)

r = particle radius

f = volume fraction of precipitated second phase

G = shear modulus

b = Burgers vector

As discussed in the last section, the volume fraction of second phase particles increases during the early stage of thermal aging until an equilibrium volume fraction is achieved. The large second-phase particles continue to coarsen at the expense of smaller particles during further aging. With particle growth, the spacing between particles and the misfit strain in particle-matrix interface both increase. When the misfit strain is sufficiently large, the particle-matrix interface loses coherency, and dislocations are unable to cut through particles. Similarly, when the increased particle separation is higher than a critical value, dislocation cutting cannot occur. For both situations, a dislocation will bow/loop around particles and require a larger stress to further its movement. This dislocation-particle interaction is also referred as *Orowan looping*. (Fig. 4.4(b)) The required stress for a dislocation to pass particles is analogous to the stress given for the activation of Frank-Read sources:

$$\tau = \frac{Gb}{L-2r}, \qquad (4-3)$$

Where, L is distance between pinning points (particles).

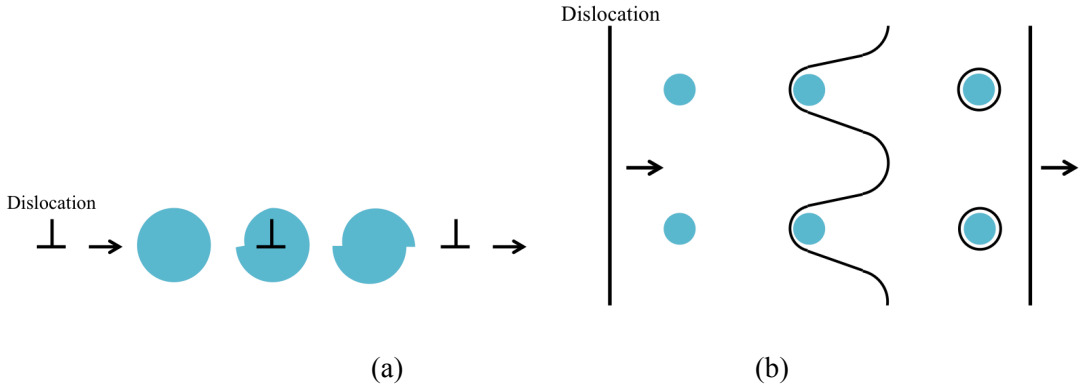

Fig. 4.4. Schematic representation of two strengthening mechanisms by dislocation-particle interaction: (a) particle cutting (b) *Orowan looping*

Beyond particle hardening, the aging process influences another important strengthening mechanism: solid solution strengthening. The solid solution elements can generate either asymmetrical or symmetrical stress fields that result in tetragonal and spherical distortion, respectively. The strengthening caused by the asymmetrical stress field is

rather significant. A typical example can be found in carbon atoms present in martensite. In contrast, the capacity of the symmetrical stress field to impede dislocation movement is limited. The increase in yield strength can be estimated by:

$$\tau = \frac{G\varepsilon^{3/2}c^{1/2}}{700}, \qquad (4-4)$$

where, ε = misfit strain (proportional to size difference between the solute and solvent atoms)

c = solute concentration (expressed as atomic fraction)

For nickel-based alloys, the solid solution elements often possess a symmetrical stress field [135].

Incorporating all introduced strengthening components, an overview of material strength evolution during thermal aging is schematically drawn in Fig. 4.5. The changes in overall strength are contributed to three components: dislocation cutting, dislocation looping and solid solution strengthening. At the onset of thermal aging, the alloy experiences the greatest potential for solid solution strengthening due to the maximum amount of supersaturated elements present in the host matrix. During the early aging stage, small and highly coherent particles precipitate within the matrix grains and their respective grain boundaries at the expense of supersaturated solute. This provides an additional strengthening component, dislocation cutting, to the alloy. Meanwhile, the strengthening component caused by solid solution decreases along with increasing precipitate strengthening. However, the loss of strengthening by the decrease of solute levels can be more than compensated by the precipitation hardening mechanisms. With further aging, the equilibrium condition is achieved, and the associated precipitation process is finished. As a result, the strengthening contributed by the solid solution mechanism decreases to a minimum value (point 'A' in Fig. 4.5). With particle growth, the dominant mechanism of dislocation-particle interaction gradually changes from cutting to bowing. This transition can be characterized by the critical particle radius, r_c, which is typically on the range of 5-30 nm. Therefore, before particles develop to the critical size ($r < r_c$), dislocation cutting is the dominant mechanism. With thermal aging and associated particle growth, the particle size will finally exceed the critical

value ($r > r_c$), and dislocation bowing then becomes the dominant mechanism. Point 'B' in Fig. 4.5 indicates the moment when the particle radius reached the critical radius ($r = r_c$). The peak strength of the alloy obtained during aging is the result of the overall response for all strengthening components. (point 'C' in Fig. 4.5) With regard to Fig. 4.5, the alloy before aging to the moment of 'C' is considered the 'underaged' condition. Conversely, the alloy is considered to be 'overaging' after progressing past the moment of 'C'.

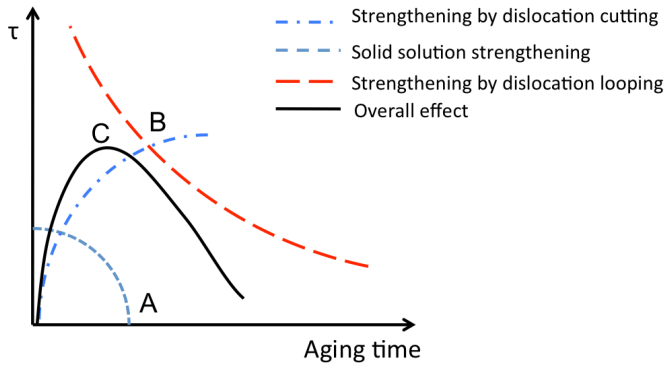

Fig. 4.5. Overall aging effect [114]

4.2 MICROSTRUCTURE DURING VARIOUS AGING CONDITIONS

4.2.1 MICROSTRUCTURE IN THE AS-RECEIVED CONDITION

The microstructure of Alloy 617 and Alloy 230 in the as-received condition has been introduced in the prior chapter. The typical microstructural characteristics consist of large strengthening particles within the grains and their respective grain boundaries. (Fig. 3.1) These intrinsic particles in Alloy 617 are Cr rich $M_{23}C_6$, Mo rich M_6C, and a small amount of Ti(C,N). [37] In Alloy 230, the intrinsic particles are W rich M_6C. [35] These particles in both alloys are strung as bands in the transverse planes and flattened in the rolling planes. The effect of orientation on mechanical properties caused by this microstructural gradient was discussed in section 3.3. These large carbide particles do not exhibit any apparent orientation relation or coherency with the host matrix grains from TEM examinations. (Fig. 4.6) However, the small intergranular particles (primarily $M_{23}C_6$ type) in the alloys have a cube-on-cube relation with the host matrix. (Fig. 4.7) The interphase boundaries between the particles and matrix are partly coherent in this cube-on-cube structure. (Fig. 4.3) Compared to

large particles, these small intergranular particles do not have a significant impact on the alloys' mechanical properties because of their small volume fraction and good coherency with the host matrix.

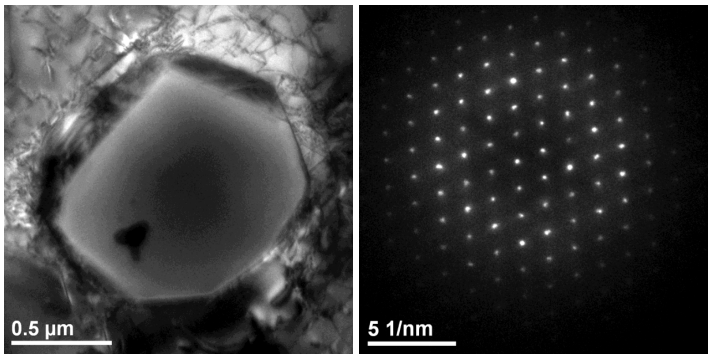

(a) (b)

Fig. 4.6. Large, incoherent $M_{23}C_6$ carbide in Alloy 617 (a) Bright field image (b) Diffraction pattern (zone axis [011])

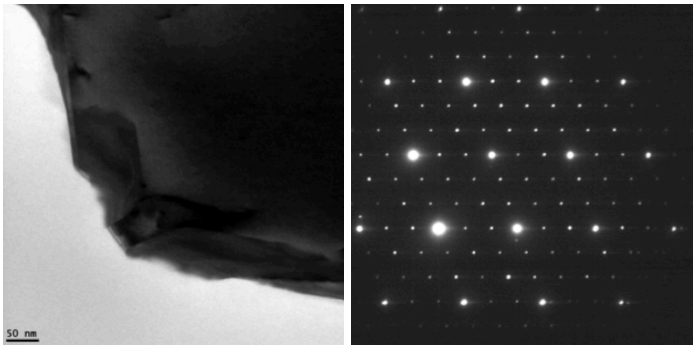

(a) (b)

Fig. 4.7. Intergranular $M_{23}C_6$ carbides in Alloy 617 (a) Bright field image (b) Diffraction pattern (zone axis [011])

The SEM and EBSD analyses show a duplex grain size distribution in Alloy 617: small grains with sizes ranging from 10 to 30 µm in the inclusion rich areas, and large grains with sizes ranging from 40 to 100 µm in the inclusion free areas where grains grow during annealing without Zener pining. (Fig. 3.1(a) & 3.5(a)) The gain size in Alloy 230 did not exhibit a great variety. The average grain size measured in Alloy 230 was ~70 µm. (Fig. 3.5(b)) Additionally, both alloys possess a high fraction of twin boundaries (∑3 grain boundaries), which are ~60% and ~53% of the total grain boundaries for Alloy 617 and Alloy 230, respectively.

4.2.2 MICROSTRUCTURE AFTER A SHORT-TERM AGING

Fig. 4.8 shows the microstructural characteristics of Alloy 617 aged at 900ºC for 30 hours. The dominant feature during short-term aging was found to be the fine and ordered precipitates nucleating on the {111} planes. (Fig. 4.8 (a)) These intragranular precipitates were the $M_{23}C_6$ type carbides with the cube-on-cube orientation relations with the γ matrix. (Fig. 4.9) Depending on the nucleation site, the size of the fine precipitates was on a range from ~10 nm (within the matrix grain, Fig. 4.8(a) & Fig. 4.9) to ~100 nm (near different boundaries, Fig. 4.8(b-d))

The characteristics of intergranular precipitates in Alloy 617 after short-term aging were found to differ from those of the as-received condition. First, the shape of intergranular particles was transformed from a film shape to an ellipsoid, along with a considerable thickness increase. (Fig. 4.8(b)) Second, the twin boundaries, which were free of particles in the as-received condition, were subjected to precipitation of long, needle-shaped particles. (Fig. 4.8(c)) Third, some intergranular particles lost their semi-coherency to the host matrix due to the size increase. Fig. 4.10 shows an intergranular carbide that developed a new orientation relation with the matrix: $[-114]_M$ // $[011]_P$. Alloy 230 experiences a similar process of microstructure development during short-term aging. Fig. 4.11 shows $M_{23}C_6$ carbides that precipitated within the matrix grains as well as the twin, grain and interphase boundaries.

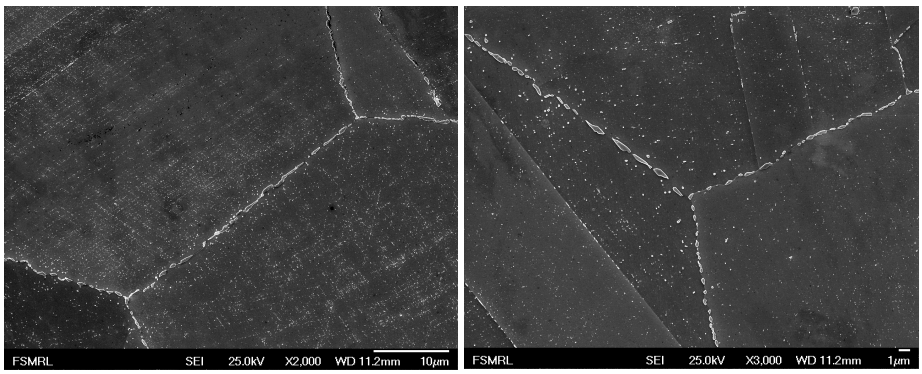

(a) (b)

Fig. 4.8. Microstructure characteristics of Alloy 617 aged at 900ºC for 30 hours: (a) fine ordered precipitates within matrix grains (b) particle nucleation and growth on grain boundaries (c) particle nucleation and growth on a twin boundary (d) particle growth on interphase boundaries

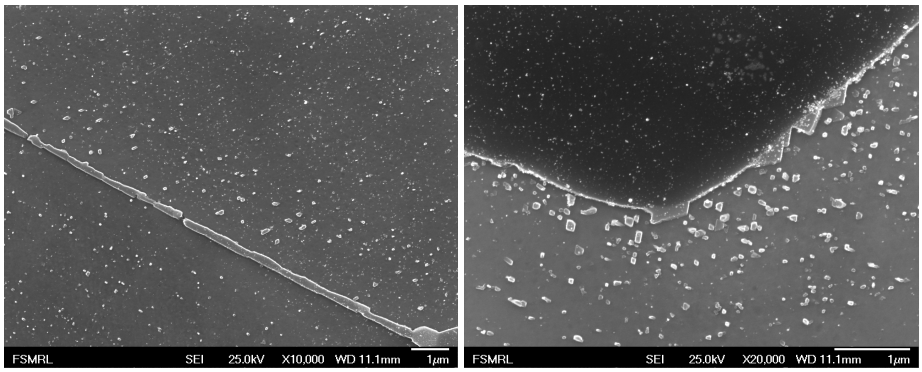

(c) (d)

Fig. 4.8. Cont.

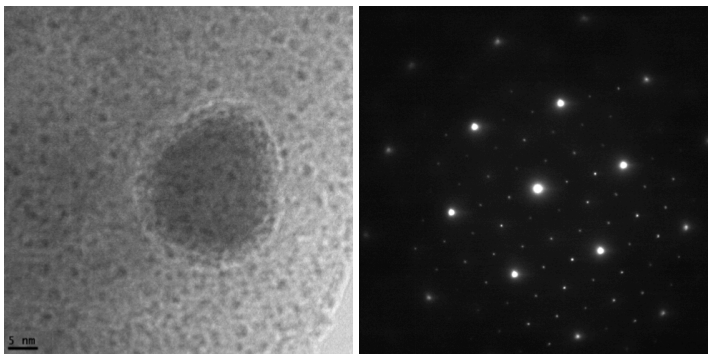

(a) (b)

Fig. 4.9. TEM analysis of small precipitate of Alloy 617 aged at 900ºC for 30 hours (zone axis [111])

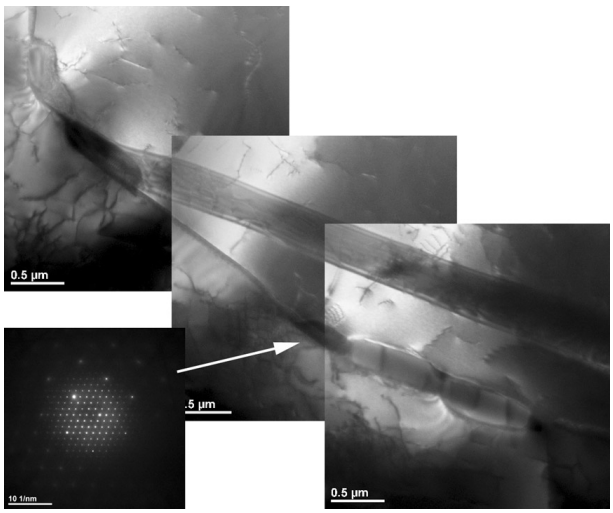

Fig. 4.10. TEM analysis of Alloy 617 aged at 1000°C for 300 hours: an intergranular precipitate (P) with an orientation relation with the matrix (M): $[-114]_M$ // $[011]_P$

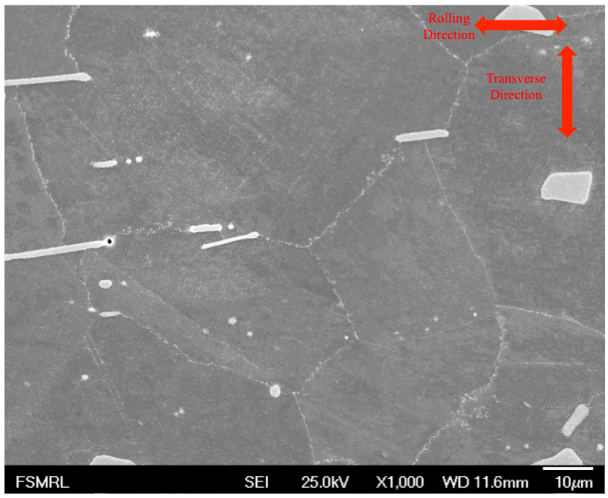

Fig. 4.11. Microstructure characteristics of Alloy 230 aged at 900ºC for 30 hours

4.2.3 MICROSTRUCTURE AFTER A LONG-TERM AGING

After long-term (>1000 hours) aging, most of the fine precipitates that nucleated within matrix grains diffuse and grown within grain boundaries and interphase boundaries. (Fig. 4.12 and Fig. 4.13) In contrast to the high particle density in these boundaries, few precipitates were found on twin boundaries. The intergranular particles experienced significant coarsening during long-term aging. In both alloys, most particles increased to a size exceeding 1 μm^2 after aging at 1000ºC for 3000 hours. Despite considerable coarsening, most large intergranular precipitates in each alloy were found to still maintain semi-coherency (cube-on-cube orientation relation) with the γ matrix from TEM analysis. (Fig. 4.14 and Fig. 4.15)

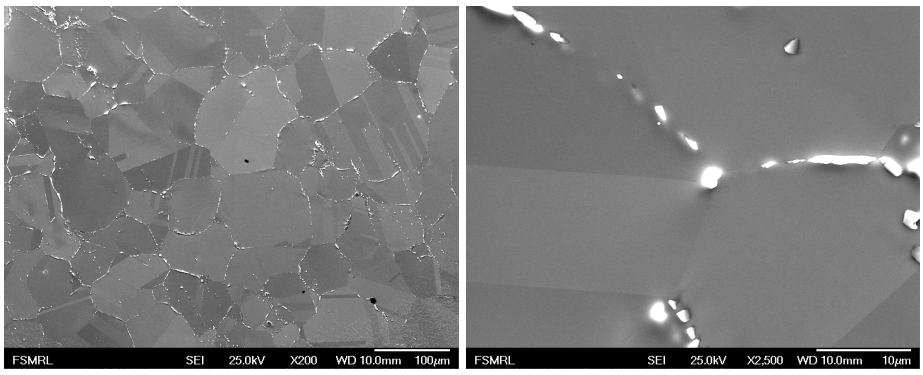

(a) (b)

Fig. 4.12. Microstructure of Alloy 617 aged at 1000ºC for 3000 hours: (a) overview; (b) intergranular precipitates

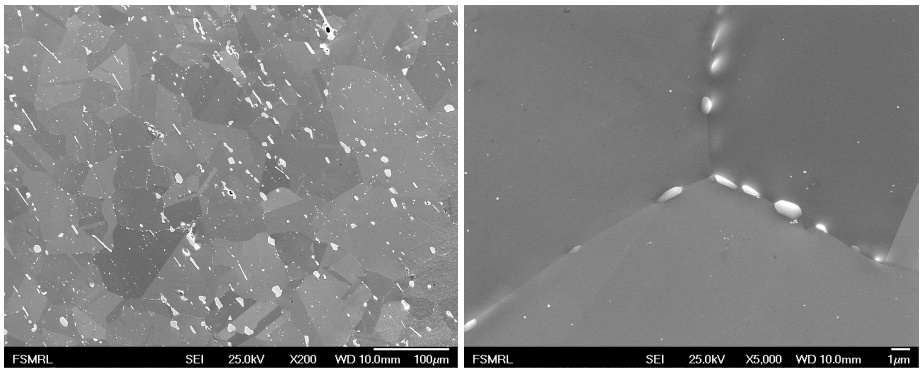

(a) (b)

Fig. 4.13. Microstructure of Alloy 230 aged at 1000ºC for 1000 hours: (a) overview; (b) intergranular precipitates

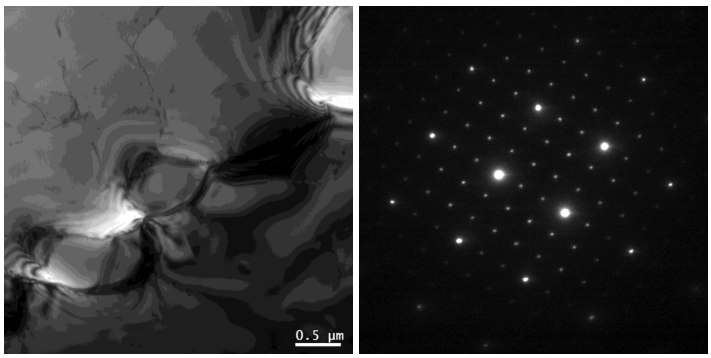

Fig. 4.14. TEM analysis of Alloy 617 aged at 1000ºC for 1000 hours (zone axis [001])

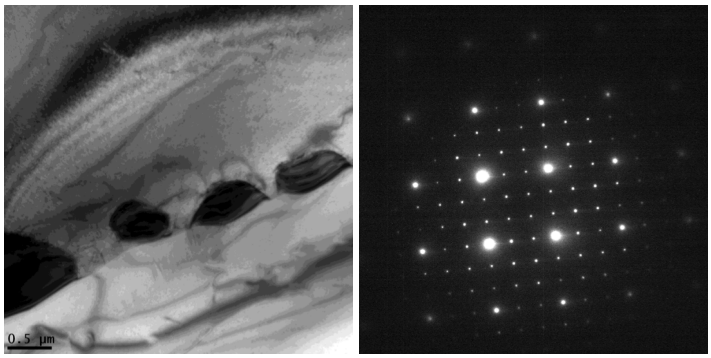

Fig. 4.15. TEM analysis of Alloy 230 aged at 1000ºC for 1000 hours (zone axis [001])

During thermal aging of Alloy 617, no significant changes in grain boundary character distribution (GBCD) and grain size distribution were found in either alloy. Fig. 4.16 shows the EBSD analysis for Alloy 617 aged at 900ºC for 1000 hours. The high fraction of twin boundaries and the duplex grain size distribution were preserved after long-term aging.

Similar results were observed in Alloy 230, showing a remarkable thermal stability for both alloys. In addition, no topologically close-packed phase (TCP) (e.g. sigma(σ), mu(μ) or chi(χ)) was observed during the aging experiment.

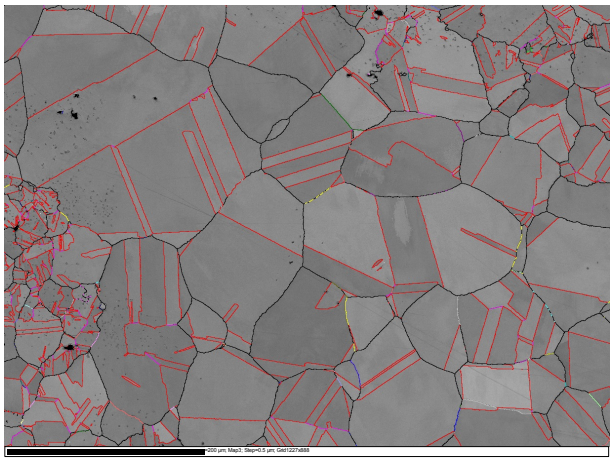

Fig. 4.16. EBSD and CSL boundary analysis for Alloy 617 aged at 900ºC for 1000 hours

4.2.4 Particle growth

In order to study the kinetics of carbide growth, the process of particle coarsening in grain boundaries was analyzed by measuring the particle volume increase. More than 150 intergranular particles were measured from SEM images from each aging condition. Fig. 4.17 shows an example for measuring the length and width of intergranular particles. The results of the measurements are shown in Fig. 4.18. For both alloys, the intergranular particles became much larger during aging at 1000ºC compared to 900ºC. This indicates a strong temperature dependence for intergranular particle coarsening. Additionally, a different coarsening rate of intergranular particles in Alloy 617 and Alloy 230 was observed. In nearly every aging condition and despite comparable initial dimensions, the length and width of Alloy 617 particles were found to be twice that of Alloy 230 particles, showing a much higher coarsening rate in Alloy 617.

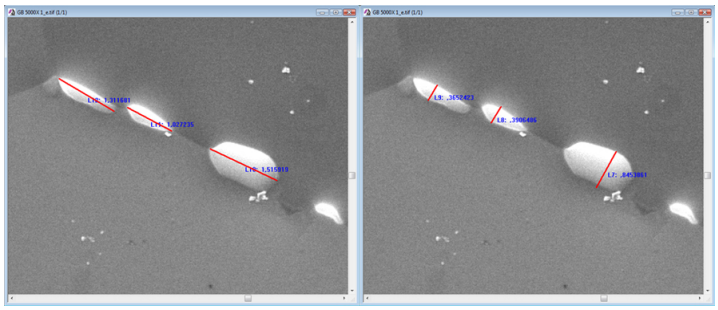

Fig. 4.17. Example of the dimension measurement of intergranular precipitates: (a) length; (b) width

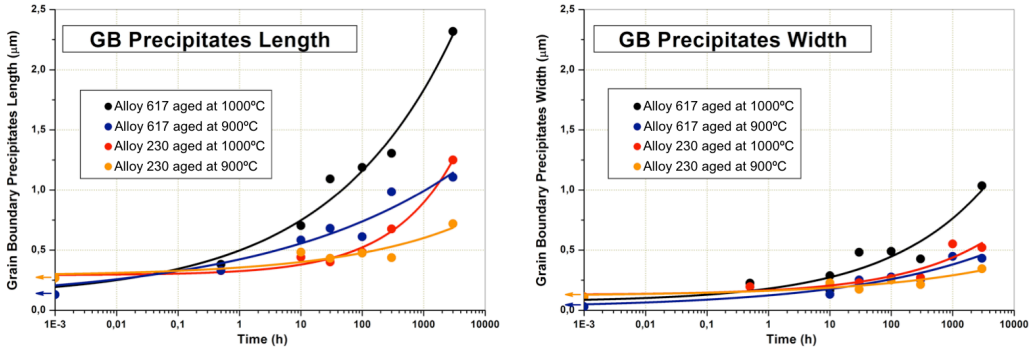

(a) (b)

Fig. 4.18. Dimensions of intergranular precipitates in Alloy 617 and Alloy 230: (a) Length (b) Width

Based on the measurements of the width and length of the particles, 3D analysis for the volume increase is conducted. The basic assumption is that the particle shape is ellipsoidal during long-term aging, which is reasonable from SEM observations. Thus, the particle volume can be calculated by:

$$V(t) = \frac{4}{3} r^2 h \quad (4-5)$$

where V is the volume of second-phase particles as a function of time, r and h are the radius and height of ellipsoid particles, corresponding to the measured length (Fig. 4.18(a)) and width (Fig. 4.18(b)), respectively. Thus, the volume development for the particles can be fitted using an adapted Avrami equation:

$$Y = 1 - \exp(-Kt^n) \quad (4-6)$$

where Y is the particle volume fraction in a function of time and is defined by:

$$Y = \frac{V(t)}{V_{mat}} \qquad (4-7)$$

V_{mat} is the volume of matured second-phase particles, and K and n are the fitting constants. Because the intergranular particles are considered to be fully developed after aging for 3000 hours [37], and little volume will be obtained by an extended aging time, V(3000h) can be assumed to be equal to V_{mat}. Fig. 4.19 shows a fit curve for intergranular particle volume development in Alloy 617 aged at 900ºC.

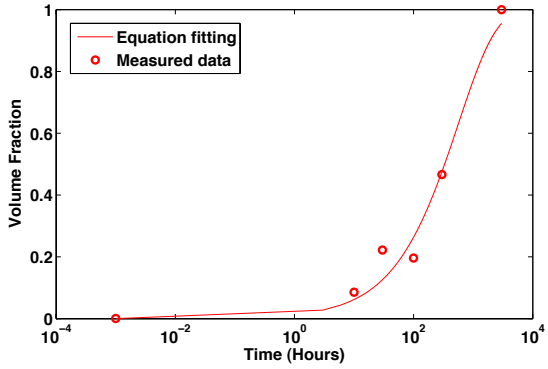

Fig. 4.19. Fitting curve for intergranular particle volume development in Alloy 617 aged at 900ºC

The process of particle volume development can be seen in the 3D analysis shown in Fig. 4.20. The particle volume rapidly increases during the early stage of aging (t < 300 hours), and then decelerated coarsening follows after extended aging time (t >300 hours). The tendency of particle growth and its temperature dependence can be quantitatively studied though analysis of particle-coarsening rate (i.e. dY/dt). (Fig. 4.21) For each alloy, intergranular particles obtained a large coarsening rate during the early stage of aging. Nevertheless, the changes in dY/dt over time are controlled by different kinetics for 900 and 1000ºC. For the situation at 900ºC, despite a high coarsening rate at the beginning of aging, the value decreases dramatically with aging time. This suggests a decline in driving force over aging time. In contrast, the particle coarsening rate during aging at 1000ºC increased for ~400 hours and then decreased moderately during further aging. The highest coarsening rate was found to be ~7×10^{-4}/h.

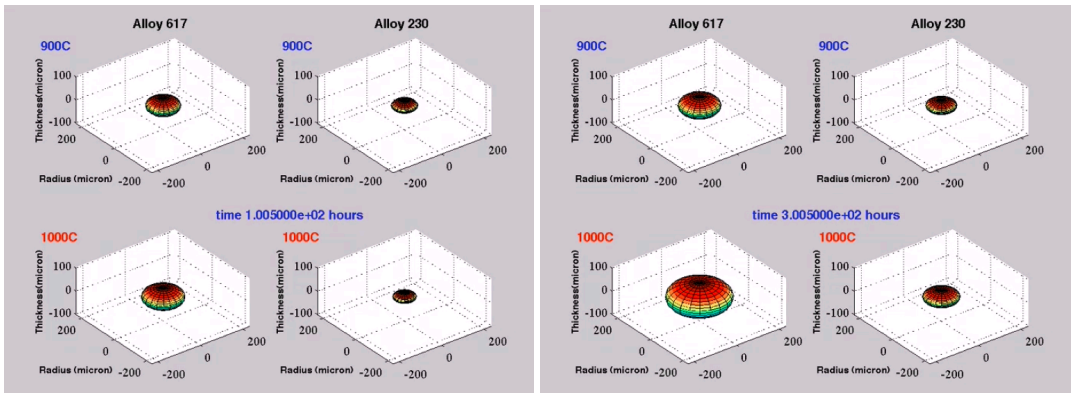

(a) (b)

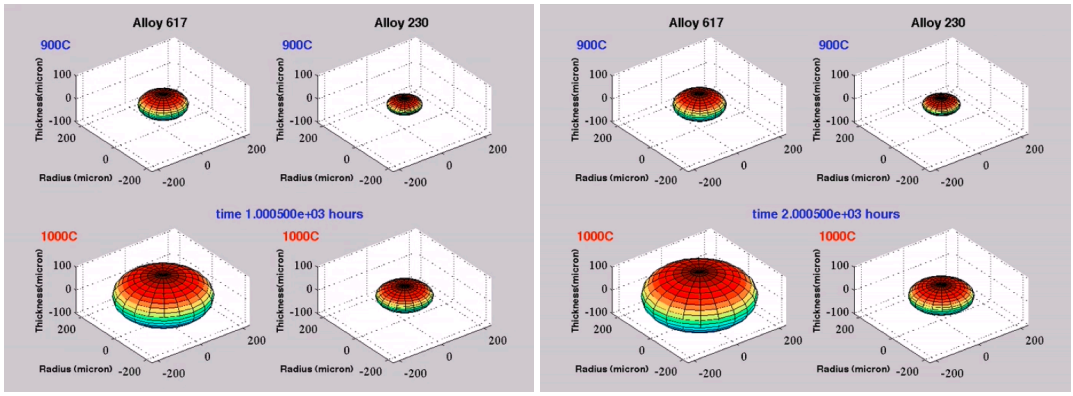

(c) (d)

Fig. 4.20. 3D images showing intergranular particle volume development after: (a) 100 hours (b) 300 hours (c) 1000 hours (d) 2000 hours

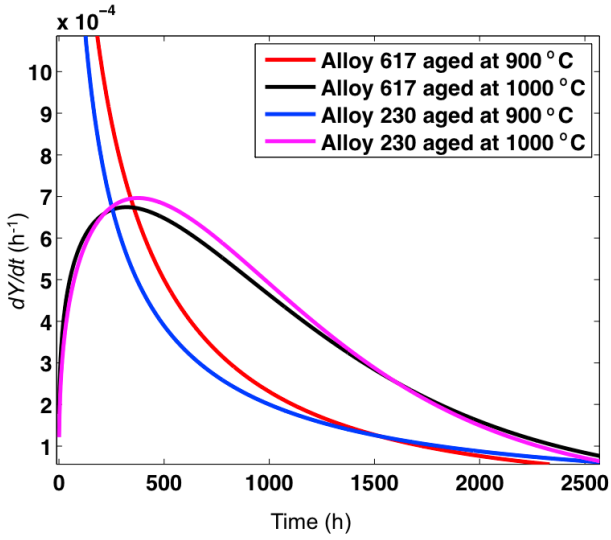

Fig. 4.21. Particle coarsening rate for Alloy 617 and Alloy 230 aged at 900 and 1000ºC

4.3 MECHANICAL PROPERTIES

Hardness and tensile tests were performed on Alloy 617 and Alloy 230 in conditions ranging from as-received to after 3000 hours aging. The tensile tests were conducted at a strain rate of ~10^{-3}/s using an INSTRON 1331 servohydraulic test system equipped with a high-temperature furnace. The detailed procedures for tensile testing have been given in section 3.2. The hardness of both alloys was measured using a Wilson® Rockwell® Model 523 hardness tester.

In order to measure the overall response from the rolling and transverse planes, the hardness tests were conducted in all planes directions. The hardness for each aging condition is obtained by averaging the measurement results. Fig. 4.22 shows the measured hardness of Alloy 617 and Alloy 230. Both alloys experienced a similar hardness development during aging: the peak hardness for both alloys is achieved during early stage aging (< ~10 hours) and followed by a continuous softening upon extended aging time. A typical hardening process can be seen in the Alloy 617 sample aged at 900ºC: the material's hardness increased from ~90 to ~94 HRB in 10 hours and then gradually decreased over time. The hardening for Alloy 617 at 1000ºC is moderate with a slight hardness increase from ~90 to 91 HRB. For each temperature, the hardness of Alloy 617 decreases to a similar value of ~88 HRB after aging for 3000 hours. This value is lower than the hardness in the as-received condition. Compared to Alloy 617, Alloy 230 experiences a longer hardening effect during aging, especially for the sample aged at 900ºC. Furthermore, the hardness decline in Alloy 230 is less than that of Alloy 617 aged at the same conditions.

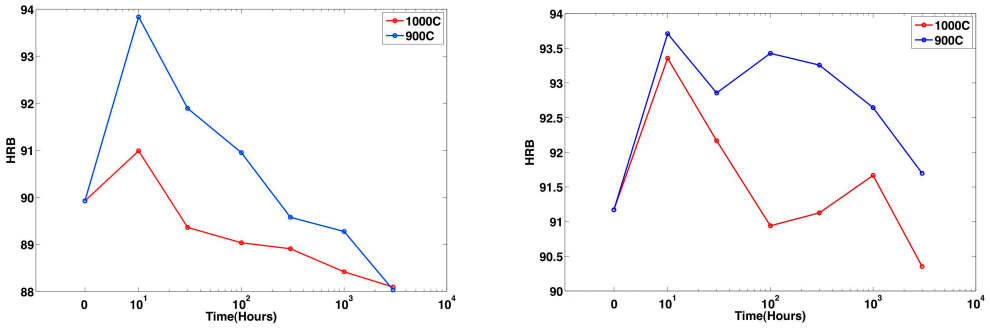

Fig. 4.22. Hardness of the as-received and aged: (a) Alloy 617 (b) Alloy 230

The results of tensile tests for the as-received and aged alloys are shown in Fig. 4.23 & 4.24. Agreeing with the hardness measurements, the measured tensile properties show a typical aging process characterized by a short-term strengthening and a long-term softening. The only exception lies in the Alloy 617 sample aged at 1000 ºC, where no apparent strengthening is observed. (Fig. 4.23) For both alloys, the changes in tensile properties during aging are controlled by the studied temperature. Generally, both alloys aged at 900ºC attain higher yield and tensile strengths with a longer hardening time compared to samples aged at 1000ºC. This suggests a more intense diffusion process at higher temperatures, so precipitate hardening can only maintain for a short time.

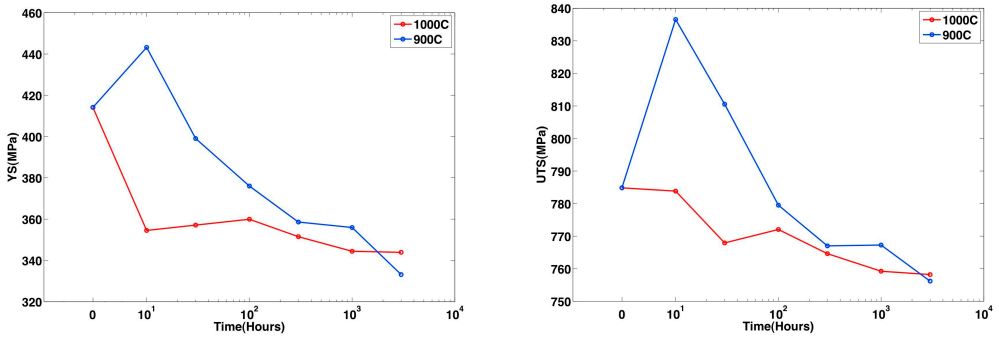

Fig. 4.23. Tensile properties for the as-received and aged Alloy 617: (a) Y.S. (b) U.T.S.

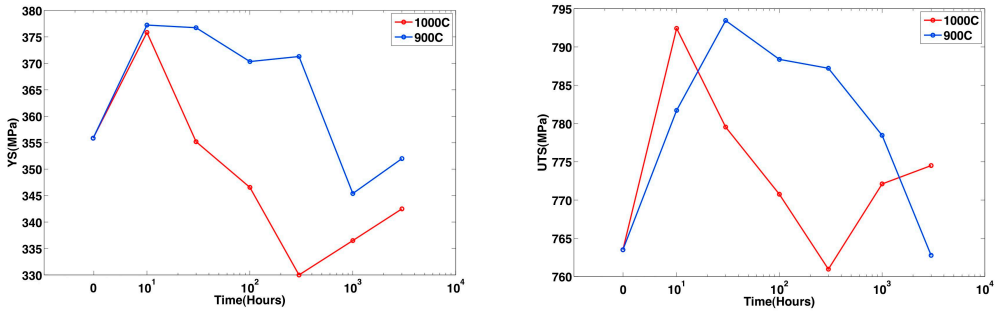

Fig. 4.24. Tensile properties for the as-received and aged Alloy 230: (a) Y.S. (b) U.T.S.

Beyond studying mechanical properties at room temperature, it is also important to investigate the aging effect on tensile responses at high temperatures, particularly for the 800-1000ºC temperature range at which the VHTR will operate. Fig. 4.25 shows a comparison of tensile properties for the as-received and 3000 hours aged (at 1000ºC) Alloy 617. Both yield

and tensile strengths for various temperatures are found to decrease after aging for 3000 hours. This softening effect can be quantified by calculating the relative strength reduction by:

$$\text{Y.S. reduction} = \frac{\text{Y.S.}(T, t=0) - \text{Y.S.}(T, t=3000h)}{\text{Y.S.}(T, t=0)} \qquad (4-8)$$

$$\text{U.T.S. reduction} = \frac{\text{U.T.S.}(T, t=0) - \text{U.T.S.}(T, t=3000h)}{\text{U.T.S.}(T, t=0)} \qquad (4-9)$$

,

where T is the studied temperature (RT to 1000ºC) during tensile testing. The results of strength reduction are summarized in Table 4.1. The softening effect after long-term aging is much more significant for the Y.S. compared to the U.T.S. The reduction in Y.S. at all studied temperatures (except 700ºC) is higher than 15% with an average value over 20%. In contrast, the mean reduction in U.T.S. is only ~5%. It can be noted that the loss in U.T.S. is temperature sensitive: high strength loss occurs at temperatures higher than 800ºC, while the strength loss is very small at lower temperatures (RT to 700ºC).

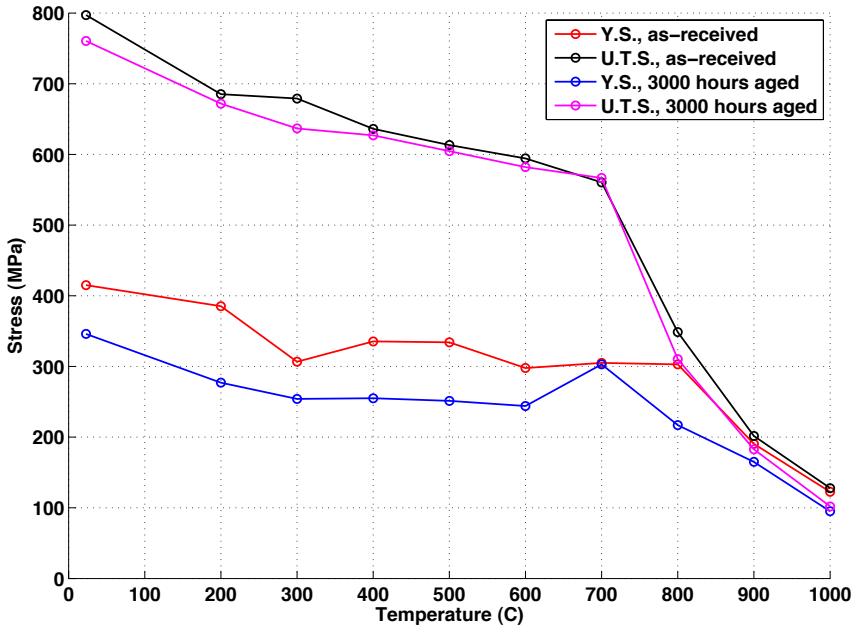

Fig. 4.25. Tensile properties at various temperatures of the as-received and long-term aged (at 1000ºC) Alloy 617

Table 4.1. Aging effect on tensile properties of Alloy 617 for various temperatures. The samples were aged for 3000 hours at 1000ºC.

Temperature (ºC)	RT	200	300	400	500	600	700	800	900	1000
Y.S. in AR condition (MPa)	415	385	306	335	334	297	305	303	190	122
U.T.S. in AR condition (MPa)	797	685	679	636	613	594	560	348	201	127
Y.S. after aging (MPa)	346	277	254	255	251	244	303	217	165	95
Reduction (%)	16.7	28.0	17.0	23.9	24.8	17.8	0.7	28.4	13.2	22.1
U.T.S. after aging (MPa)	760	672	637	627	605	582	567	310	183	102
Reduction (%)	4.6	1.9	6.2	1.4	1.3	2.0	-1.0	10	8.9	19.7

4.4 DISCUSSION

4.4.1 MICROSTRUCTURAL DEVELOPMENT

The aging process for both Alloy 617 and Alloy 230 is characterized by particle nucleation and growth. According to the microstructural development, the aging process can be essentially divided into two stages: the early stage, featuring fine and ordered precipitates within matrix grains and boundaries (Fig. 4.8(a)) and the overaging stage, with depletion of small precipitates within the grains (Fig. 4.12 & 4.13) along with a significant coarsening of intergranular particles. During aging, the favorable nucleation sites for precipitates, determined by a higher free energy (or larger average atomic volume) compared to the host matrix, are interphase boundaries, grain boundaries and twin boundaries. Thus, the size of the particles in these areas is much larger than particle size within the host matrix. After an extended aging time, the precipitates diffused and stabilized in the areas with the highest interfacial free energy (e.g. interphase boundaries and high-angle grain boundaries). Both matrix and twin boundaries were found to be free of carbide particles due to their low interfacial free energy. The depletion of carbide particles in twin boundaries is analogous to the anti-sensitization of low $\sum$ boundaries in steel: the low $\sum$ boundaries show a higher intergranular resistance for Cr depletion than high-angle grain boundaries. [143] The results

were also in good agreement with the findings by Schlegel et al. that low ∑ boundaries tended to suppress intergranular precipitation in Alloy 617 during creep. [34]

Whittenberger performed an aging test on both Alloy 617 and Alloy 230 at 820ºC over 20,000 hours. [55] No change in grain size was observed in his experiment. Tan et al. annealed Alloy 617 at 850 and 1000°C for 4 and 6 weeks after thermomechanical processing. [122, 126] He found that GBCD in Alloy 617 were persevered after thermal aging. In the current study, it was also found that 3000 hours aging at 900 and 1000ºC did not influence grain size distribution or GBCD for both Alloy 617 and Alloy 230. Their exceptional thermal stability is partially attributed to 'Zener pining' by large intrinsic carbides and age-coarsened intergranular particles. These particles inhibit the grain boundary migration and impede grain growth during aging. Hence, the grain boundary characters are preserved.

The maintenance for inexistence of topologically close-packed phases (e.g. sigma(σ), mu(μ) or chi(χ)) is critical to ensure material strength during service life, because these detrimental phases can cause a brittle failure at low temperatures and a loss of strength at high temperatures. [142] According to ThermoCalc® modeling, the σ phase can precipitate in Alloy 617 if the alloying composition is not well controlled. [10] Nevertheless, no TCP was observed in either alloy at any aging condition. This finding also agrees well with previous aging studies for Alloy 617 at lower temperatures by Wu et al. [40] and for similar a temperature range by Mankins et al. [37], Kihara et al. [39] and Kirchhofer et al. [38]

The analysis of intergranular particle growth provides insight into the kinetics of precipitation processes in Alloy 617 and Alloy 230. Particle nucleation and growth are essentially controlled by two factors, both of which are temperature dependent. The first factor is the driving force of particle nucleation that depends on the content of the second-phase in the equilibrium condition. The second factor lies in the diffusion kinetics of heterogeneous elements (e.g. C, W or Mo) that form the particles. The diffusion kinetics is directly related to aging temperature such that a higher temperature promotes the diffusion of heterogeneous atoms, and vice versa. According to the predicted equilibrium phase diagram of Alloy 617 [9], the content of particles (including both M_6C and $M_{23}C_6$) is slightly higher at

1000^{o} C compared to 900ºC. This suggests a larger driving force at 1000ºC for particle nucleation in Alloy 617. Moreover, the heterogeneous elements in both alloys obtained a higher diffusibility at 1000ºC. The slower diffusion process and the lower diving force significantly limit the particle growth in the alloys aged at 900ºC. The temperature dependence of particle growth can be seen in the 2D (Fig. 4.18) and 3D (Fig. 4.20) analyses that show larger intergranular particles grown at 1000ºC compared to 900ºC during aging.

Intergranular particle growth is also studied through analysis of the particle-coarsening rate (*dY/dt*). (Fig. 4.21) At 900ºC, most volume gain (in fraction) of intergranular particles occurs during the early stage of aging with a sharp decline in coarsening rate. This suggests a dramatic loss of growing momentum. In contrast, the particle coarsening rate increases in the first few hundred hours during aging at 1000ºC before the decline occurs. During this period of time, the carbide nucleation continues, accompanied by the growth of existing precipitates, until the equilibrium volume fraction is developed. It should be noted that this stage, characterized by a combination of particle nucleation and growth, also occurred for the alloys aging at 900ºC, but within a very short time (<<10 hours) due to a low equilibrium volume fraction of second-phase particles. Therefore, this transient at 900ºC was not observed in the present study.

Intergranular particle growth is analyzed based on the measured data fitted by the adapted Avarmi equation (eq. 4-6). The original form of the Avrami equation is:

$$X = 1 - \exp(-Kt^{n}), \qquad (4-10)$$

where X is the overall transformed volume fraction of second-phase particles. K and n are the physical interpretation of Avrami constants that are known as the Avrami coefficient and Avrami exponent, respectively. If we assume that the number of intergranular particles does not change with time (i.e. no impingement takes place during aging) X and Y can be considered with the equal value. Then, we can refer to the value of n that relates the balance between nucleation and growth and suggests the mechanism of transformation.

Table 4.2. Results and interpretation of *n*

	Alloy 617	**Alloy 230**	**Mechanism [144]**
900ºC	0.682	0.547	Thickening of large plates (n≈0.5)
1000ºC	1.27	1.34	Growth of particles of large volume (n =1-1.5)

Table 4.2 shows the possible mechanisms of the particle evolution of Alloy 617 and Alloy 230 during aging at 900ºC and 1000ºC. The "thickening of large plates" at 900ºC indicates a dominant coarsening process, whereas the "growth of particles of a large volume" suggests a mixed process involving both nucleation and growth. [144] The interpretations of *n* agree well with the previous discussion.

Different heterogeneous elements can attribute to different kinetics for particle growth in Alloy 617 and Alloy 230. W, as a main alloying element in Alloy 230, is less thermally active compared to Co and Mo in Alloy 617. The lower thermal activity of W can be reflected in its much higher melting temperature (T_m of W: 3422ºC >> T_m of Mo: 2623ºC & T_m of Co: 1495ºC). The diffusion rate of W in γ matrix is therefore lower compared to Co and Mo and results in a relatively slower process of precipitate growth in Alloy 230. (Fig. 4.18 & 4.20) Additionally, the varying diffusion kinetics in the alloys can be reflected by the changes in mechanical properties with aging and will be discussed in the following section.

4.4.2 MECHANCIAL PROPERTIES

As introduced in section 4.1, the strength development with aging typically involves three strengthening mechanisms: dislocation cutting (τ_{cut}), dislocation looping (τ_{loop}) and solid solution strengthening (τ_{sss}). (Fig. 4.5) Material's fundamental strengthening mechanisms also include strain hardening (τ_{sh}) and gain-boundary hardening (τ_{HP}, the subscript 'HP' denotes the Hall-Petch relationship). Therefore, a comprehensive relation to describe the overall strength (τ_{tot}) of the alloys can be given as:

$$\tau_{tot} = \tau_0 + \tau_{HP} + \tau_{sh} + \tau_{sss} + \tau_{loop} + \tau_{cut}, \qquad (4-11)$$

where τ_0 is intrinsic strength of the material without additional strengthening mechanisms. The value of τ_{sh} is close to the frictional stress for the dislocation movement, also known as the Peierls stress that can be expressed in terms of the width, w, of a dislocation:

$$\tau_0 = G\exp(\frac{-2\pi w}{b}) \qquad (4-12)$$

Note that the $M_{23}C_6$ carbides are the main precipitates during the early stage of aging. These particles are non-deformable and partially coherent to the γ matrix during aging. Fig. 4.26 shows an SEM image for an Alloy 230 specimen that has been plastic deformed and processed by fine polishing and acid etching. The dislocation looping/bowing around the particles induces a strained area that can be easily etched out. The fine particles within etched pits suggest that the dislocation bowing/looping is the strengthening mechanism for aged alloys. (Fig. 4.26) Therefore, the component τ_{cut} can be discarded from equation 4-11 because dislocation cutting does not occur.

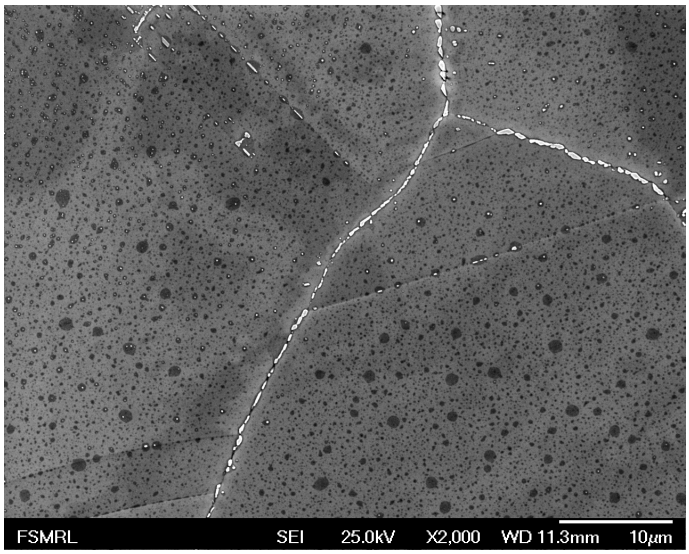

Fig. 4.26. Alloy 230 aged at 1000ºC for 10 hours

According to microstructural analysis, the grain size does not change with aging so that the strength component of grain-boundary hardening, τ_{HP}, can be considered to be constant during aging. If we assume that the dislocation density does not change significantly

with aging, then the strain hardening component, τ_{sh}, can also be treated as aging-independent. Accordingly, the equation 4-11 can be simplified to:

$$\tau_{tot} = \tau_{sss} + \tau_{loop} + \tau_{other} \qquad (4-13)$$

τ_{other} is composed of all strengthening components that are invariable with aging. Thus, the overall strength development with aging can be analyzed based on the balance of τ_{loop} and τ_{sss}. In fact, the particle strengthening is much more efficient and stronger compared to the solid solution strengthening and controls the overall hardening response during aging. Accordingly, the changes in mechanical properties observed in both alloys with aging can be interpreted. For Alloy 617 aged at 900ºC, nucleation of fine particles results in precipitate strengthening (increasing τ_{loop}) and a loss of solid solution strengthening (decreasing τ_{sss}) in a very short time. The precipitate strengthening is sufficiently large to compensate the loss of solid solution strengthening. As intergranular particles grow at the expense of fine precipitates, spatial distance between particles (L in equation 4-3) continues to increase. Therefore, τ_{loop} is gradually decreasing and becomes less effective for the overall strength (τ_{tot}). When the particles finally stabilized in the boundaries, τ_{tot} becomes lower than the value before aging due to the loss of solid solution strengthening. The results of hardness and tensile tests show this aging process characterized by short-term hardening and long-term softening. (Fig. 4.22(a) & 4.23) However, this sectional process is not observed in alloys aged at 1000ºC. Due to a much higher diffusion rate, the particles grow rapidly at 1000ºC compared to 900ºC. This leads to a sharp decline of strength within a short time (<<10 hours) because of the loss of fine particles as hardeners. Particle strengthening is not enough to compensate for the loss of strengthening by solute elements. Hence, the softening effect is dominant for Alloy 617 aging at 1000ºC. Fig. 4.27 shows the schematic of the overall aging effect of Alloy 617 at 900 and 1000ºC.

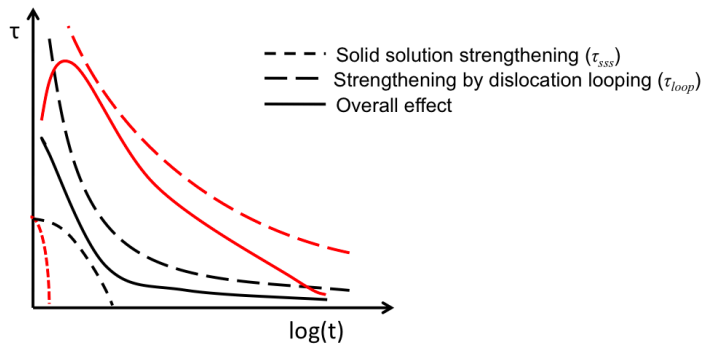

Fig. 4.27. Schematic of the overall aging effect of Alloy 617 at 900 (red) and 1000ºC (black)

For Alloy 230, the changes in mechanical properties with aging experience a similar trend in development as Alloy 617. However, as discussed in section 4.3.1, the main heterogeneous element, W, in Alloy 230 has a lower diffusibility compared to Mo and Co in Alloy 617. Thus, the precipitate growth in Alloy 230 is slower and results in a moderate decline of particle strengthening. This explains the observation of a longer hardening effect for Alloy 230 compared to Alloy 617. (Fig. 4.22 - 4.24)

After long-term aging, a loss of strength is not only found in tensile testing at room temperature, but also at high temperatures up to 1000ºC. These strength reductions with thermal aging are analogous to the results of the orientation effect analysis (section 3.3). Both studies suggest that the degradation of tensile properties at high temperatures is comparable to that at low temperatures.

Finally, the measured hardness of Alloy 617 after 300 and 1000 hours of aging is higher than the values reported in ref. 23. The aging effect on microstructure evolution and associated mechanical properties is dependent on chemical composition and the history of heat treatment. From the data summarized in ref. 9, the kinetics and magnitude of changes in hardness and tensile properties with aging are different from one heat to another. Therefore, proper control of chemical compositions and a regulation of heat treatment are both necessary to maintain the design margins of Alloy 617 and Alloy 230.

CHAPTER 5

SYNCHROTRON RADIATION STUDY

In this chapter, a state-of-the-art technique known as high-energy synchrotron X-ray radiation has been applied to study the deformation process of Alloy 230. The high resolution of synchrotron based X-ray diffraction provides a unique measurement for small volume fractions of carbides of the studied material (e.g. ~6% of M_6C in Alloy 230) which are difficult to observe using lab-based X-ray machines or neutron scattering facilities. The roles and limitations of the M_6C carbides during deformations were therefore clarified.

In addition, a high-energy diffraction technique was developed based on the combination of synchrotron X-rays and pressurized creep tubes This technique allows macroscopic creep strain and the microstructural development to be measured simultaneously by a single X-ray exposure. *In-situ* observation of the development of dislocation densities and lattice strain make it possible to track the onset of accelerated creep voids nucleation, growth and coalescence.

5.1 OVERVIEW

5.1.1 X-RAY DIFFRACTION MEASURMENT FOR TENSILE RESPONSE

High-energy X-ray diffraction measurements were carried out at the 1-ID beamline of the Advanced Photon Source (APS) in Argonne National Laboratory (ANL). The experimental setup and its schematic are shown in Fig. 5.1 and 5.2, respectively. Uniaxial tensile tests were performed on an MTS closed-loop servo-hydraulic test frame (Model 858) at a crosshead speed of 0.005 mm/s, corresponding to an initial specimen strain rate of $\sim 10^{-3}$/s. Diffraction measurements were conducted continuously with a monochromatic 86 keV (λ = 0.0144 nm) X-ray beam every 10 seconds. The incident beamsize was 300 x 300 μm^2. Complete Debye–Scherrer diffraction rings from the solid-solution austenitic matrix and the carbide from the diffraction volume were recorded using an area detector (GE angio type). An

ion chamber and a PIN diode (p-type, intrinsic, n-type diode) embedded within the beamstop were used to measure the initial and transmitted beam intensities, respectively. The distance between the sample and the detector was 1.336 m.

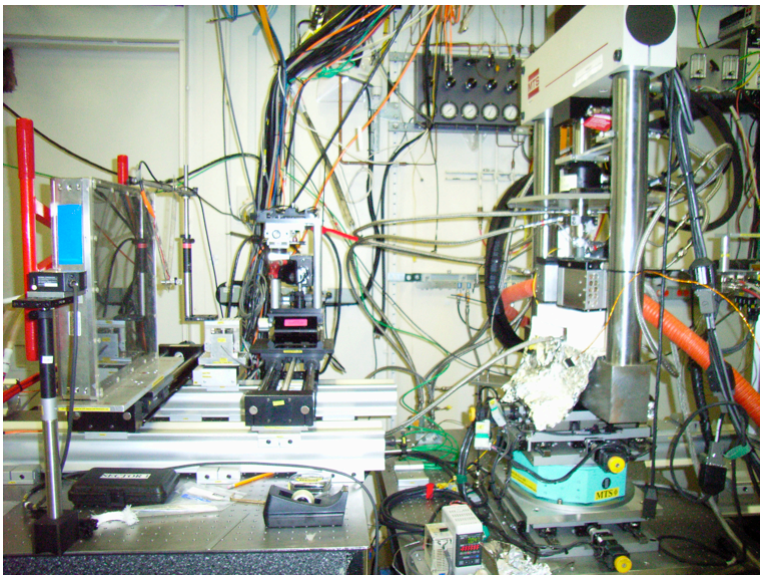

Fig. 5.1. The experimental diffraction setup at APS 1-ID beamline at ANL

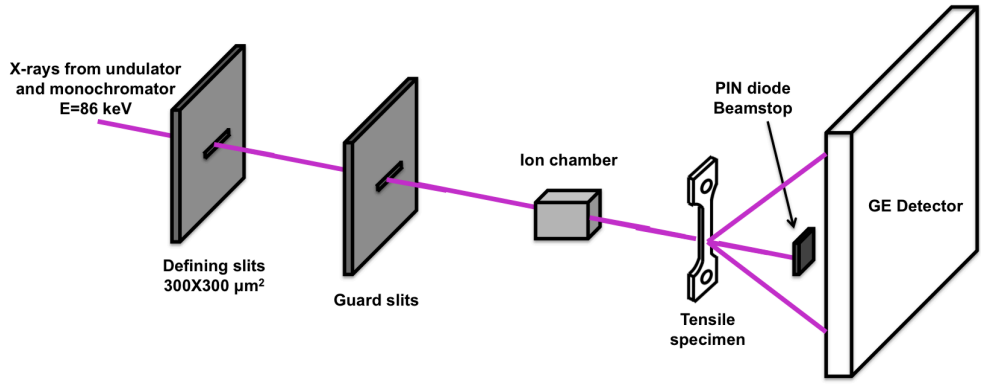

Fig. 5.2. Schematic of the experimental diffraction setup

Fig. 5.3(a)&(b) show typical 2D diffraction patterns from an Alloy 230 specimen before and after tensile loading (~45% strain), respectively. The Debye rings associated with various radii are reflected by lattice planes with various interplanar spacing, d_{hkl}. Before tensile loading, the diffraction pattern was incomplete rings (relatively sporadic with varying intensity for diffracted areas). (Fig. 5.3(a)) After tensile loading with a large strain, the alloy

experienced significant plastic deformation. The dislocation density development and subgrain structure (e.g. dislocation cell) formation resulted in increased random crystalline orientations in the alloy, which can be seen in the uniform Debye rings. (Fig. 5.3(b)) Nevertheless, texture formation during plastic deformation caused additional variations of diffraction intensities in the azimuthal direction. The diffraction pattern in Fig. 5.3(b) shows the *duplex fiber texture*: [111]+[100]. Another important phenomenon that occurs after external loading is the change in shape of the Debye rings. Under the external applied stress, the spherical diffraction rings became ellipsoidal. The change in shape of the diffraction rings is the foundation for measuring lattice strain caused by the *macrostresses*, or Type I stress (see section 2.) Schematic interpretations of the changes in diffraction patterns for tensile response are shown in Fig. 5.4. The internal stress formed during vertical loading causes the radii of Debye rings to be shortened in the axial direction (Azimuth (η) = 90 and 270º) and lengthened in the transversal direction (Azimuth (η) = 0 and 180º). To deduce the lattice strain, ε, from the change in radii, an algorithm similar to those found in refs. 41, 42, 45 & 86 was applied to the diffraction patterns of Alloy 230. The detailed analysis procedure that was performed is detailed below:

1. Determined the beam center, detector tilt and sample-to-detector distance using software FIT2D [41, 42, 112] according to (200) and (333) reflections of reference material CeO_2.
2. Converted the diffraction pattern from polar to Cartesian coordinates through a re-binning processing. The converted images of the original diffraction patterns from Alloy 230 (Fig. 5.3) are shown in Fig. 5.5. 36 azimuthal bins were used in the study, corresponding to an angle increment of 10º.
3. Fitted diffraction peaks using a pseudo-Voigt function to find the average center of the peak intensity, $R(\eta)$. (Fig. 5.6) For each reflection, the radius profile changes with applied stresses with an intersection at a single radius. This radius, R_0, and its corresponding azimuth, η_0, are considered invariant during deformations. (Fig. 5.7) Thus, the lattice strain caused by applied stresses can be calculated by:

$$\varepsilon(\eta) = \frac{R(\eta) - R_0}{R_0} \qquad (5-1)$$

4. Applied the bi-axial strain model to determine the axial lattice strain, ε_{11}, and transversal lattice strain, ε_{22}, in the sample coordinate system. (ε_{11}= $\varepsilon(\eta$=90 or 270º) & ε_{22}= $\varepsilon(\eta$=0 or 180º)) (Fig. 5.8)

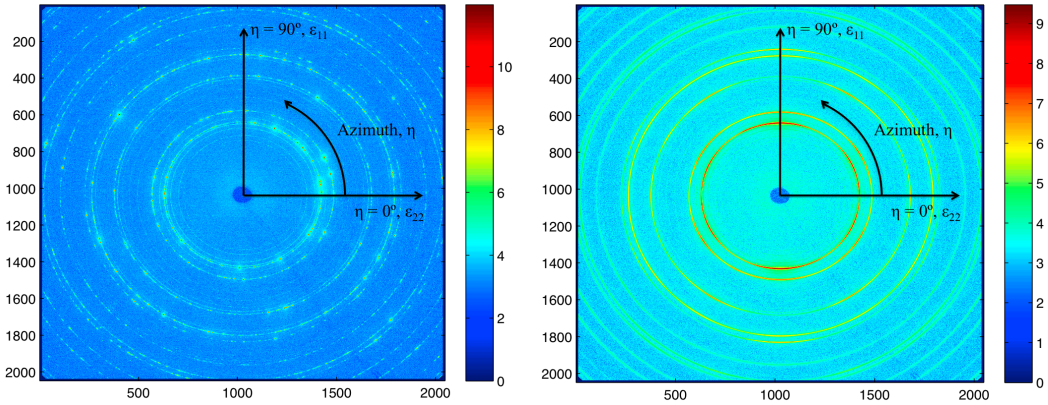

Fig. 5.3. Diffraction patterns from Alloy 230: before (a) and after (b) deformation

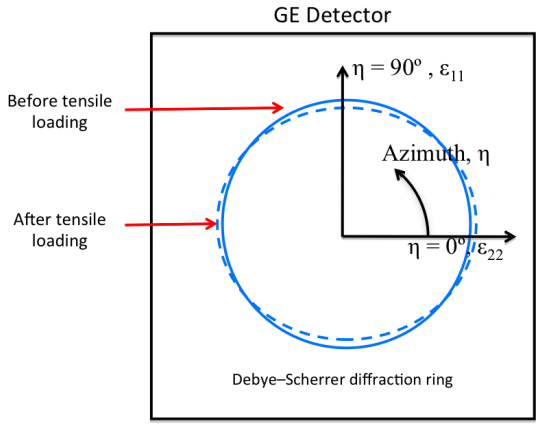

Fig. 5.4. Schematic interpretation of the changes in diffraction patterns for the tensile response

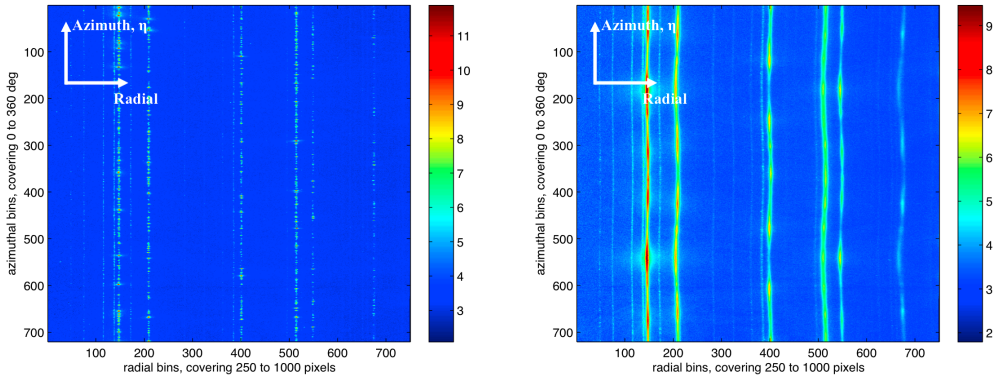

Fig. 5.5. Converted diffraction patterns from Alloy 230: before (a) and after (b) deformation

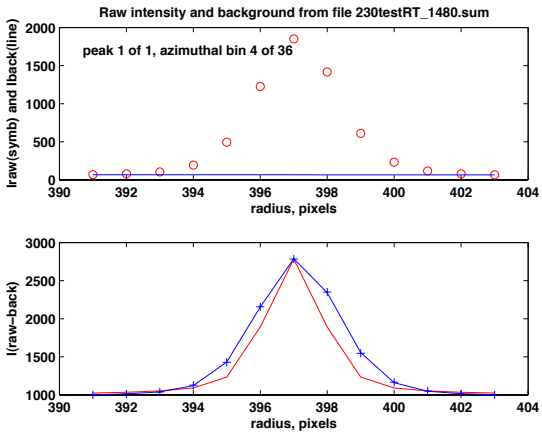

Fig. 5.6. Peak fitting using a Pseudo-Voigt function for the average center of the peak intensity

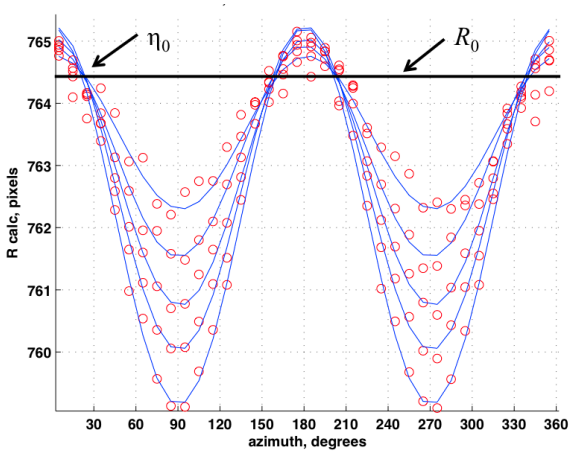

Fig. 5.7. Radius peak position versus azimuthal degree for the (311) reflection as a function of applied stresses for Alloy 230

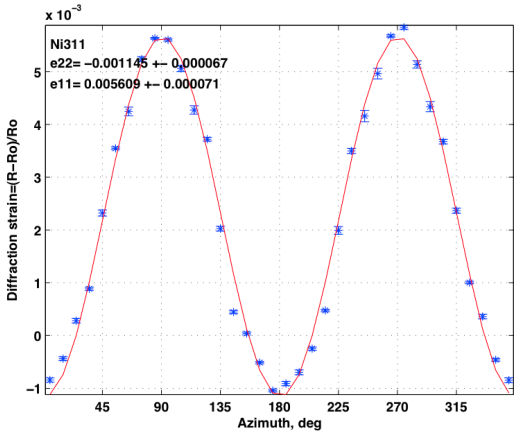

Fig. 5.8. Lattice strain analysis based on a profile fit of diffraction strain(ε) versus Azimuth(η)

5.1.2 X-RAY DIFFRACTION MEASURMENT FOR CREEP

Creep is defined as a slow straining at constant load or stress at elevated temperatures. Fig. 5.9 shows typical creep curves subdivided into three regions: primary, secondary and tertiary creeps according to deformation responses and mechanisms.

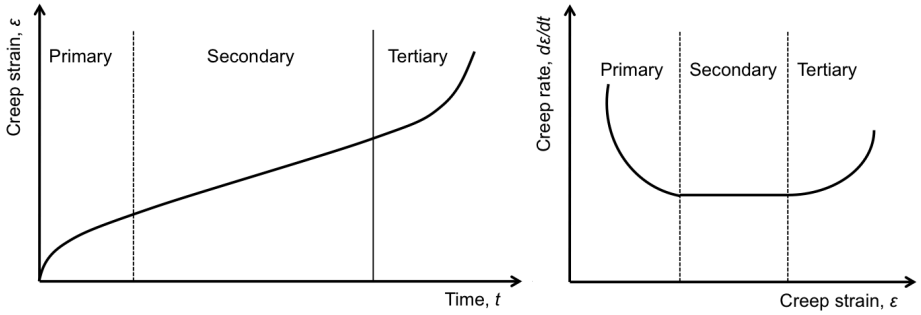

(a) (b)

Fig. 5.9. Typical creep curves: (a) creep strain versus time (b) creep rate versus creep strain

The primary creep is the initial stage of creep deformation and is characterized by a decrease in creep rate along with a corresponding increase in creep strain. This stage consists of a competing process of softening and hardening mechanisms under stress. The hardening (usually strain hardening) at elevated temperatures is believed to involve rearrangement of dislocations to form subgrain structures and dislocation tangling. In this case, dislocation movement is decelerated at a fixed stress. This process can be observed as a reducing strain rate:

$$(\frac{d^2\varepsilon}{dt^2})_h < 0 \text{ or } (\frac{d\dot{\varepsilon}}{dt})_h < 0 \qquad (5-2)$$

Conversely, the softening or recovery process involves a thermally activated cross-slip and edge dislocation climb. This process can be considered an acceleration of dislocations at a fixed stress and observed as an increasing strain rate:

$$(\frac{d^2\varepsilon}{dt^2})_s > 0 \text{ or } (\frac{d\dot{\varepsilon}}{dt})_s > 0 \qquad (5-3)$$

The overall creep deformation is the combination of the softening and hardening processes:

$$\frac{d^2\varepsilon}{dt^2} = (\frac{d^2\varepsilon}{dt^2})_h + (\frac{d^2\varepsilon}{dt^2})_s \qquad (5-4)$$

Since the hardening process is dominant, the creep rate decreases during the primary creep region:

$$\frac{d^2\varepsilon}{dt^2} < 0 \text{ or } (\frac{d^2\varepsilon}{dt^2})_h < -(\frac{d^2\varepsilon}{dt^2})_s \qquad (5-5)$$

As creep continuous, a balance between hardening and softening is developed, and hence the creep rate becomes constant:

$$\frac{d^2\varepsilon}{dt^2} = 0 \text{ or } (\frac{d^2\varepsilon}{dt^2})_h = -(\frac{d^2\varepsilon}{dt^2})_s \qquad (5-6)$$

The creep deformation then enters the secondary creep regime. Secondary creep is significant for high-temperature component design because accelerated creep deformation, and even fracture after a short period of time, will occur once deformation leaves secondary creep and enters the tertiary stage. The increased creep rate in tertiary stage is related to the creep void development. [33, 145] Therefore, it is important to maintain creep strain within a limited value (for example: <1% total elongation including strain on loading in the ASME B&PV Code, Section III, Subsection NH) for components used in high temperature systems.

Conventional creep tests can be conducted in a loading frame coupled with a high-temperature furnace using typical uniaxial creep specimens. [30-32] Creep strain development is obtained by measuring axial elongation of the specimens. Compared to conventional creep tests, the pressurized creep tube is a newer and more efficient approach to measure creep

strain development. The pressurized creep tube was developed primarily for reactor materials irradiation testing and fusion materials creep testing. [146-148] The miniature design enables multiple tubes to fit into a limited space under exposure to various environments (e.g. neutron irradiation in a reactor or a high temperature corrosive atmosphere in an experimental loop). The specimens are compact and rely only on internal pressure to produce desired stresses. As a result, the stress state in the pressurized creep tube is biaxial, which differs from the uniaxial state of conventional creep specimens. The biaxial creep deformation of the tube can be measured periodically using high precision laser measuring systems. In addition, the configuration of the creep tubes simulates heat transport and exchange tubing and piping in the NGNP system. Thus, results of creep tests can be better compared with realistic reactor situations.

Even though creep strain, rupture lives and partial environmental effects can be studied from *ex-situ* measurements on the pressurized tube, no microstructural information can be obtained in the creep study unless a destructive examination (e.g. SEM or TEM) is employed during or after experimentation. Real-time microstructural information (e.g. dislocation density or volume faction of voids and precipitates) is required to develop a fundamental understanding of constitutive creep behavior. The current study, however, presents a non-destructive measurement of internal creep mechanisms using synchrotron X-ray diffraction and pressurized creep tubes. The general setup is analogous to the setup of the uniaxial tensile experiment (described in section 5.1.1). The primary difference lies in the method in which external stresses are applied. Unlike mechanical loading for uniaxial tensile specimens, external stresses on the tube can be applied through the process of pressurizing high purity Argon gas within the tube to generate a biaxial stress state in the walls of the tube. Fig. 5.10 shows the configuration of the pressurized creep tube used in this study. 316L stainless steel was used in the study for the tube material. The inner pressure of the tube was ~1450psi, equivalent to a mid-wall hoop stress ~150MPa. Before the experiment, X-ray scanning in the transverse and longitude directions was conducted to position the synchrotron

beam in the center of the tube. The temperature was maintained at ~700ºC during the experiment.

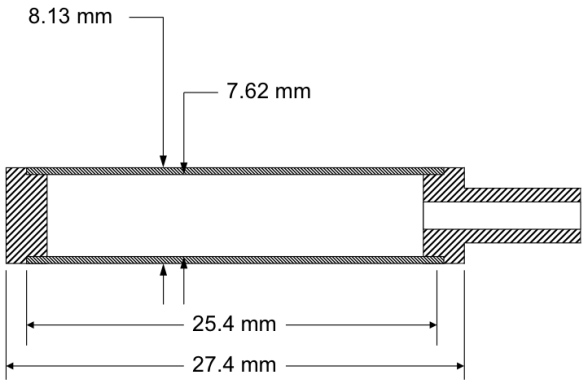

Fig. 5.10. Geometry of pressurized creep tube used in the study

5.2 HIGH-ENERGY X-RAY DIFFRACTION STUDY ON ALLOY 230

5.2.1 MATERIAL

Similar to the anisotropy study of Alloy 617 given in section 3.3, the long and short-transverse directions were used to fabricate two different types of tensile specimens. Fig. 5.11 shows a schematic of the studied specimens and their representative microstructures. The large, lamellar-shaped particles seen in the SEM images are tungsten rich M_6C type carbides. The volume fraction of the tungsten carbide is ~6%. Detailed discussion of the microstructure of Alloy 230 can be found in Chapter 3 & 4.

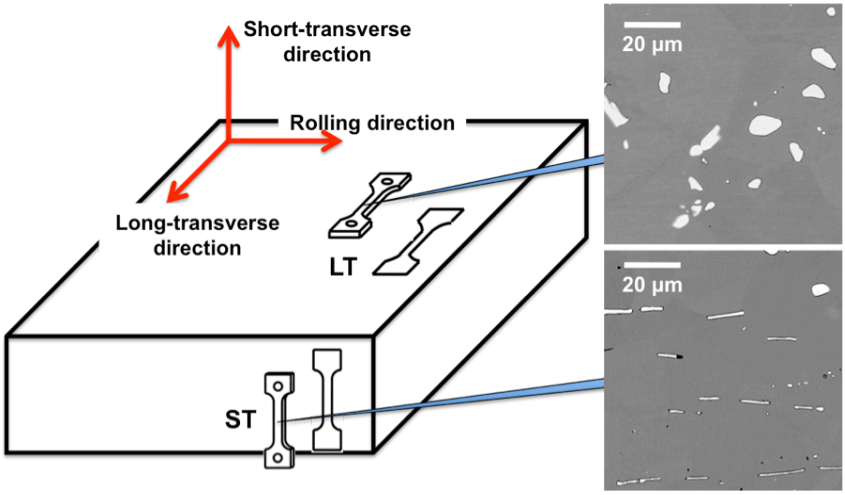

Fig. 5.11. In-plane sampling directions and microstructures of tensile specimens

Fig. 5.12 shows a representative X-ray diffraction pattern of Alloy 230 with phase and peak identifications. Despite low fractions of M_6C carbides, their diffraction rings can be clearly identified by a distinctive lower intensity compared to the reflections from the γ matrix. The most intense reflections for the carbide are (331), (422), (333), (440) and (822). The measured lattice constants for the γ matrix and the M_6C carbide are 3.58Å and 10.99Å, respectively.

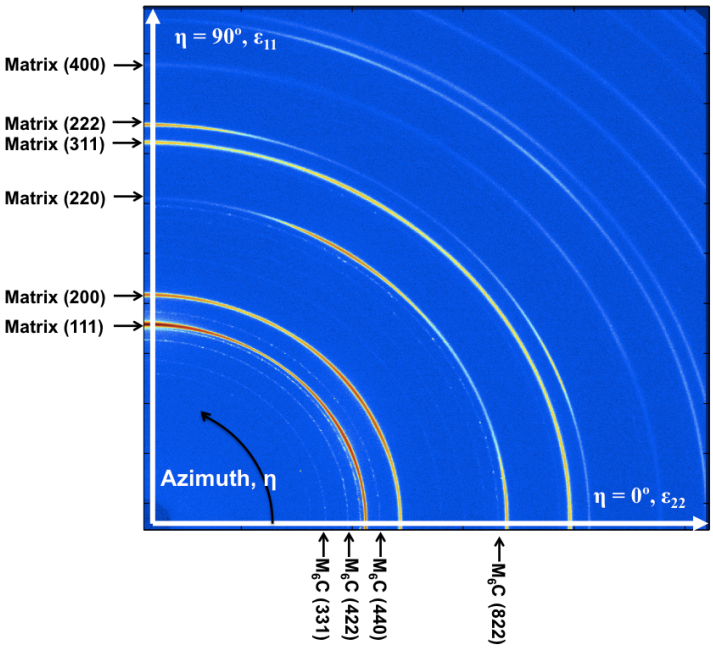

Fig. 5.12. Representative X-ray diffraction pattern (quarter of image plate) for Alloy 230. All Debye rings are identified as belonging to γ matrix and M_6C carbides

In order to have a large diffraction volume to measure the materials' bulk responses, the specimens were scanned for 10 different axial positions periodically during tensile testing. (Fig. 5.13) The diffraction volume for one single exposure was 300 x 300 x 760 μm^3. So, the total diffraction volume obtained from 10 scans is ~68.4 x 10^7 μm^3, which provides adequate statistics to extract the bulk response from the material.

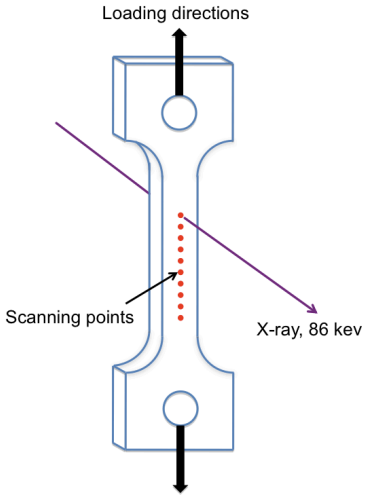

Fig. 5.13. Schematic of axial-scanning measurements.

5.2.2 MECHANICAL TESTS

The engineering strain-stress diagram for uniaxial tensile testing during *in-situ* XRD measurement is shown in Fig. 5.14(a). Both long-transverse (LT) and short-transverse (ST) specimens exhibited a typical tensile response under loading. However, similar to the anisotropy study on Alloy 617, considerable differences in tensile properties were found in two sampling directions. The 0.2% yield strength was equal to ~ 380 and 300MPa for LT and ST specimens, respectively. Even larger divergence was found in the tensile strength in the LT and ST directions, which are 576 and 839 MPa, respectively. Along with decreased U.T.S., the elongation for the ST specimen was 17%, which is much lower than the value for the LT specimen of 59%. Both specimens failed immediately when stress reached ultimate tensile strength so that necking was not apparent for either specimen.

Fig. 5.14(b) represents the true strain-stress diagrams for short- and long-transverse specimens converted from engineering strain and stress via equation 2-3 & 2.4. The true fracture stress for the LT specimen is ~1327MPa, or more than twice the value for the ST specimen of ~668MPa. The bulk Young's modulus for both specimens is ~211GPa, or the same as the value listed in the material profile. [36] The summarized tensile properties are shown in Table 5.1.

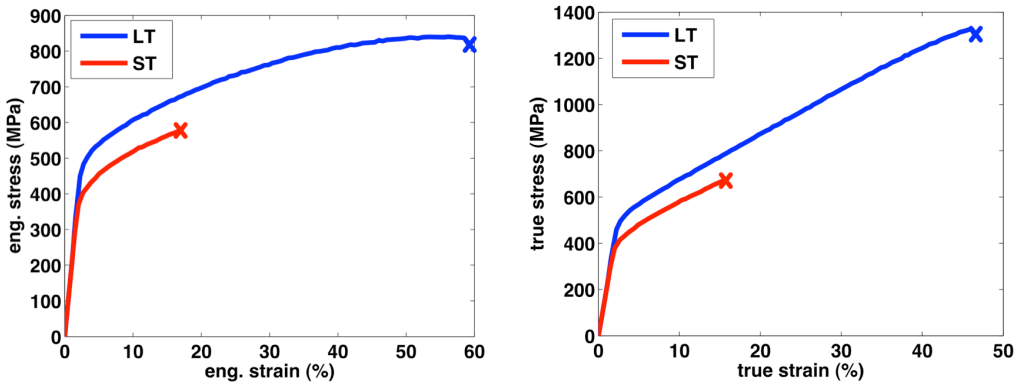

(a) (b)

Fig. 5.14. Macroscopic strain-stress diagrams for Alloy 230 tensile specimens in the long transverse (LT) and short transverse (ST) directions: (a) engineering stress versus engineering strain and (b) true stress versus true strain

Table 5.1. Mechanical properties for the long- and short-transverse specimens of Alloy 230

Direction/Properties	0.2% Y.S. (MPa)	UTS (MPa)	Elongation (%)	Fractured stress (MPa)
Long-transverse	380	839	59	1327
Short-transverse	300	576	17	668

5.2.3 ELASTIC CONSTANT DETERMINATION

An important question must be answered before further discussion takes place: how are the measured *hkl*-specific strains interpreted to attain internal stress? The typical expression for the relation of the strain components, ε_{ij}, and stress components, σ_{ij}, is:

$$\sigma_{ij} = C_{ijkl}\varepsilon_{kl} \qquad (5-7)$$

or

$$\varepsilon_{ij} = S_{ijkl}\sigma_{kl} \qquad (5-8)$$

In these equations, C_{ijkl} is the fourth-rank stiffness tensor and S_{ijkl} is the fourth-rank compliance tensor. For a given material, the values of C and S for single crystal are different from polycrystalline because there are significant interactions between gains in the polycrystalline structure. Therefore, a bar is often added to C and S to distinguish the stiffness

and compliance for macroscopic polycrystalline from the corresponding values for a single crystal:

$$\sigma = \overline{C}\varepsilon \quad \& \quad \varepsilon = \overline{S}\sigma \tag{5-9}$$

In the case of an isotropic polycrystalline material with cubic crystal structure, $\overline{C}$ can be expressed by two independent elastic constants, i.e. Young's modulus, *E*, and Poisson's ratio, *v*. The equation 5-9 can then be simplified to:

$$\sigma_{ij} = \frac{E}{(1+v)}[\varepsilon_{ij} + \frac{v}{(1+2v)}(\varepsilon_{11} + \varepsilon_{22} + \varepsilon_{33})] \quad , \tag{5-10}$$

In this relation, *i, j* =1, 2, 3, … indicate the components relative to chosen axes [103]. For an anisotropic system (e.g. a single crystal), *E* and *v* depend on the loading direction, which is defined by *hkl* in a cubic system. Although the polycrystalline is generally treated as isotropic, the material is composed of aggregated monocrytals with anisotropic properties. Additionally, the elastic behavior in the polycrystalline involves an interaction between grains. Therefore, precise interpretation from lattice strains to internal stresses (the question posed at the beginning of this section) will essentially require a complete solution of the influence of elastic anisotropy for every grain and their respective interactions. Since this solution is extremely difficult to obtain, various models have been proposed for modeling interaction between crystallites based on single crystal behavior. [69, 103, 113] The most widely used models are: Reuss's, Voigt's and Kröner's. These models were initially introduced to predict the overall response (e.g. bulk, shear and Young's moduli and Poisson's ratio) of polycrystalline materials based on their elastic constants for monocrytal. Nevertheless, the monocrystal are elastic anisotropic, and hence, the *hkl*-specific response for polycrystalline aggregates can also be simulated using these models.

Voigt Model:

The basic assumption of the Voigt model is that all grains in a polycrystalline aggregate experience the same uniform strain. Thus, the elastic properties can be calculated by averaging the stiffness constants (*C*) over all crystallites. For cubic materials (e.g. fcc or

bcc) E and v for polycrystalline aggregate can be obtained by calculating the bulk modulus, K, and shear modulus, μ:

$$K = \frac{1}{3}(C_{11} + 2C_{12}) \qquad (5-11)$$

$$\mu = \frac{1}{5}(C_{11} - C_{12} + 3C_{44}) \qquad (5-12)$$

Then, E and v can be given as:

$$E = 2(1+v)\mu \qquad (5-13)$$

$$v = \frac{3K - 2\mu}{2(3K + \mu)} \qquad (5-14)$$

One should note that the obtained values for E and v in the Voigt Model are independent of crystallographic direction, *hkl*.

Reuss Model:

The basic assumption of the Reuss model is that all grains in a polycrystalline aggregate experience the same amount of stress. For each crystallite, the lattice strain developed by the applied stress is dependent on the elastic anisotropy of a single crystal. In this hypothesis, elastic constants for the polycrystalline are *hkl*-specific and can be computed by:

$$E(hkl) = \frac{1}{S_{11} - 2S_0 A_{hkl}} \qquad (5-13)$$

$$v(hkl) = -\frac{S_{12} + S_0 A_{hkl}}{S_{11} - 2S_0 A_{hkl}}\ , \qquad (5-14)$$

where,

$$S_0 = S_{11} - S_{12} - \frac{1}{2S_{44}} \qquad (5-15)$$

$$A_{hkl} = \frac{h^2k^2 + h^2l^2 + l^2k^2}{(h^2 + k^2 + l^2)^2} \qquad (5-16)$$

S_0 is a factor related to the amount of elastic anisotropy for a material (Note: Zener anisotropy factor is $2(S_{11}\text{-}S_{12})/S_{44}$). A_{hkl} and $3A_{hkl}$ are known as the anisotropy factor [103] and orientation parameter [149], respectively.

Kröner Model:

Both of the models proposed by Voigt and Reuss are based on idealized situations where strain or stress is identical over all elements of the aggregate. In contrast, Kroner's model considers the stress and strain individually according to the Esheby's 'self-consistent approach'. [150] In this self-consistent model, each grain is treated as an inclusion particle imbedded in a homogenous matrix, and its strain-stress relations can be expressed as:

$$\sigma_{ij} = (C_{ijkl} + r_{jjkl}(\Omega))\varepsilon_{kl} \qquad (5-17)$$

or

$$\varepsilon_{ij} = (S_{ijkl} + t_{jjkl}(\Omega))\sigma_{kl} \qquad (5-18)$$

,

In these formulas, C_{ijkl} and S_{ijkl} are the stiffness and compliance tensors, respectively, of a single crystal of volume Ω, and r_{ijkl} and t_{ijkl} are tensors that describe the interaction between grains. Following integration of equation 5-17 or 5-18 over all orientations, the macroscopic average values for the bulk material (denoted by subscript B) can be obtained:

$$\bar{\sigma}_{ij} = (C_{ijkl})_B \bar{\varepsilon}_{kl} \qquad (5-19)$$

or

$$\bar{\varepsilon}_{ij} = (S_{ijkl})_B \bar{\sigma}_{kl} \qquad (5-20)$$

And thus,

$$\int_D r_{ijkl} dD = \int_D t_{ijkl} dD = 0 \qquad (5-21)$$

In this equation, D is total volume of the body for analysis. The relations of r_{ijkl}, t_{ijkl}, C_{ijkl}, S_{ijkl}, $(C_{ijkl})_B$ and $(S_{ijkl})_B$ can be determined and are dependent on the shape of grains and their crystal structure (e.g. cubic or hexagonal structures). Therefore, $E(hkl)$ and $v(hkl)$ can be obtained

through an iterative computation. [69, 103, 113, 149] More details concerning the computation can be found in APPENDIX B.

Several examples are provided herein to clarify the difference between these models. The four selected materials are Cu, Al, W and Nb, whose values of single-crystal elastic constants are given in Table 5.2. Based on the single-crystal elastic constants, Young's moduli for the polycrystalline metals are simulated by the models of Voigt, Reuss and Kröner and are shown in 3D (Fig. 5.15) and 2D (Fig. 5.16) plots. As previously discussed, the orientation dependence of Young's modulus for polycrystalline materials is different in each of the three models. The simulated Young's moduli using Voigt's model are independent of *hkl*. In sharp contrast, the Young's moduli calculated by Reuss's model show a strong orientation dependence, particularly clear for the difference between the [111] and [100] directions. Kröner's model, in general, yields values close to the average of the Voigt and Reuss limits. Beyond the comparison between these models, the impact of the Zener anisotropy factor is notable in the model results that yield different geometries in 3D contouring (Fig. 5.15) and different curves in 2D plots (Fig. 5.16). For Cu with an anisotropy factor of 3.2, the Young's modulus is highest in the [111] direction and decreased to the minimum in the [100] direction according to both Reuss's and Kröner's models. For a material with an anisotropy factor close to 1 (e.g. Al and W) the orientation dependence of Young's modulus is insignificant. In the case of Nb, the maximum Young's modulus appears in the [100] direction, and the value decreases to the minimum in the [111] direction because the anisotropy factor of Nb is $0.5<1$.

Among these models, Kröner's model is considered to be the most realistic for calculating overall and *hkl*-specific responses for polycrystals. The calculated results are close to experimentally determined values. [113] Therefore, Kröner's model will be employed for the lattice strain/internal stress conversion for the γ matrix of Alloy 230 in the following discussion.

Table 5.2. Values of single-crystal elastic constants for selected materials

Material	Crystal Structure	C_{11} (GPa)	C_{12} (GPa)	C_{44} (GPa)	$2(C_{44})/(C_{11} - C_{12})$
Cu	FCC	168.4	121.4	75.4	3.2
Al	FCC	107.3	60.9	28.3	1.2
W	BCC	522.4	204.4	160.8	1
Nb	BCC	240.2	125.6	28.2	0.5

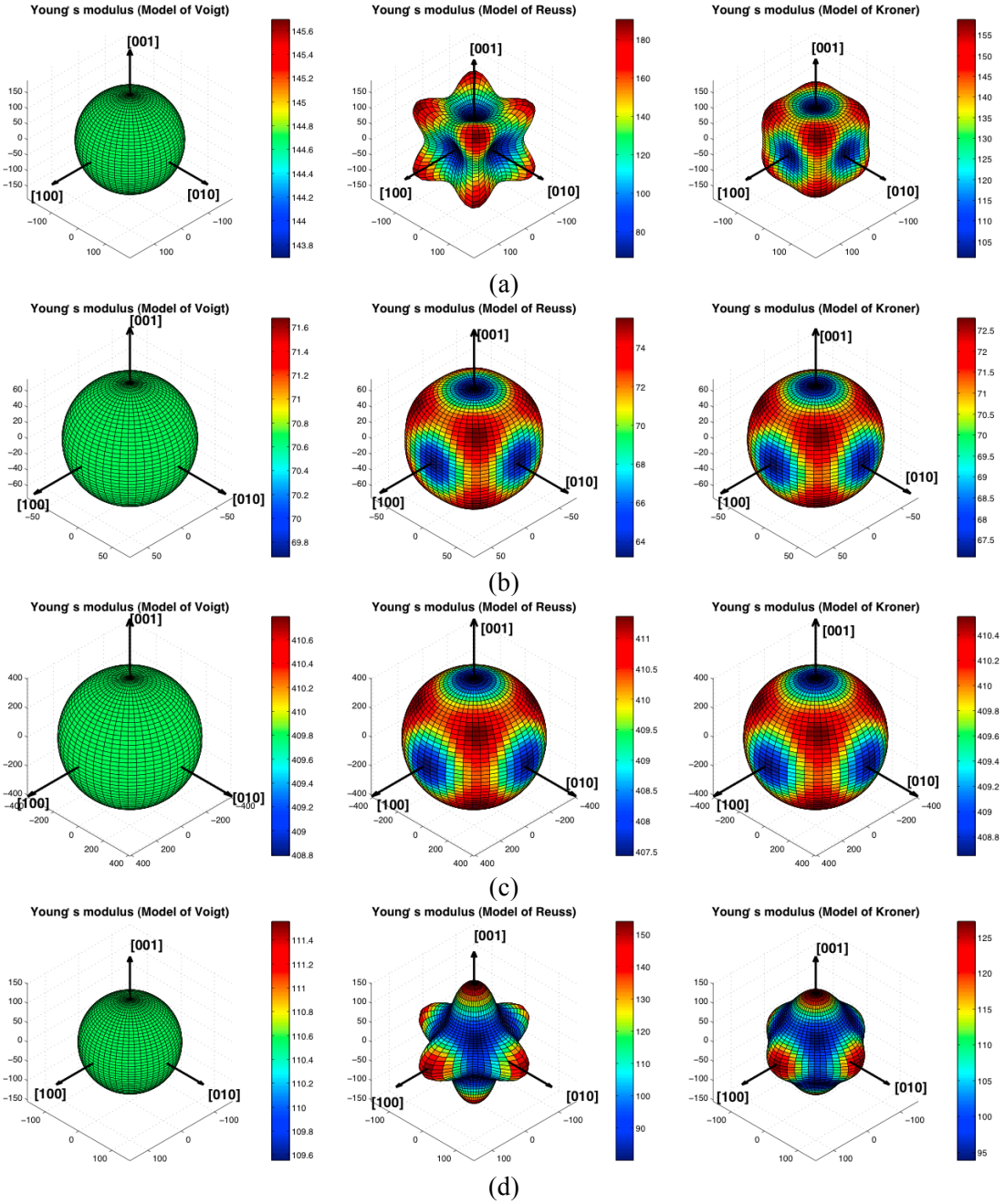

Fig. 5.15. Orientation dependence of Young's modulus (unit: GPA) for polycrystalline aggregate: (a) Cu (b) Al (c) W and (d) Nb

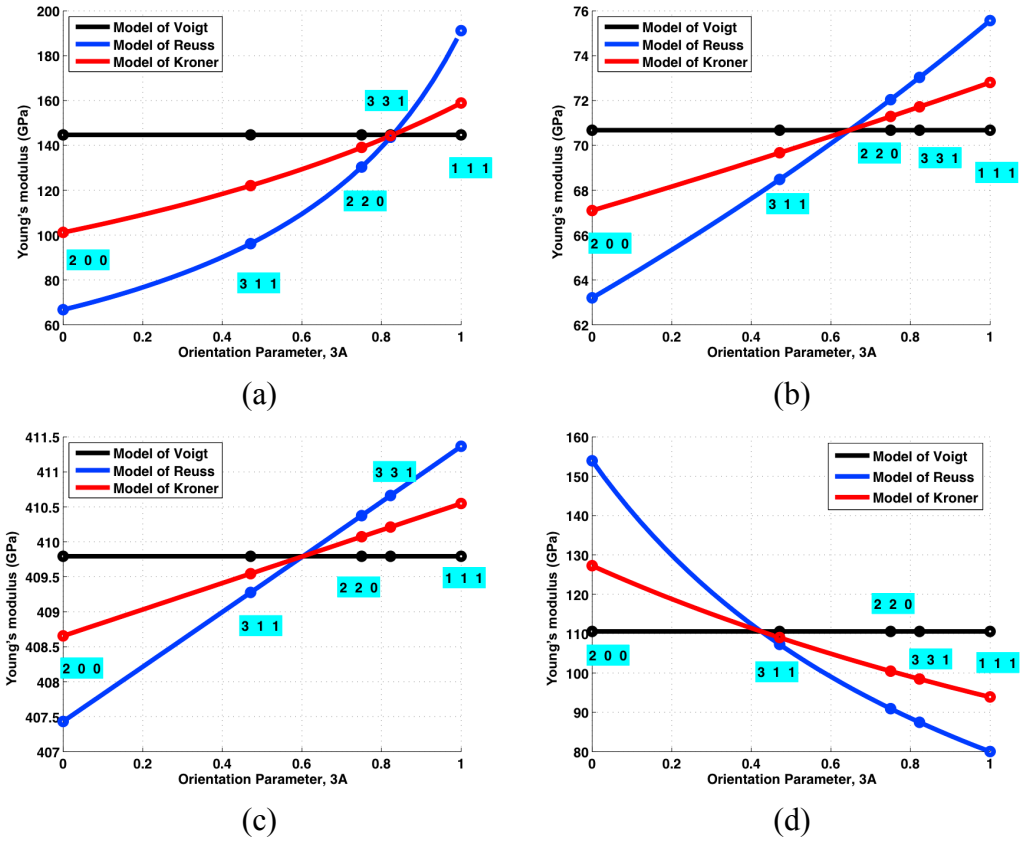

Fig. 5.16. Elastic anisotropy of Young's modulus: (a) Cu (b) Al (c) W and (d) Nb

5.2.4 ELASTIC RESPONSE OF THE AUSTENITIC MATRIX

Fig. 5.17 shows the lattice strain development for different reflections of the γ matrix in the long-transverse (LT) Alloy 230 specimen. The results from a single scanned position (Fig. 5.13) provide sufficient information for analyzing the elastic anisotropy. During tensile loading, the (222) reflection shows the stiffest strain-stress loading curves, a result of the highest Young's modulus in the [111] orientation. For the same reason, the (200) reflection shows the more compliant behavior compared to the other reflections. The lower lattice strain in the transversal direction (ε_{22}) relative to the axial direction (ε_{11}) is the result of the Poisson effect, which can be expressed as: $\varepsilon_{22} = -\nu\varepsilon_{11}$ (ν is the Poisson's ratio, typically ~0.2-0.5 for metals). This elastic anisotropy of the γ matrix is analogous for both alloys, with each showing an almost linear lattice strain development to the applied stress during both elastic and plastic deformations. Fig. 5.18 shows the lattice strain development for different reflections of the γ matrix in the short-transverse (ST) Alloy 230 specimen. In spite of an

earlier rupture, the anisotropic loading behavior for the ST specimen during *in-situ* tensile testing is analogous to the LT specimen.

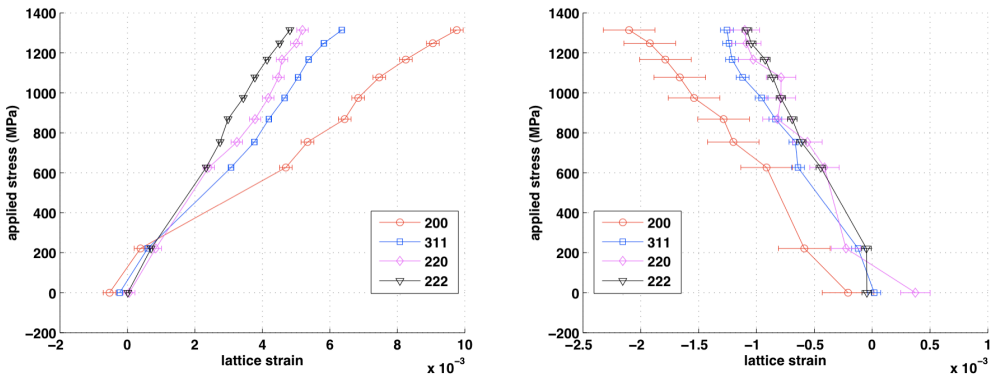

Fig. 5.17. Lattice strain generated during *in-situ* tensile tests in the long-transverse Alloy 230 specimens: (a) axial direction, ε_{11} (b) transversal direction, ε_{22}

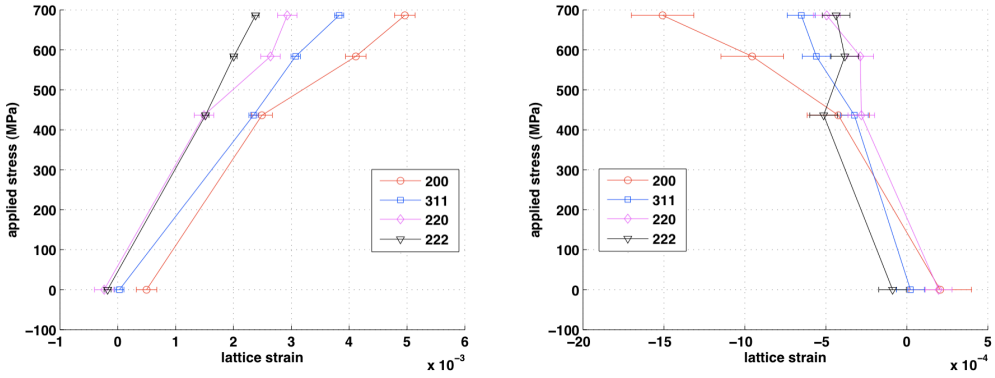

Fig. 5.18. Lattice strain generated during *in-situ* tensile tests in the short-transverse Alloy 230 specimens: (a) axial direction, ε_{11} (b) transversal direction, ε_{22}

Since the single crystal data for both alloys are not available presently, the elastic constants for single crystal nickel were preliminary used in this study. C_{11}, C_{12} and C_{44} for single crystal nickel are 250, 151 and 123 GPa, respectively, and the Zener anisotropy factor is ~2.5. [151] Fig. 5.19 and 5.20 show the results for *E(hkl)* calculated by Kröner's model with a comparison with the Voigt and Reuss limits. The orientation dependence of Young's modulus for Ni is typical for FCC alloys with a high anisotropy factor, which is analogous to modeling results of Cu in Fig. 5.15(a) and 5.16(a).

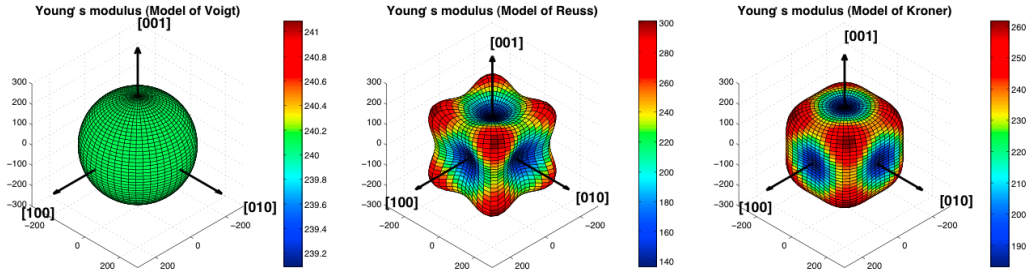

Fig. 5.19. Orientation dependence of Young's modulus (unit: GPA) for Ni polycrystal

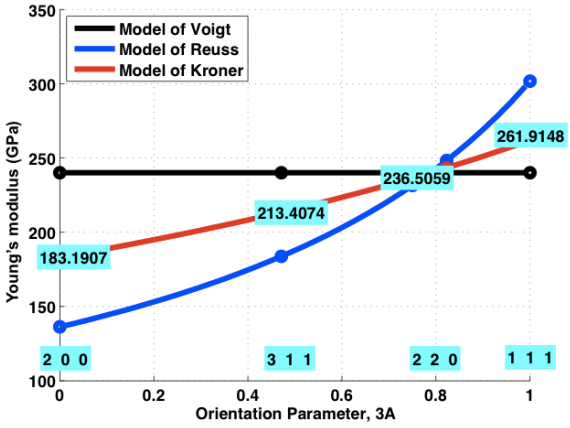

Fig. 5.20. Elastic anisotropy of Young's modulus for Ni

Based on the modeled *E(hkl)*, the measured lattice strains for different reflections can be converted into internal stresses according to equation 5-10. Therefore, the axial and transversal internal stresses (represented by σ_{11} and σ_{22}, respectively), can be expressed as:

$$\sigma_{11} = \frac{E}{1+\nu}\varepsilon_{11} + \frac{\nu E}{(1+\nu)(1-2\nu)}(\varepsilon_{11}+\varepsilon_{22}+\varepsilon_{33}) \qquad (5-22)$$

$$\sigma_{22} = \sigma_{33} = \frac{E}{1+\nu}\varepsilon_{22} + \frac{\nu E}{(1+\nu)(1-2\nu)}(\varepsilon_{11}+\varepsilon_{22}+\varepsilon_{33}) \qquad (5-23)$$

Since the tensile tests are uniaxial, ε_{22} can be considered equal to ε_{33} and $\nu = -\varepsilon_{22}/\varepsilon_{11}$. If we assume that the *hkl*-specific ν and E are constant during deformations, Eq. 5-22 can be simplified to:

$$\sigma_{11} = E\varepsilon_{11} \qquad (5-24)$$

In this equation, E and ε_{11} are obtained from modeling and XRD measurements, respectively.

Fig. 5.21 shows the results for internal stress development in the long-transverse specimen with a comparison to true stress. (Note that XRD measurements from all ten scanned positions are employed to obtain sufficient statistics to extract the average response from the bulk material.) The internal stresses measured from (311), (220) and (222) reflections are in good agreement with the true stresses. The internal stresses measured from the (200) reflection are slightly higher than the true stresses, which could be caused by the slightly overestimated $E(111)$ determined by modeling. Generally, the XRD measured lattice strains with modeled Young's moduli provided satisfactory results for the internal stresses, whose values are analogues to true stresses from the mechanical measurement.

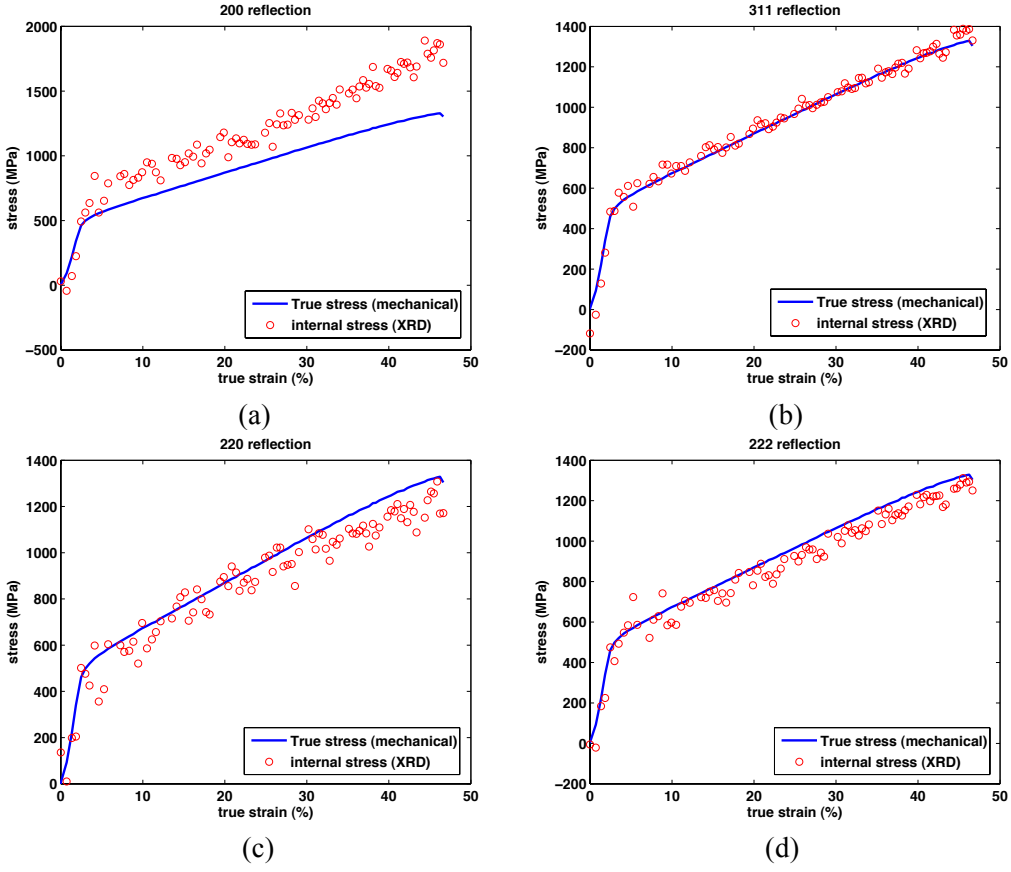

Fig. 5.21. The results of internal stress in the contrast to the true-stress

One should note that the measured internal stresses obtained from the (311) reflection possess the least amount of data scattering and provide the best fit to true stresses. (Fig. 5.21(b)) Previous studies confirm that (311) reflection is the suitable representation for

characterization of macroscopic stresses and strains for FCC metals. [152] Therefore, the (311) reflection from the γ matrix was selected for further discussion in the following section.

5.2.5 PARTICLE PARTICIPATION DURING LOADING

Among all measurable reflections, the (422) reflection for the M_6C carbide is selected for the strain-stress analysis, not only because of its relatively high intensity, but also due to its reciprocal space location where no intense reflection from the γ matrix is around. In fact, unlike the high anisotropy of the γ matrix, the elastic constants for the M_6C carbide are nearly orientation (*hkl*) independent. Li et al. modeled three typical types of M_6C carbides: Fe_3W_3C, Co_3W_3C and Ni_3W_3C, and obtained their respective Zener anisotropy factors that are 0.9725, 0.8740 and 0.9248. [153] (Note that Ni_3W_3C is close to the M_6C carbide used in this study.) Since the anisotropy factor for M_6C carbides is close to 1, the carbide values of Young's moduli for various (*hkl*) reflections are essentially equal.

Fig. 5.22(a)&(b) show the lattice strain development for both the γ matrix and the M_6C carbide, respectively. The lattice strain for the γ matrix responds almost linearly to the external applied stress with a slightly decreased slope once the material yields. In contrast, the lattice strain evolution for the M_6C carbide is not linear during deformations and can be essentially divided in three stages: (1) the linear lattice strain development during elastic deformation, (2) the accelerated straining during the alloys' early yielding and (3) the gradually decreased lattice strain during plastic deformation. This process is typical for the carbides in the long-transverse specimen, but not apparent in the short-transverse specimen. This difference can be seen in the individual analyses of strain development for the long-transverse and short-transverse specimens in Fig. 5.23(a) and 5.23(b), respectively. The lattice strain of the carbide in the short-transverse specimen increases moderately without a dramatic loading behavior during early yielding. Nevertheless, it should be noted that there is a maximum lattice strain for the carbide for both specimens, which occurs immediately after the alloy yields. The value of this critical lattice strain was found to be ~0.0047, corresponding to an internal stress of ~1344MPa (the Young's modulus of M_6C carbide is

~286GPa [154]). The short-transverse specimen fails immediately once the carbide achieves this critical internal stress, while the long-transverse specimen conducts further plastic deformation with decreasing carbide lattice strain until failure occurs. (Fig. 5.22(a))

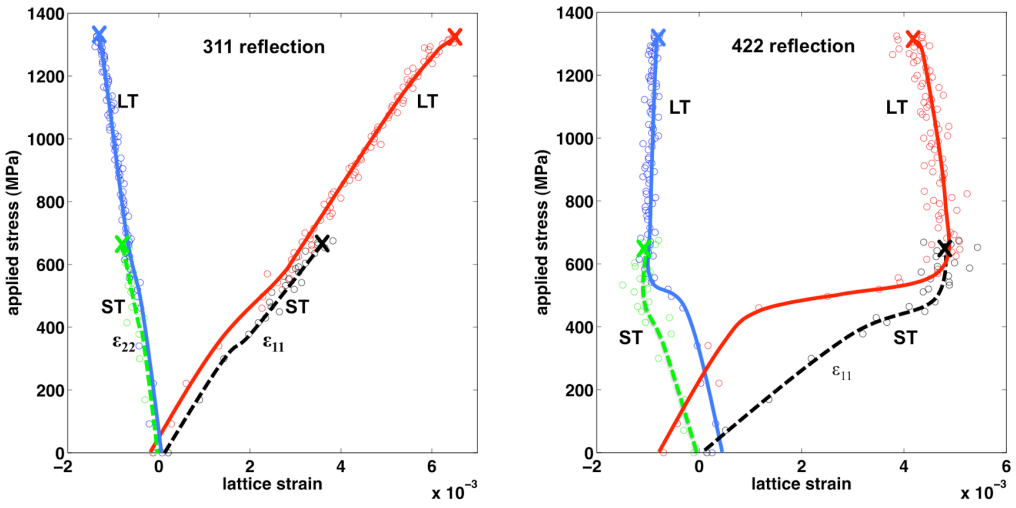

(a) (b)

Fig. 5.22. Applied stress versus lattice strain (ε_{22}: lattice strain perpendicular to applied stress and ε_{11}: lattice strain parallel to applied stress) for (a) the γ matrix ((311) reflection) and (b) the M_6C ((422) reflection). Note: The solid and dash lines are curves fitted though the data points to show the trend.

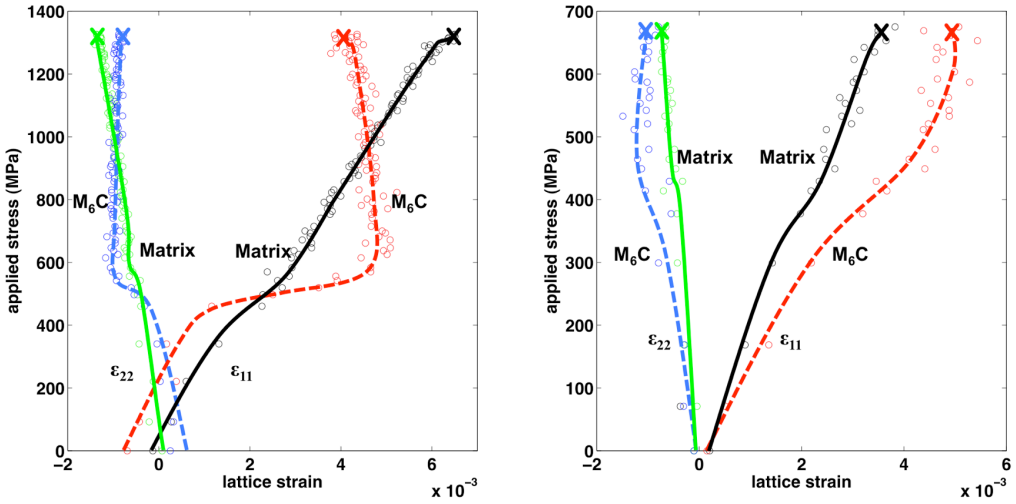

(a) (b)

Fig. 5.23. Applied stress versus lattice strain (ε_{22}: lattice strain perpendicular to applied stress and ε_{11}: lattice strain parallel to the applied stress) for the γ matrix ((311) reflection) and the M_6C ((422) reflection) in (a) long-transverse and (b) short-transverse directions. Note: The solid and dash lines are curves fitted though the data points to show the trend.

5.2.6 DISCUSSION OF THE TENSILE EXPERIMENT

The γ matrix in the long-transverse and short-transverse samples of Alloy 230 has a similar response as the lattice strain development during tensile loading, although an early failure occurs for the short-transverse specimen. The materials' elastic anisotropy is revealed by different responses of *hkl*-specific reflections, which are typical for FCC metals. [152, 155] Calculated from Kröner's self-consistent method, Young's moduli for different (*hkl*) reflections provide a sufficient approximation for converting measured lattice strains to internal stresses. Although this analysis only considers one phase, the results agree well with true stresses from the mechanical measurement. (Fig. 5.21) The analysis also suggests that the load transferred from the γ matrix to second-phase particles is insignificant in Alloy 230 during deformation at room temperature.

One should take note of the observed Bauschinger effect in the Alloy 230 specimens. The difference in Y.S. between long- and short-transverse specimens was found to be ~ 80 MPa from mechanical measurements. (Table 5.1) This can be predicted by the measurement of residual stress in the specimens before tensile loading. The measured lattice strains parallel to the applied stress (ε_{11}) are -1.21×10^{-4} and 2.76×10^{-4} for long- and short-transverse specimens, respectively. (Fig. 5.22 & 5.23) Thus, the corresponding difference in residual stress is 83 MPa, which agrees well with the mechanical measurement.

The deformation process of carbide particles in Alloy 230 can be revealed by analyzing the lattice strain responses for the long-transverse specimen. During the alloy's elastic deformation, the lattice strain of the carbide increases linearly with increasing external applied stress. The lattice strain dramatically increases during early yielding until it reaches its maximum value. This process is the result of significant dislocation movements during material yielding and, consequently, a great number of dislocations that bow around large non-deformable particles. However, unlike the sustained loading behavior of the particles in refs. 42 & 86, the lattice strain of the M_6C carbide in Alloy 230 cannot increase during plastic deformation. Instead, lattice strain gradually decreases, in contrast to the linear straining of the γ matrix. This indicates that the large carbides with low volume fractions cannot maintain

large internal stresses and begin to rupture upon early yielding. The continued particle fracture process results in a decreasing loading capacity (therefore reducing the lattice strain) during plastic deformation. The particle's maximum internal stress, achieved during early yielding in the material, can be defined as the critical fracture stress for the M_6C type carbide in Alloy 230. This is the maximum internal stress that the M_6C carbide is able to withstand. Particle fracture will initiate once the internal stress is greater than this critical value (~1344 MPa, corresponding to the lattice strain of ~0.0047).

Because of the residual stress on the particles as well as the early rupture of the specimen, the loading behavior of the carbide in the short-transverse specimen cannot be divided into multistage as seen in the long-transverse specimen. However, the carbide in both specimens achieved the same value of lattice strain (~0.0047) after yielding. (Fig. 5.22(b)) This confirms the analysis for the critical fracture stress in the long-transverse specimen. Moreover, the analysis of the short-transverse specimen suggests that the critical fracture stress for the M_6C type carbide in Alloy 230 is independent of loading orientation. In other words, the loading direction on the specimens, either long- or short-transverse, will not change the initial stress of carbide fracture. Note that the M_6C carbide is lamellar-shaped and embedded in the γ matrix. (Fig. 5.11) From the mechanical tests on Alloy 230 (also seen in the effect of orientation of Alloy 617, section 3.3), the anisotropic geometry of the carbide as well as their distribution in the material are found to have an impact on all tensile properties. (Fig. 5.14 & Table 5.1) Nevertheless, the maximum stress that the carbides can withstand is found to be independent of their shape and distribution in the alloy.

Complementary studies using SEM analysis for the ruptured specimens are shown in Fig. 5.24. Similar to the anisotropy of Alloy 617, the early failure of the short-transverse Alloy 230 specimen is caused by the ligament of carbides bands, and most of the carbides still maintain their integrity after the sample rupture. (Fig. 5.24 (b)) In contrast, almost all of the carbides fractured in the ruptured long-transverse specimen. (Fig. 5.24(a)) The difference in the carbide integrity explains the observation of different lattice strains (therefore different internal stresses) when the specimens fail.

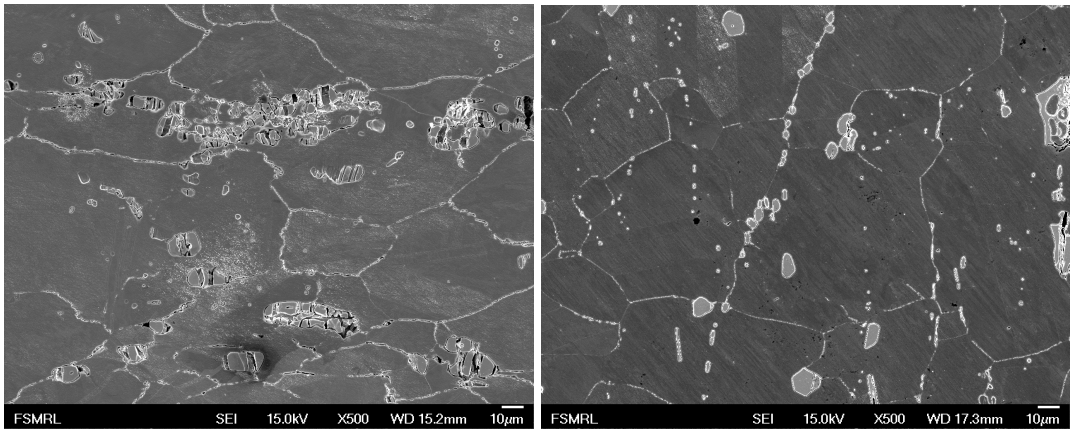

(a) (b)

Fig. 5.24: Carbide fractures in ruptured specimens: (a) long-transverse and (b) short-transverse

Finally, it must be noted that the present study is based on tensile tests conducted at room temperature. Since both alloys are expected to be used at high temperatures, the actual loading behavior for both γ matrix and carbides might differ from that found during tests at low temperatures. The high-energy synchrotron technique can be further applied to study high-temperature mechanical behavior for Alloy 230 (e.g. creep and creep-fatigue).

5.3 IN-SITU CREEP STUDY USING PRESSURIZED CREEP TUBES

5.3.1 METHODS

A typical diffraction pattern from a pressurized creep tube is shown in Fig. 5.25. The enlarged image, sampled from a part of the diffraction pattern (in red square of Fig. 5.25), shows that each reflection forms two Debye–Scherrer diffraction rings that are generated from the two sides of the tube. Fig. 5.26 shows the procedures to extract the diameter of the pressurized tubes from diffraction patterns. The basic steps for the creep strain analysis are: first, measure the distance, *a*, between two diffraction rings for a single reflection (e.g. (311) reflection); second, calculate the diameter of the tube, *D*, based on a tangent angle relation with *a*; and third, evaluate the creep strain by comparing the value of diameter before and after various stages of creep deformation. (Fig. 5.26(a)) However, due to elastic anisotropy, the distance between two diffraction rings is not a constant value at various azimuths.

Therefore, a polar re-binning processing turning pixel intensity data into radius/angle (R/μ) with respect to the pattern center was performed. This was followed by a peak fitting in R to determine the center of each diffraction peak in pixels. (Fig. 5.26(b)) Then, the distance of two diffraction rings, which is also the mean distance between two diffraction peaks for azimuth from 0 to 360º, can be calculated by:

$$\bar{a} = 0.2\text{mm} \times \frac{1}{n}\sum_{n=1}^{n}(P1(\eta) - P2(\eta)) \qquad (5-25)$$

In this equation, n is the number of bins used during the polar re-binning process (n=36 in this study) and $P1$ and $P2$ are radii in pixels of fitted peak 1 and peak 2, respectively. The distance between two diffraction rings has a factor of 0.2mm, which is the dimension of one pixel in the GE detector. Then, we can obtain the diameter of the tube, D, by the expression:

$$D = a / \tan(2\theta) \qquad (5-26)$$

Relative changes in the tube diameter during the experiment can be calculated with respect to the initial state denoted by subscript 0 and can be converted to the mid-wall hoop strain by use of a factor of 1.063:

$$\varepsilon = 1.063\frac{D^* - D_0}{D_0} \qquad (5-27)$$

In the above formula, D_0 is the diameter obtained from Eq. 5-26 for the initial state, and D^* is the diameter during creep. The assumption imperative for Eq. 5-27 is that the material is incompressible and deforms uniformly during creep [156]. More details for converting tube diameter into strain can be found in ref. 157. Finally, since tan(2θ) is nearly constant during the measurement, D_0 and D^* in Eq. 5-27 can be replaced with their values from Eq. 5-26, to yield the much simpler equation:

$$\varepsilon = 1.063\frac{\bar{a}^* - \bar{a}_0}{\bar{a}_0} \qquad (5-28)$$

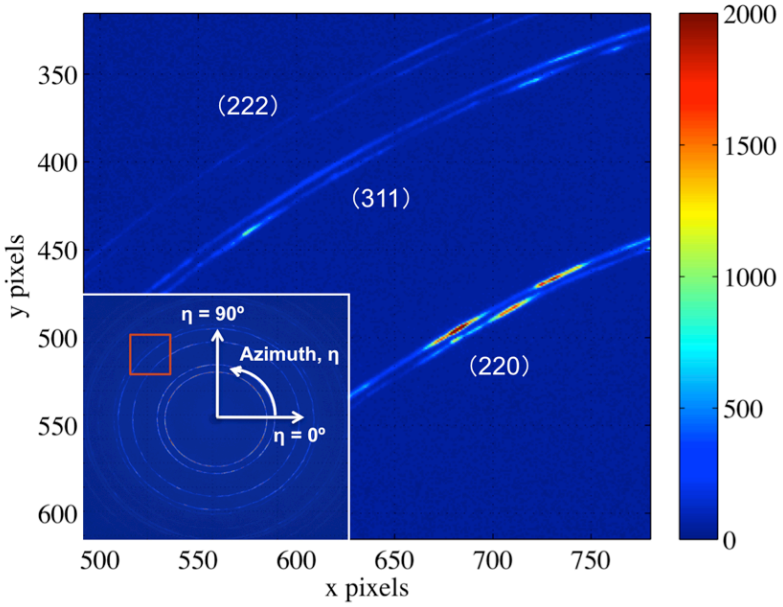

Fig. 5.25. Representative diffraction patterns for a pressurized creep tube

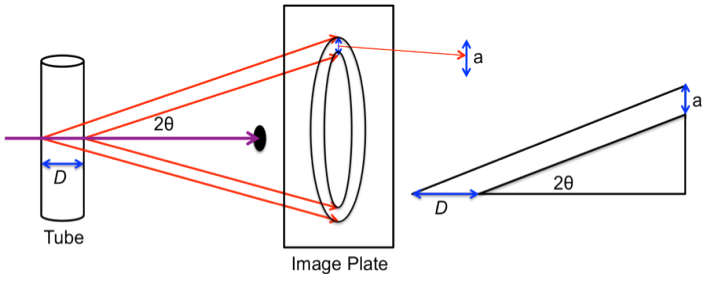

(a)

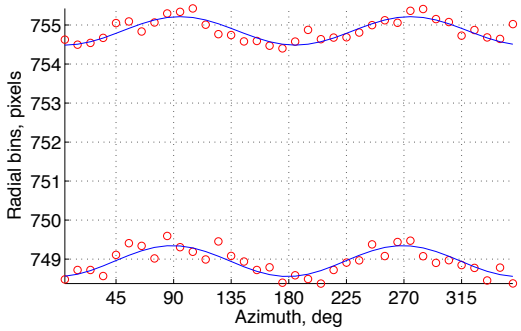

(b)

Fig. 5.26. Diameter measurements for the pressurized creep tube: (a) Schematic representations of the measurement (b) Radius peak position versus azimuth for dual (311) diffraction rings (in red circles) and the fitting on the radius profile for lattice strain analysis (in blue lines)

5.3.2 RESULTS

Based on Eq. 5-28, the macroscopic creep strain can be found directly by using the distance between two diffraction rings obtained in Eq. 5-25. Fig. 5.27 shows the results from analyzing the (311) reflection. Using this approach, a typical creep curve was obtained from the analysis of the time dependence of the separation of two (311) reflections. The secondary creep behavior, characterized by a constant strain rate, can be seen from the starting point to ~200 minutes. Primary creep cannot be clearly identified due to rapid deformations resulting from the high temperatures and large applied stresses in the experiment. Following secondary creep, tertiary creep was observed with an increased strain rate. Failure occurred at ~5 hours.

In addition to creep strain measurements, X-ray data allow for an assessment of the microstructure development. The shape of a diffraction peak changes during material deformation, which is called "X-ray line broadening" [113]. The diffraction peak broadening, demonstrated by the full width at half maximum (FWHM), is determined by the distribution of randomly oriented lattice plane distances (or lattice parameters) if the instrumentation factors are constant [149]. For plastic deformation, the typical origins for changing the FWHM are crystalline size and micro distortion/strain. Fig. 5.27(a) shows the time-dependence of the macroscopic creep strain and the relative width of the (311) reflection. During the early creep stage, the FWHM of the (311) reflection decreases in contrast to the fact that the macroscopic creep strain increases. As the creep progresses, the FWHM reaches a static level during the secondary creep stage. After ~2hours at a static level, the FWHM increases until the tube fracture occurs.

Another method used to explore the microstructure development is to measure lattice strain development deduced from the shifts of diffraction peaks. The procedures used to analyze microscopic lattice strain are similar to the ones used in the *in-situ* tensile studies described in section 5.1. Due to a similar stress state for both sides of the creep tube, both Debye rings reflected from two sides were used for analysis in order to employ a longer X-ray path length (~0.5mm), and thus obtain more diffraction volume (~0.046mm^2), over which the average lattice strains were measured. The results from the lattice strain (radial direction)

analysis are shown in Fig. 5.27(b) in comparison to the measured macroscopic creep strain. Compared to the creep strain development, the deviation of lattice strain is small, on the range of 10^{-4}. The average measured lattice strain, ε, is 6.5×10^{-4}, corresponding to an internal radial stress of ~126MPa (E^{311} is ~193GPa). The measured radial stress is slightly lower than the expected hoop stress of 150MPa following the thin-wall assumption. It should be noted that an increasing lattice strain occurred at the moment of ~180 minutes after initializing the creep test. The average strain is ~5.4×10^{-4} (corresponding to 105MPa internal stress) before this transient moment, and it increases to a mean strain of 7.2×10^{-4} (corresponding to 139MPa internal stress) by the end of the test.

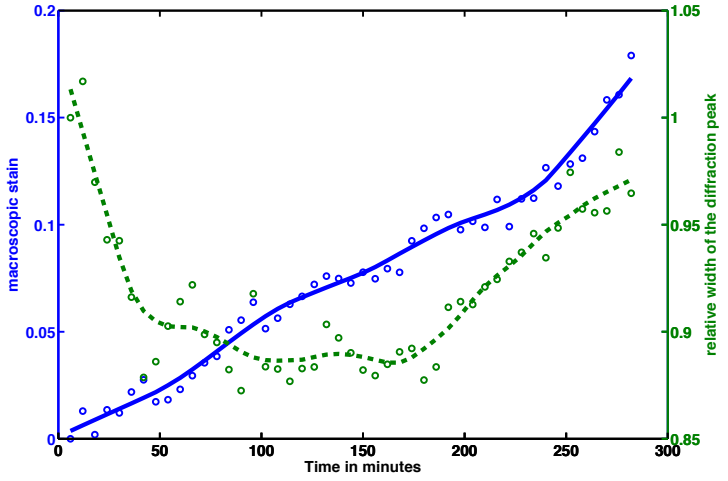

(a)

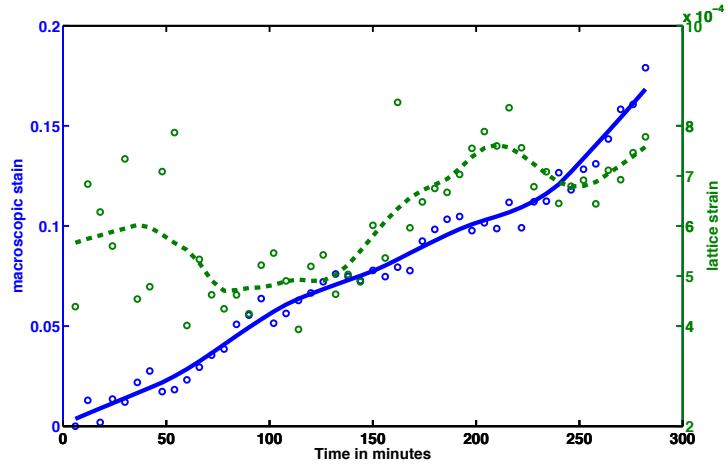

(b)

Fig. 5.27. Results of creep analysis: (a) time-dependence of the macroscopic creep strain (in blue) and the relative width of the (311) reflection (in green) (b) time-dependence of the macroscopic creep strain (in blue) and the lattice strain (in green). The solid and dash lines are curves fitted though the data points to show the trend.

5.3.3 DISCUSSION OF THE CREEP TUBE EXPERIMENT

From the analysis of diffraction patterns from pressurized creep tubes, a complete creep curve is obtained with a better continuity compared to interrupted strain measurements employed in previous studies. [156] This method also allows for an assessment of the *in-situ* microstructure development during different creep stages. First, the range of local strains and the crystalline size can be evaluated from analyzing peak broadening. Since the effective crystalline size remains relatively constant during creep, the peak width development can be considered to be generally caused by the local strain or undirected micro distortion. [113, 121, 149] From the analysis, the three-stage peak width development was observed. During the early stage, the FWHM of the (311) reflection decreased and reached a static level in ~60 minutes. This indicates a decrease in dislocation density in the early stages of creep, which is caused by the rearrangement and recombination of dislocations. (Fig. 5.27(a)) The result agrees well with the creep study completed by Pyzalla et al. and suggests that small residual stresses may result during the manufacturing of the tube used in the present study. [121] The static level of the FWHM lasts for ~ 2 hours then increases until the tube fractures. This peak broadening is most likely attributed to the development of associated localized stress concentrations caused by the nucleation, growth and coalescence of a large volume of creep voids. These results could be used to provide a better division of the secondary and tertiary creep regimes.

The analysis of the diffraction peak shifting also showed that higher internal stresses are developed after 160 minutes, which is close to the moment when the diffraction peak starts broadening. Thus, despite a relatively large data variation due to small applied stresses, the results of lattice strain measurement agree well with the analysis of diffraction peak broadening and indicate that the onset of the accelerated development of creep voids occurs ~180mins after the start of the creep test.

This technique, which uses the combination of pressurized creep tubes and high-energy synchrotron X-rays, can be coupled with small angle X-ray scattering (SAXS) or X-ray tomography to more directly observe the initiation of plasticity-induced void formation.

[86] The multi-scale measurement and X-ray technique crossover can provide an insight into the creep deformation for prospective materials for nuclear energy development. Finally, it should be noted that the specimen configuration in the present study simulates the heat transport and exchange tubing and piping in the NGNP system. This paves the way for using synchrotron X-ray diffraction as a non-destructive method to investigate many components in practical engineering applications.

CHAPTER 6

CONCLUSION

Nuclear energy is considered to be a promising energy source for the future. If technical issues pertaining to structural materials for next generation reactors can be overcome, nuclear energy can become more economic and reliable with vast improvements in safety. Currently, material development and characterization of high-temperature materials stands as one of the leading challenges, and perhaps the most limiting factor, for the development and advancement of next generation reactors, particularly the VHTR. In this thesis work, fundamental material studies have been conducted for two of the most promising structural materials for the VHTR: Alloy 617 and Alloy 230. The objective of this work was to investigate the material performance (short-term tensile response and long-term aging development) for a high-temperature environment. In addition, this study employed an advanced measurement technique, high-energy synchrotron radiation, to investigate deformation processes (time-independent and time-dependent) during *in-situ* loading.

6.1 ALLOY PROPERTIES

The deformation mechanisms of Alloy 617 and Alloy 230 during tensile loading at temperatures up to 1000ºC were clarified using experimentation. At temperatures from 300 to 700ºC, the yield strength was found to be temperature independent as a result of additional strain hardening provided by *dynamic strain aging*. However, higher temperatures (>800ºC) activated additional deformation mechanisms, including dislocation creep and dynamic recrystallization, leading to a significant decrease in strength at 800ºC. Consequently, the fracture mechanisms changed from inclusion particle cracks at temperatures up to 700ºC to triple junction cracks from 800 to 1000ºC. A small number of recrystallized grains were observed in the highly strained area connected to triple junction cracks during the tensile tests completed at 800ºC. Dynamic recrystallization became predominant at 1000ºC. A large

number of fine grains were found to recrystallize in grain boundaries and interphase grain boundaries, particularly in the inclusion-rich area in the necking part of the specimen. So, it was found that high strain, large particles and small grains promote the formation of new grains. Additionally, EBSD analyses show that a steady state recrystallized microstructure at 1000ºC was never achieved, although the tensile strain was larger than 0.5 by the conclusion of testing.

The effect of orientation on the tensile properties of Alloy 617 was also analyzed. Lower material strengths were detected for specimens with non-zero angles of orientation with the long-transverse direction. The yield strength was found to considerably decrease once the loading direction deviated from the long-transverse direction, while the ultimate tensile strength was found to decrease with a linear trend from the long-transverse to the short-transverse direction. This mechanical anisotropy has a comparable impact on Alloy 617 for temperatures up to 1000ºC. The dependency of plastic deformation on loading orientation was analyzed through several microstructural examinations. The results show that mechanical fibering, consisting of an alignment of inclusion particles and matrix crystals, is responsible for the mechanical anisotropy of Alloy 617 with varying performance across the studied temperature range. At low temperatures (<800ºC), Alloy 617 did not deform homogenously as a result of microstructure gradients. The inclusion rich area, seen as clusters from the rolling plane and bands from the transverse plane, could not be smoothly deformed, and thus the area developed high local strains under tensile load. The steep strain gradient in the short-transverse direction caused early fracture in the material, leading to a much lower tensile strength. At high temperatures (800-1000ºC), the highly strained areas caused by dislocation pileups at barriers (e.g. interphase boundaries) were subject to dynamic recrystallization. The orientation dependence of dynamic recrystallization with different dimensions and alignments of recrystallized grains results from the anisotropic spatial distribution of inclusion particles (i.e. mechanical fibering) in Alloy 617. This leads to an orientation dependence of mechanical properties at elevated temperatures.

Strain-rate sensitivity analysis for each alloy was conducted in order to approximate the long-term flow stresses. The *strain-rate sensitivities* for the 0.2% flow stress were found to be temperature independent ($m \approx 0$) at temperatures ranging from RT to 700ºC due to *dynamic strain aging*. At elevated temperatures (800-1000ºC), the *strain-rate sensitivity* significantly increased ($m > 0.1$). Compared to Alloy 617, Alloy 230 displayed higher *strain-rate sensitivities* at high temperatures. This leads to a lower estimated long-term flow stresses. Results of this analysis have also been used to evaluate current ASME allowable design limits. According to the comparison with the estimated flow stresses, the allowable design stresses for either alloy according to ASME B&PV Code did not provide adequate degradation estimation for the long-term service life. However, rupture stresses for Alloy 617, developed in ASME code case N-47-28, can generally satisfy the safety margin estimated in the study following the strain-rate sensitivity analysis. Nevertheless, additional material development studies must be completed, since the design parameters for rupture stresses are constrained such that current VHTR conceptual designs cannot satisfy the limits.

6.2 THERMAL AGING DEVELOPMENT

The thermal degradation processes for Alloy 617 and Alloy 230 was analyzed through long-term, high-temperature aging experiments. A similar microstructure evolution characterized by particle nucleation and growth was observed in each alloy. Fine and semi-coherent $M_{23}C_6$ precipitates nucleated in the early stage of aging and provided additional particle strengthening for each alloy. With further aging, large intergranular particles continued to grow at the expense of fine, intragranular precipitates. After long-term aging (>1000 hours), these fine precipitates had diffused and coarsened in high angle grain boundaries and interphase boundaries due to their high interfacial free energy. For the same reason, the carbide precipitates located in twin boundaries during the early stage of aging were depleted. Despite significant volume gain, most intergranular particles grown during thermal aging were found to maintain a cube-on-cube orientation with the γ matrix after aging for over 1000 hours.

The kinetics of microstructure development was also investigated by dimension measurements and coarsening-rate analysis of intergranular particles. At both 900 and 1000ºC, most volume gain (by fraction) of intergranular particles occurred during the early stage of aging. After this early development, the growth rate decreased with time. The intergranular particle growth and associated growth rate development were controlled by thermal aging temperature. Due to a lower equilibrium volume fraction of carbides at 900ºC, particle nucleation was completed in a short period of time (<<10 hours). Hence, the following microstructural development was dominantly characterized by particle coarsening. In contrast, a mixed process incorporating particle nucleation and growth was observed in the aging process at 1000ºC due to a higher equilibrium volume fraction of carbides. Additionally, heterogeneous elements (e.g. C, W or Mo) that form the intergranular particles obtained a higher diffusibility at higher temperatures. Therefore, larger intergranular particles were found in specimens aged at 1000ºC compared to specimens aged at 900ºC.

Results of mechanical tests were in good agreement with microstructure observations. Both the hardness measurements and tensile tests showed a typical aging process characterized by short-term strengthening and long-term softening. Generally, both alloys that were aged at 900ºC attained higher yield and tensile strengths with a longer hardening time compared to samples aged at 1000ºC. This agrees well with the completed microstructural analysis and suggests a more intense diffusion process at higher temperatures, so that precipitate hardening can only be maintained for a relatively short time period. Alloy 230 exhibited a longer effect of age-hardening compared to Alloy 617. The difference in duration of strengthening can be attributed to the diffusibility of main heterogeneous elements in the alloys. The diffusibility of W in Alloy 230 is lower compared to Co and Mo in Alloy 617, and this results in a relatively slower process of precipitate growth. The strengthening by fine particles within the γ matrix can therefore be maintained for a longer time in Alloy 230. Material softening after long-term aging resulted in a loss of strength in specimens aged at all studied temperatures (RT to 1000ºC). Analogous to the analysis on orientation effect, the

long-term aging degradation for high-temperatures tensile properties was found to be comparable to the degradation for low-temperatures properties.

During thermal aging of Alloy 617 and Alloy 230, no significant changes in grain boundary character distribution or grain size distribution were observed in either alloy. The exceptional thermal stability for both alloys is partially attributed to 'Zener pining' by large intrinsic carbides and age-coarsened intergranular particles. These particles inhibit the grain boundary migration and impede grain growth during aging. Hence, grain boundary character is preserved. In addition, even though σ phase is predicted from the calculated equilibrium phase diagram, this phase is not observed during the aging experiment. This finding agrees with all previous experimental studies and suggests that TCP phases will not be a significant threat for both alloys.

6.3 SYNCHROTRON RADIATION STUDY

With recent developments in synchrotron radiation techniques, various fundamental materials questions that have been difficult to answer using traditional destructive examinations have received solutions, in some cases by using a single X-ray exposure. However, nuclear material research is a relatively new area to implement synchrotron radiation study. In this thesis work, high-energy synchrotron X-ray diffraction was applied to study the tensile response of Alloy 230. The lattice strain response for reflections from the γ matrix was found to be nearly linear with the external applied stress. Thus, the lattices strain/internal stress conversion becomes straightforward based on the elastic, self-consistent Kröner's method. The γ matrix of Alloy 230 in both the long- and short-transverse direction experienced a similar process of lattice strain development during tensile loading, although the short-transverse specimen possesses a shorter elongation due to an early failure. The Bauschinger effect seen in Alloy 230 specimens can be measured from the difference in residual stresses, which agrees well with results of mechanical testing.

Due to the large particle size and small volume fractions, M_6C carbides in Alloy 230 have a limited loading capacity. By increasing the external applied stress in the long-

transverse specimen, the lattice stain of the carbide decreases as a result of the continued fracture process observed during plastic deformation in the material. The maximum internal stress of the particle was achieved during early yielding of the material and can be defined as the critical fracture stress for the M_6C type carbide in Alloy 230. This critical value was found to be ~1344 MPa corresponding to a lattice strain of ~0.0047. The analysis on the short-transverse specimen further confirms this conclusion and suggests that the critical fracture stress is independent of loading orientation.

In addition to tensile experiments, a unique analysis technique was developed in this work to characterize the *in-situ* deformation response of pressurized creep tubes at elevated temperatures. The technique allows the macroscopic creep strain and the microstructural development to be measured simultaneously during a single X-ray exposure. A typical creep curve with identifiable secondary and tertiary creep response was obtained by analyzing the X-ray diffraction patterns. Additionally, *in-situ* observations of the development of dislocation structures and lattice strain during deformation make it possible to track the development of creep void nucleation, growth and coalescence. This technique, which uses a combination of pressurized creep tubes and high-energy synchrotron X-rays, can be used with small angle X-ray scattering (SAXS) to more directly observe the initiation of plasticity-induced void formation. Finally, it should be noted that the specimen configuration in the present study simulates the heat transport and exchange tubing and piping in the VHTR system. This study paves the way for using synchrotron X-ray diffraction as a non-destructive method to investigate components in practical engineering applications.

CHAPTER 7

FUTURE WORK

Although both Alloy 617 and Alloy 230 have been actively studied in a number of programs, these metallic alloys have strength limitations at very high temperature (discussed in Chapter 2, 3 & 4), which compromises their use under the extreme environments of the VHTR. A major reason for these limitations is the thermal instability of the strengthening agents in these materials. As discussed in Chapter 4, both of the lead alloy systems are strengthened with metal-carbide type precipitates which coarsen rapidly and change the structure at the expense of solid-solution elements at high temperatures. So, the overall strength decreases with aging time. This limitation can be overcome by employing another strengthener, oxide dispersion, into the Ni alloying system. Ni-based oxide dispersion strengthened alloys (ODS) can provide duplex benefits that cannot be achieved by either Ni-based superalloys (including γ' strengthened or solid-solution strengthened) or iron-based ODS alloys: very-high-temperature strength and creep/creep-fatigue resistance (problematic for Ni-based superalloys) with very-high-temperature corrosion resistance (problematic for iron-based ODS alloys). Oxide particles differ from precipitates in that they are thermally stable up to temperatures near their melting points which are typically much higher than the melting ranges of the metal matrix materials in which they are embedded. Thus, ODS alloys will not suffer a loss of particle strengthening during long-term thermal aging. In fact, Ni-based ODS alloys may be the only serviceable metallic structural materials able to withstand the very-high-temperature system for a long service life. In future studies, a focus will be placed on the application of synchrotron radiation to characterize and develop the Ni-based ODS alloys.

To date, the exact nature of the oxide particles remains unclear. In order to develop suitable ODS alloys and optimize their chemical compositions for the VHTR environment, it is necessary to investigate the essential characteristics of ODS materials (carbide particles,

precipitates, nano-clusters, crystallines, nanofeatures, etc.) as well as their response to applied stress. High-energy X-ray diffraction provides a unique method for directly and continuously measuring the lattice strains for various phases (carbide, oxide particles and host matrix) in various crystallographic orientations during *in-situ* tensile tests. The stress or load transfer for different phases can be directly determined based on measurements of elastic mismatch, matrix plasticity, interface decohesion and even particle fracture. Moreover, small-angle X-ray scattering can be employed to study the nano-particle distribution and void development during tensile loading. The mechanisms and kinetics by which the nano-clusters form under applied stress, as well as the structure, composition, and nanoscale characters can be elucidated through high-energy X-ray exposure. Current analysis methods for ODS alloys focus on small angle neutron scattering (SANX), transmission electron microscopy (TEM), and atom-probe-tomography (APT), yet none of these techniques reveal the dynamic processes for ODS materials during deformations. The future study will aim to provide new, unique insights into high-temperature deformation mechanisms of ODS alloys, including creep, creep-fatigue and creep-environment interaction. These mechanisms will be investigated based on the developed techniques presented in this thesis work: uniaxial tensile loading and biaxial pressurized creep tube with synchrotron X-ray exposure while adjusting the applied temperature, loading modes and exposure environment. This work will provide understanding of the fundamental material degradation of Ni-based ODS alloys in high-temperature, aggressive environments and evaluate whether Ni-based ODS alloys can replace the current lead Ni alloy systems (i.e. Alloy 617 and Alloy 230) with better material performance in the VHTR.

APPENDIX A: STRAIN-STRESS DIAGRAMS FOR ALLOY 617 AND ALLOY 230

The engineering strain-stress diagrams for Alloy 617 testing at three strain rates and various temperatures are given in Fig. A.1 to A.10.

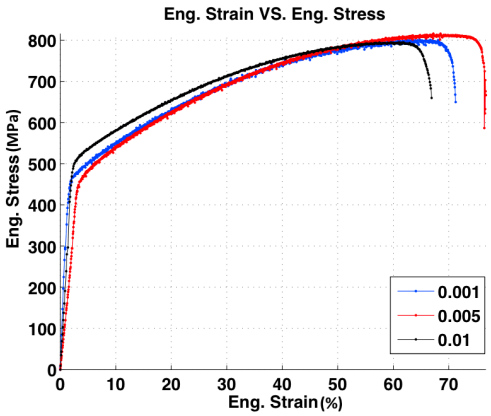

A.1. 100 ºC

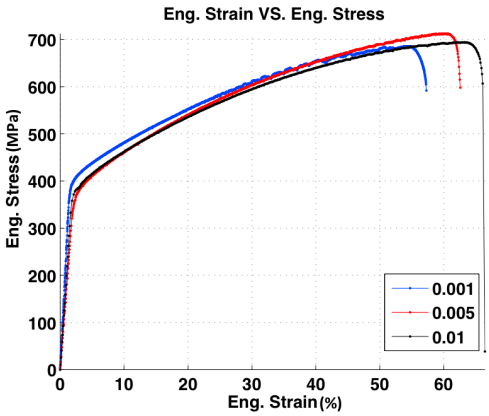

A.2. 200 ºC

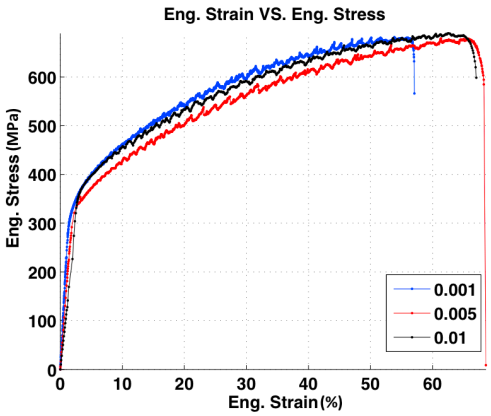

A.3. 300 ºC

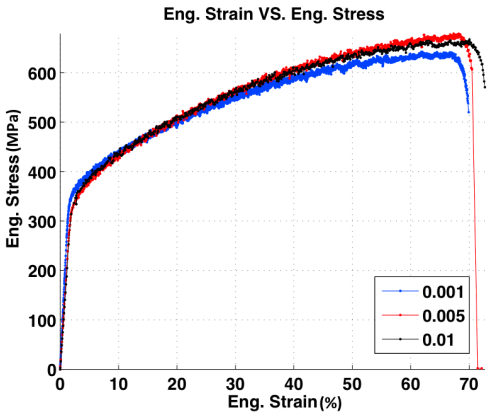

A.4. 400 ºC

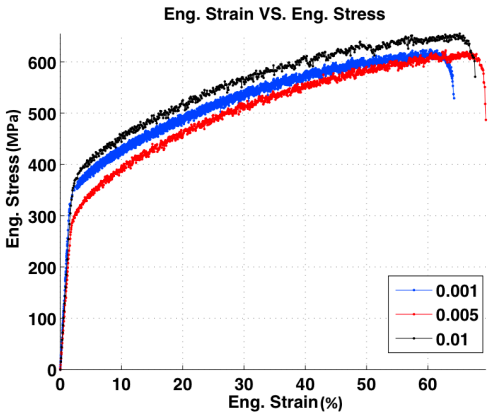

A.5. 500 ºC

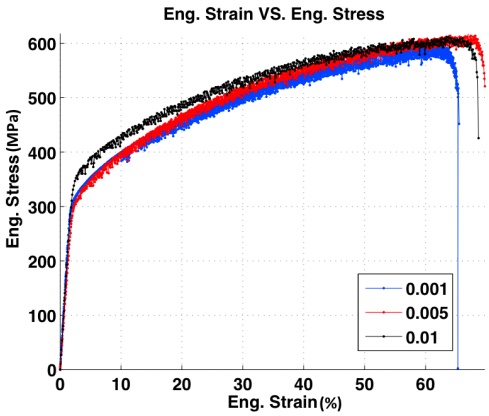

A.6. 600 ºC

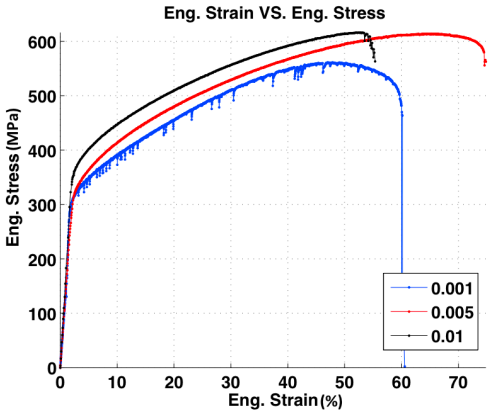

A.7. 700 ºC

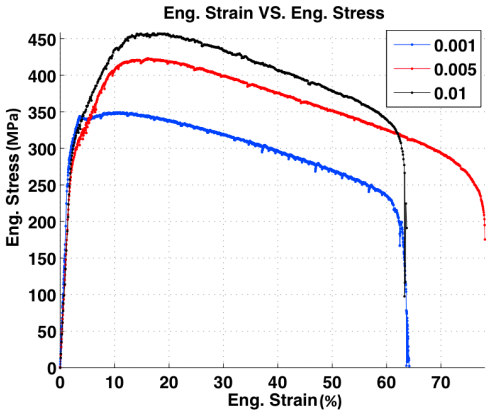

A.8. 800 ºC

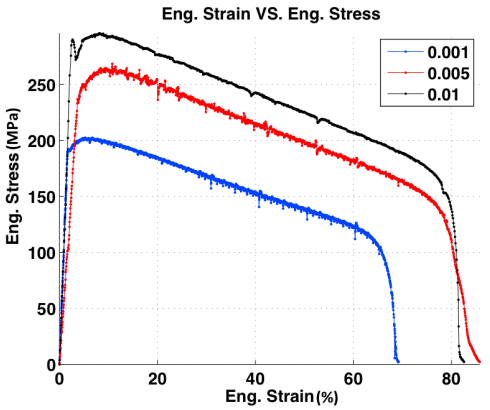

A.9. 900 ºC

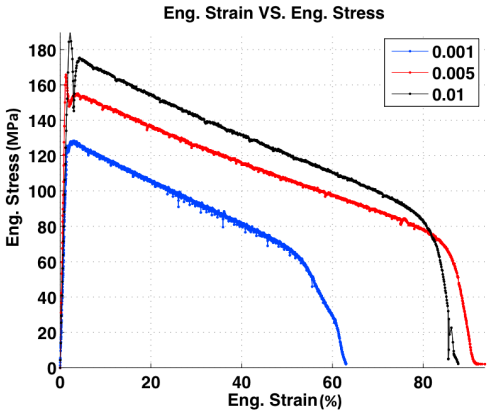

A.10. 1000 ºC

The engineering strain-stress diagrams for Alloy 230 testing at three strain rates and various temperatures are given in Fig. A.11 to A20.

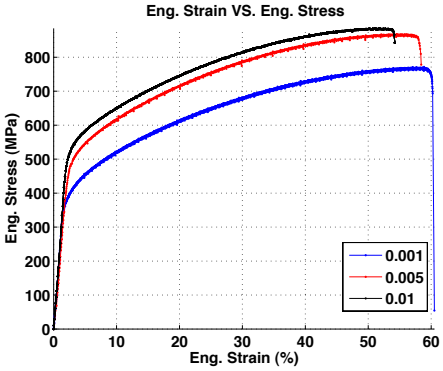

A.11. 100 ºC

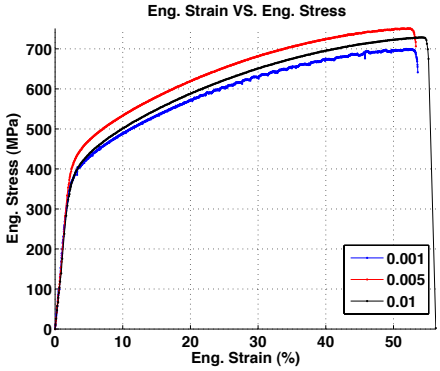

A.12. 200 ºC

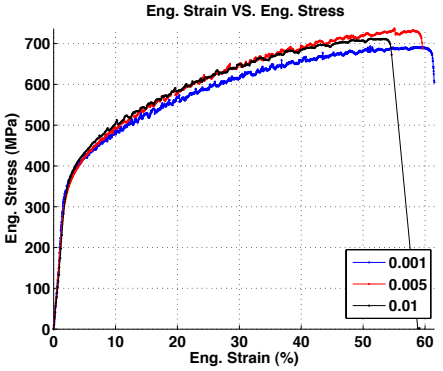

A.13. 300 ºC

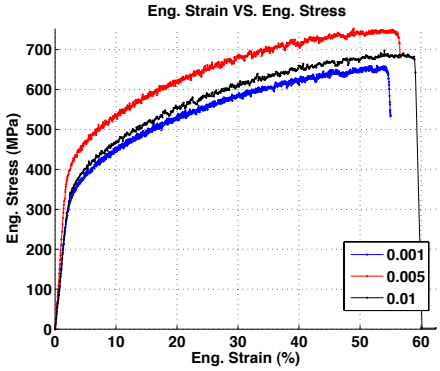

A.14. 400 ºC

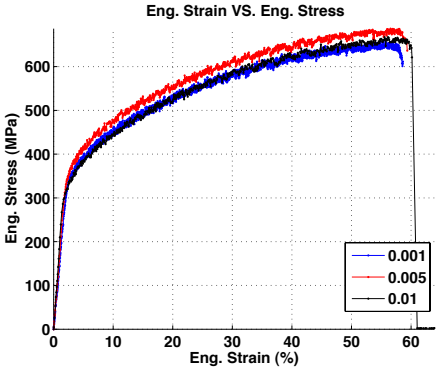

A.15. 500 ºC

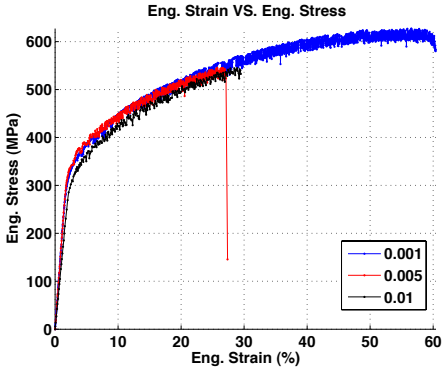

A.16. 700 ºC

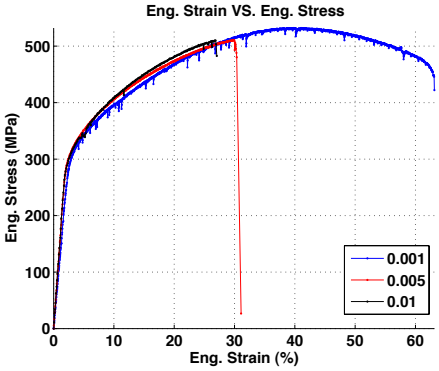

A.17. 700 ºC

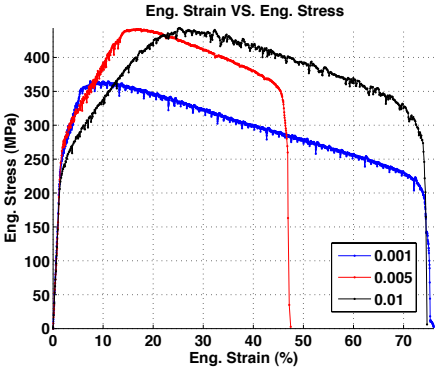

A.18. 800 ºC

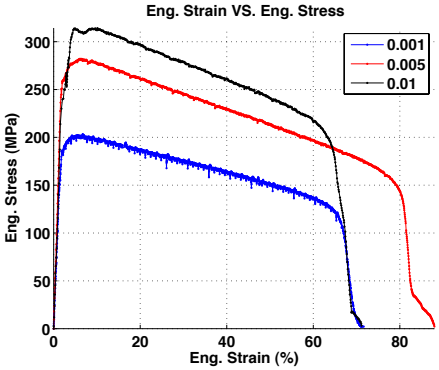

A.19. 900 ºC

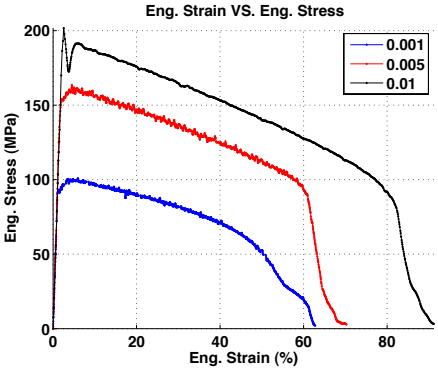

A.20. 1000 ºC

APPENDIX B: MODELING YOUNG'S MODULUS AND POISSON'S RATIO BASED ON VOIGT'S, REUSS'S & KRÖNER'S AVERAGES

```
load('MaterialData.mat')
Mater = 'W';

Study_spec_ref=1;

h =[2 3 2 1];
k =[0 1 2 1];
l =[0 1 0 1];

NumRef = length(h);

for i=1:NumRef
   Ahkl(i)=(h(i)^2*k(i)^2+k(i)^2*l(i)^2+l(i)^2*h(i)^2)/(h(i)^2+k(i)^2+l(i)^2)^2;
end

C11=0;
for i =1:length(Materials_Name)
   if strcmp(Materials_Name{i},Mater)
         C11 = SingleCrystalData(1,i);
         C44 = SingleCrystalData(2,i);
         C12 = SingleCrystalData(3,i);
         break
   end
end

if C11==0
  axis off
  text(0,0.5,'No such material in database','FontSize',18,'fontweight','b','color','r');
end

S44=1/C44;
S12=(-C12)/(C11+2*C12)/(C11-C12);
S11=1/C11+2*C12^2/(C11*(C11+2*C12)*(C11-C12));

i=0;
for AHKL=0:0.01:0.33
   i=i+1;
   Ehklv(i)=(2*S44+6*(S11-S12))/(2*S11*(S11+S12+2*S44)-2*S12*(2*S12+S44));
   vhklv(i)=-(S11*(2*S11+2*S12-S44)+S12*(3*S44-4*S12))/(2*S11*(S11+S12+2*S44)-
2*S12*(2*S12+S44));
end

for i=1:length(Ehklv)
   SS12v(i)=(1+vhklv(i))/Ehklv(i);
   SS1v(i)=-vhklv(i)/Ehklv(i);
end

if Study_spec_ref
   for i=1:NumRef
   EhklvSSR(i)=(2*S44+6*(S11-S12))/(2*S11*(S11+S12+2*S44)-2*S12*(2*S12+S44));
   vhklvSSR(i)=-(S11*(2*S11+2*S12-S44)+S12*(3*S44-4*S12))/(2*S11*(S11+S12+2*S44)-
2*S12*(2*S12+S44));
   SS12vSSR(i)=(1+vhklvSSR(i))/EhklvSSR(i);
   SS1vSSR(i)=-vhklvSSR(i)/EhklvSSR(i);
   end
end
```

```
Kv=1/3*(1/(S11+2*S12));
Miuv=(1/5)*(1/(S11-S12)+3/S44);
Miuvavg=(1/5)*(1/(S11-S12)+3/S44);
Ehklvavg=Ehklv(1);
vhklvavg=vhklv(1);

i=0;
for AHKL=0:0.01:0.33
   i=i+1;
   Ehklr(i) = 1/(S11-AHKL*(2*(S11-S12)-S44));
   vhklr(i) = -(S12+AHKL*((S11-S12)-S44/2))/(S11-AHKL*(2*(S11-S12)-S44));
end

for i=1:length(Ehklr)
   SS12r(i)=(1+vhklr(i))/Ehklr(i);
   SS1r(i)=-vhklr(i)/Ehklr(i);
end

if Study_spec_ref
   for i=1:NumRef
   EhklrSSR(i)=1/(S11-Ahkl(i)*(2*(S11-S12)-S44));
   vhklrSSR(i)=-(S12+Ahkl(i)*((S11-S12)-S44/2))/(S11-Ahkl(i)*(2*(S11-S12)-S44));
   SS12rSSR(i)=(1+vhklrSSR(i))/EhklrSSR(i);
   SS1rSSR(i)=-vhklrSSR(i)/EhklrSSR(i);
   end
end

Kr=Kv
Miuravg= 5/(4*(S11-S12)+3*S44);

Ehklravg=(9*Kv*Miuravg)/(3*Kv + Miuravg)
vhklravg = (3*Kv - 2*Miuravg)/(6*Kv + 2*Miuravg)

Tao=(C11-C12)/2;
Miu =C44;
Kk=(C11+2*C12)/3;
alpha1=(45*Kk+24*Miu+36*Tao)/40;
alpha2 = (2*Tao+3*Miu)/5;
beta1=3*Kk*(2*Miu+3*Tao)/20;
beta2=3*(6*Kk*Tao+9*Kk*Miu+20*Miu*Tao)/40;
gamma=3*Kk*Tao*Miu/4;

Miuk=0;
for i=1:300
Miuk= (alpha2*Miuk^2+beta2*Miuk+gamma)/(Miuk^2+alpha1*Miuk+beta1);
end
 t3333=1/(3*Miuk)*(2*Miuk*(S11-S12)-1)/(((8*Miuk^2+9*Kk*Miuk)/(6*Miuk+3*Kk)*(S11-
S12))+1);
t3311=-t3333/2;
t3131=-t3333/2;
t0=t3333-t3311-2*t3131;

i=0;
for AHKL=0:0.01:0.33
   i=i+1;
   SS1k(i)= 1/3*(1/3/Kk-1/2/Miuk)+t3311+t0*AHKL;
   SS12k(i)= 1/2/Miuk+t3333-t3311-3*t0*AHKL;
end

for i =1:length(SS1k)
```

```
vhklk(i)=-SS1k(i)/(SS1k(i) + SS12k(i));

Ehklk(i)=1/(SS1k(i) + SS12k(i));
end

if Study_spec_ref
   for i=1:NumRef
   SS1kSSR(i)=1/3*(1/3/Kk-1/2/Miuk)+t3311+t0*Ahkl(i);
   SS12kSSR(i)=1/2/Miuk+t3333-t3311-3*t0*Ahkl(i);
   vhklkSSR(i)=-SS1kSSR(i)/(SS1kSSR(i) + SS12kSSR(i));
   EhklkSSR(i)=1/(SS1kSSR(i) + SS12kSSR(i));
   end
end

Miukavg=Miuk;
Ehklkavg=(9*Kv*Miuk)/(3*Kv + Miuk)
vhklkavg = (3*Kv - 2*Miuk)/(6*Kv + 2*Miuk)
```

REFERENCES

[1] Leapfrogging the power grid, Nature. 427 (2004) 661-661.
[2] D. Butler, Energy: Nuclear power's new dawn, Nature. 429 (2004) 238-240.
[3] A Technology Roadmap for Generation IV Nuclear Energy Systems, in, U.S. DOE Nuclear Energy Research Advisory Committee and the Generation IV International Forum, 2002, pp. 50.
[4] Y. Guérin, G.S. Was, S.J. Zinkle, Materials Challenges for Advanced Nuclear Energy Systems, MRS BULLETIN. 34 (2009) 10-14.
[5] W.R. Corwin, T.D. Burchell, C.E. Duty, Y. Katoh, J.W. Klett, T.E. McGreevy, R.K. Nanstad, W. Ren, P.L. Rittenhouse, L.L. Snead, R.W. Swindeman, D.F. Wilson, Next Generation Nuclear Plant Materials Research and Development Program Plan, Revision 3, INL/EXT-06-11701. (2006).
[6] C.H. Oh, E.S. Kim, M. Patterson, Design Option of Heat Exchanger for the Next Generation Nuclear Plant, J Eng Gas Turb Power. 132 (2010) 032903.
[7] www.specialmetals.com.
[8] W.J. Ren, R. Swindeman, A Review on Current Status of Alloys 617 and 230 for Gen IV Nuclear Reactor Internals and Heat Exchangers, J Press Vess-T Asme. 131 (2009) 044002.
[9] W.J. Ren, R. Swindeman, A Review Paper on Aging Effects in Alloy 617 for Gen IV Nuclear Reactor Applications, J Press Vess-T Asme. 131 (2009) 024002.
[10] W. Ren, R. Swindeman, M. Santella, Developing a Nuclear Grade of Alloy 617 for Gen IV Nuclear Energy Systems, in: ICAPP '10, San Diego, CA, USA , 2010.
[11] J.C. Hosier, D.J. Tillack, Inconel Alloy 617 - New High-Temperature Alloy, Met Eng Quart. 12 (1972) 51-55.
[12] H.G.A. Bates, The Corrosion Behavior of High-Temperature Alloys during Exposure for Times up to 10000 H in Prototype Nuclear Process Helium at 700 ºC to 900ºC, Nucl Technol. 66 (1984) 415-428.
[13] L.W. Graham, Corrosion of Metallic Materials in Htr-Helium Environments, J Nucl Mater. 171 (1990) 76-83.
[14] H.J. Christ, U. Kunecke, K. Meyer, H.G. Sockel, Mechanisms of High-Temperature Corrosion in Helium Containing Small Amounts of Impurities .2. Corrosion of the Nickel-Base Alloy Inconel-617, Oxid Met. 30 (1988) 27-51.
[15] H.J. Christ, U. Kunecke, K. Meyer, H.G. Sockel, High-Temperature Corrosion of the Nickel-Based Alloy Inconel-617 in Helium Containing Small Amounts of Impurities, Mater Sci Eng. 87 (1987) 161-168.
[16] C. Jang, D. Lee, D. Kim, Oxidation behaviour of an Alloy 617 in very high-temperature air and helium environments, Int J Pres Ves Pip. 85 (2008) 368-377.
[17] C. Cabet, A. Terlain, P. Lett, L. Guetaz, J.M. Gentzbittel, High temperature corrosion of structural materials under gas-cooled reactor helium, Mater Corros. 57 (2006) 147-153.
[18] C. Cabet, J. Chapovaloff, F. Rouillard, G. Girardin, D. Kaczorowski, K. Wolski, M. Pijolat, High temperature reactivity of two chromium-containing alloys in impure helium, J Nucl Mater. 375 (2008) 173-184.
[19] C. Cabet, F. Rouillard, Corrosion of high temperature metallic materials in VHTR, J Nucl Mater. 392 (2009) 235-242.

[20] C. Cabet, F. Rouillard, Corrosion Issues of High Temperature Reactor Structural Metallic Materials, J Eng Gas Turb Power. 131 (2009) 062902.
[21] C. Cabet, J. Jang, J. Konys, P.F. Tortorelli, Environmental Degradation of Materials in Advanced Reactors, MRS BULLETIN. 34 (2009) 35-39.
[22] M.A. Harper, J.E. Barnes, G.Y. Lai, Long-Term Oxidation Behavior of Selected High Temperature Alloys, in: CORROSION 97, NACE, 2008, pp. Paper No. 132.
[23] R. Wright, Summary of Studies of Aging and Environmental Effects on Inconel 617 and Haynes 230, INL/EXT-06-11750. (2006) 39.
[24] F. Schubert, U. Bruch, R. Cook, H. Diehl, P.J. Ennis, W. Jakobeit, H.J. Penkalla, E. Teheesen, G. Ullrich, Creep-Rupture Behavior of Candidate Materials for Nuclear Process Heat Applications, Nucl Technol. 66 (1984) 227-240.
[25] H.J. Penkalla, F. Schubert, H. Nickel, Material Hardening under Multiaxial Creep Loading, Nucl Eng Des. 137 (1992) 355-362.
[26] S.K. Sharma, G.D. Ko, F.X. Li, K.J. Kang, Oxidation and creep failure of alloy 617 foils at high temperature, J Nucl Mater. 378 (2008) 144-152.
[27] A.K. Roy, M.H. Hasan, J. Pal, Creep deformation of Alloys 617 and 276 at 750-950ºC, Mat Sci Eng a-Struct. 520 (2009) 184-188.
[28] K. Schneider, W. Hartnagel, P. Schepp, B. Ilschner, Creep-Behavior of Materials for High-Temperature Reactor Application, Nucl Technol. 66 (1984) 289-295.
[29] S.K. Sharma, C. Jang, K.J. Kang, Effect of thermo-mechanical processing on microstructure and creep properties of the foils of alloy 617, J Nucl Mater. 389 (2009) 420-426.
[30] M. Cappelaere, M. Perrot, J. Sannier, Behavior of Metallic Materials between 550ºC and 870ºC in High-Temperature Gas-Cooled Reactor Helium under Pressures of 2-Bar and 50-Bar, Nucl Technol. 66 (1984) 465-478.
[31] H.M. Yun, P.J. Ennis, H. Nickel, H. Schuster, The Effect of High-Temperature Reactor Primary Circuit Helium on the Formation and Propagation of Surface Cracks in Alloy 800-H and Inconel-617, J Nucl Mater. 125 (1984) 258-272.
[32] P.S. Shankar, K. Natesan, Efffect of trace impurities in helium on the creep behavior of Alloy 617 for very high temperature reactor applications, J Nucl Mater. 366 (2007) 28-36.
[33] T. Lillo, J. Cole, M. Frary, S. Schlegel, Influence of Grain Boundary Character on Creep Void Formation in Alloy 617, Metall Mater Trans A. 40A (2009) 2803-2811.
[34] S. Schlegel, S. Hopkins, E. Young, J. Cole, T. Lillo, M. Frary, Precipitate Redistribution during Creep of Alloy 617, Metall Mater Trans A. 40A (2009) 2812-2823.
[35] H.M. Tawancy, D.L. Klarstrom, M.F. Rothman, Development of a New Nickel-Base Superalloy, Jom-J Min Met Mat S. 36 (1984) 58-62.
[36] http://www.haynesintl.com/.
[37] W.L. Mankins, J.C. Hosier, T.H. Bassford, Microstructure and Phase-Stability of Inconel Alloy 617, Metall Trans. 5 (1974) 2579-2590.
[38] H. Kirchhofer, F. Schubert, H. Nickel, Precipitation Behavior of Ni-Cr-22fe-18mo (Hastelloy-X) and Ni-Cr-22co-12mo (Inconel-617) after Isothermal Aging, Nucl Technol. 66 (1984) 139-148.
[39] S. Kihara, J.B. Newkirk, A. Ohtomo, Y. Saiga, Morphological-Changes of Carbides during Creep and Their Effects on the Creep-Properties of Inconel 617 at 1000ºC, Metall Trans A. 11 (1980) 1019-1031.
[40] Q.Y. Wu, H.J. Song, R.W. Swindeman, J.P. Shingledecker, V.K. Vasudevan, Microstructure of long-term aged IN617Ni-base superalloy, Metall Mater Trans A. 39A (2008) 2569-2585.

[41] M.L. Young, J. DeFouw, J.D. Almer, D.C. Dunand, Load partitioning during compressive loading of a Mg/MgB2 composite, Acta Materialia. 55 (2007) 3467-3478.
[42] M.L. Young, J.D. Almer, M.R. Daymond, D.R. Haeffner, D.C. Dunand, Load partitioning between ferrite and cementite during elasto-plastic deformation of an ultrahigh-carbon steel, Acta Materialia. 55 (2007) 1999-2011.
[43] S. Cheng, A.D. Stoica, X.L. Wang, Y. Ren, J. Almer, J.A. Horton, C.T. Liu, B. Clausen, D.W. Brown, P.K. Liaw, L. Zuo, Deformation Crossover: From Nano- to Mesoscale, Phys Rev Lett. 103 (2009) 035502.
[44] B. Jakobsen, H.F. Poulsen, U. Lienert, J. Almer, S.D. Shastri, H.O. Sorensen, C. Gundlach, W. Pantleon, Formation and subdivision of deformation structures during plastic deformation, Science. 312 (2006) 889-892.
[45] J. Almer, U. Lienert, R.L. Peng, C. Schlauer, M. Oden, Strain and texture analysis of coatings using high-energy x-rays, J Appl Phys. 94 (2003) 697-702.
[46] http://www.gen-4.org/.
[47] T. Allen, H. Burlet, R.K. Nanstad, M. Samaras, S. Ukai, Advanced Structural Materials and Cladding, MRS BULLETIN. 34 (2009) 20-27.
[48] R.E. Mizia, Next Generation Nuclear Plant Intermediate Heat Exchanger Acquisition Strategy, in, Idaho National Laboratory, 2008.
[49] K. Natesan, A. Purohit, S.W. Tam, Materials Behavior in HTGR Environments, NUREG_cr6824. (2003) 85.
[50] M.A. Burke, C.G. Beck, The High-Temperature Low-Cycle Fatigue Behavior of the Nickel-Base Alloy in-617, Metall Trans A. 15 (1984) 661-670.
[51] T.C. Totemeier, H.B. Tian, Creep-fatigue-environment interactions in INCONEL 617, Mat Sci Eng a-Struct. 468 (2007) 81-87.
[52] K.B.S. Rao, H. Schiffers, H. Schuster, H. Nickel, Influence of Time and Temperature-Dependent Processes on Strain Controlled Low-Cycle Fatigue Behavior of Alloy-617, Metall Trans A. 19 (1988) 359-371.
[53] A.K. Roy, V. Marthandam, Mechanism of yield strength anomaly of Alloy 617, Mat Sci Eng a-Struct. 517 (2009) 276-280.
[54] Y. Pan, K.H. Lang, D. Lohe, E. Macherauch, Cyclic Deformation and Precipitation Behavior of Nicr22co12mo9 during Thermal Fatigue, Physica Status Solidi a-Applied Research. 138 (1993) 133-145.
[55] J.D. Whittenberger, Effect of Long-Term 1093-K Exposure to Air or Vacuum on the Structure of Several Wrought Superalloys, J Mater Eng Perform. 2 (1993) 745-758.
[56] F.R. Chien, R. Brown, Cyclic Oxidation of Haynes-230 Alloy, J Mater Sci. 27 (1992) 1514-1520.
[57] H.M. Tawancy, High-temperature oxidation behavior of a wrought Ni-Cr-W-Mn-Si-La alloy, Oxid Met. 45 (1996) 323-348.
[58] D.M. Liu, R. Hu, J.S. Li, Y. Liu, H.E.H. Kou, H.Z. Fu, Isothermal Oxidation Behavior of Haynes 230 Alloy in Air at 1100ºC, Rare Metal Mat Eng. 37 (2008) 1545-1548.
[59] F. Rouillard, C. Cabet, K. Wolski, M. Pijolat, Oxide-layer formation and stability on a nickel-base alloy in impure helium at high temperature, Oxid Met. 68 (2007) 133-148.
[60] F. Rouillard, C. Cabet, K. Wolski, M. Pijolat, Oxidation of a chromia-forming nickel base alloy at high temperature in mixed diluted CO/H2O atmospheres, Corros Sci. 51 (2009) 752-760.

[61] F. Rouillaird, C. Cabet, K. Wolski, A. Terlain, M. Tabarant, M. Pijolat, F. Valdivieso, High temperature corrosion of a nickel base alloy by helium impurities, J Nucl Mater. 362 (2007) 248-252.
[62] D. Kim, C. Jang, W. Ryu, Oxidation Characteristics and Oxide Layer Evolution of Alloy 617 and Haynes 230 at 900ºC and 1100ºC, Oxid Met. 71 (2009) 271-293.
[63] Y.L. Lu, L.J. Chen, P.K. Liaw, G.Y. Wang, C.R. Brooks, S.A. Thompson, J.W. Blust, P.F. Browning, A.K. Bhattachary, J.M. Aurrecoechea, D.L. Klarstrom, Effects of temperature and hold time on creep-fatigue crack-growth behavior of HAYNES (R) 230 (R) alloy, Mat Sci Eng a-Struct. 429 (2006) 1-10.
[64] Y.L. Lu, L.J. Chen, G.Y. Wang, M.L. Benson, P.K. Liaw, S.A. Thompson, J.W. Blust, R. Browning, A.K. Bhattacharya, J.M. Aurrecoechea, D.L. Klarstrom, Hold time effects on low cycle fatigue behavior of HAYNES 230 (R) superalloy at high temperatures, Mat Sci Eng a-Struct. 409 (2005) 282-291.
[65] Y.L. Lu, P.K. Liaw, Y. Sun, G.Y. Wang, S.A. Thompson, J.W. Blust, P.F. Browning, A.K. Bhattacharya, J.M. Aurrecoechea, D.L. Klarstrom, Hold-time effect on the elevated-temperature crack growth behavior of solid-solution-strengthened superalloys, Acta Materialia. 55 (2007) 767-775.
[66] Y.L. Lu, P.K. Liaw, G.Y. Wang, M.L. Benson, S.A. Thompson, J.W. Blust, P.F. Browning, A.K. Bhattacharya, J.M. Aurrecoechea, D.L. Klarstrom, Fracture modes of HAYNES®230® alloy during fatigue-crack-growth at room and elevated temperatures, Mat Sci Eng a-Struct. 397 (2005) 122-131.
[67] Special Metals Corporation, Inconel 617, 2005, Publication Number: SMC-029.
[68] N. Kasai, M. Kakudo, X-ray Diffraction by Macromolecules, Springer, 2005.
[69] M.E. Fitzpatrick, A. Lodini, Analysis of Residual Stress by Diffraction using Neutron and Synchrotron Radiation, Taylor & Francis Inc., 2003.
[70] C.R.A. Catlow, X-ray diffraction from powders and crystallites, in Applications of Synchrotron Radiation, Blackie, Glasgow, 1990.
[71] P. Coppens, Synchrotron Radiation Crystallography, Academic Press, London, 1992.
[72] J. Pannetier, Time resolved experiments, in Neutron and Synchrotron Radiation for Condensed Matter Studies, Springer, Berlin, 1993.
[73] V. Srajer, T.Y. Teng, T. Ursby, C. Pradervand, Z. Ren, S. Adachi, W. Schildkamp, D. Bourgeois, M. Wulff, K. Moffat, Photolysis of the carbon monoxide complex of myoglobin: Nanosecond time-resolved crystallography, Science. 274 (1996) 1726-1729.
[74] A.C. Jupe, X. Turrillas, P. Barnes, S.L. Colston, C. Hall, D. Hausermann, M. Hanfland, Fast in situ x-ray-diffraction studies of chemical reactions: A synchrotron view of the hydration of tricalcium aluminate, Phys Rev B. 53 (1996) 14697-14700.
[75] M.I. Eremets, I.A. Trojan, S.A. Medvedev, J.S. Tse, Y. Yao, Superconductivity in hydrogen dominant materials: Silane, Science. 319 (2008) 1506-1509.
[76] E. Gregoryanz, L.F. Lundegaard, M.I. McMahon, C. Guillaume, R.J. Nelmes, M. Mezouar, Structural diversity of sodium, Science. 320 (2008) 1054-1057.
[77] W.L. Mao, H.K. Mao, P.J. Eng, T.P. Trainor, M. Newville, C.C. Kao, D.L. Heinz, J.F. Shu, Y. Meng, R.J. Hemley, Bonding changes in compressed superhard graphite, Science. 302 (2003) 425-427.
[78] W.L. Mao, H.K. Mao, Y. Meng, P.J. Eng, M.Y. Hu, P. Chow, Y.Q. Cai, J.F. Shu, R.J. Hemley, X-ray-induced dissociation of H2O and formation of an O-2-H-2 alloy at high pressure, Science. 314 (2006) 636-638.
[79] L.E. Levine, B.C. Larson, W. Yang, M.E. Kassner, J.Z. Tischler, M.A. Delos-Reyes, R.J. Fields, W.J. Liu, X-ray microbeam measurements of individual

dislocation cell elastic strains in deformed single-crystal copper, Nat Mater. 5 (2006) 619-622.
[80] B.C. Larson, W. Yang, G.E. Ice, J.D. Budai, J.Z. Tischler, Three-dimensional X-ray structural microscopy with submicrometre resolution, Nature. 415 (2002) 887-890.
[81] R.I. Barabash, G.E. Ice, W.J. Liu, O.M. Barabash, Polychromatic microdiffraction characterization of defect gradients in severely deformed materials, Micron. 40 (2009) 28-36.
[82] R.I. Barabash, G.E. Ice, M. Kumar, J. Ilavsky, J. Belak, Polychromatic microdiffraction analysis of defect self-organization in shock deformed single crystals, Int J Plasticity. 25 (2009) 2081-2093.
[83] M. Lambert, Diffuse scattering, in Neutron and Synchrotron Radiation for Condensed Matter Studies, Springer, Berlin, 1993.
[84] T.P. Russell, Small-angle scattering, in Handbook of Synchrotron Radiation, North-Holland, Amsterdam, 1991.
[85] C. Williams, Small angle scattering from solids and solutions, in Neutron and Synchrotron Radiation for Condensed Matter Studies, Springer, Berlin, 1993.
[86] X. Pan, X.L. Wu, X. Chen, K. Mo, J. Almer, D.R. Haeffner, J.F. Stubbins, Temperature and particle size effects on flow localization of 9-12%Cr ferritic/martensitic steel by in situ X-ray diffraction and small angle scattering, J Nucl Mater. 398 (2010) 220-226.
[87] X. Pan, X.L. Wu, K. Mo, X. Chen, J. Almer, J. Ilavsky, D.R. Haeffner, J.F. Stubbins, Lattice strain and damage evolution of 9–12%Cr ferritic/martensitic steel during in situ tensile test by X-ray diffraction and small angle scattering, J Nucl Mater. 407 (2010) 10-15.
[88] P.A. Bruhwiler, M. Barbezat, A. Necola, D.J. Kohls, O. Bunk, D.W. Schaefer, P. Potschke, Comparison of quasistatic to impact mechanical properties of multiwall carbon nanotube/polycarbonate composites, J Mater Res. 25 (2010) 1118-1130.
[89] L.E. Levine, G.G. Long, J. Ilavsky, R.A. Gerhardt, R. Ou, C.A. Parker, Self-assembly of carbon black into nanowires that form a conductive three dimensional micronetwork, Appl Phys Lett. 90 (2007) 014101.
[90] F. Zhang, J. Ilavsky, Ultra-Small-Angle X-ray Scattering of Polymers, Polym Rev. 50 (2010) 59-90.
[91] D.A. Baker, L. Pruitt, A. Bellare, Ultra-small angle X-ray scattering to detect fatigue damage in polymers, J Mater Sci Lett. 20 (2001) 1163-1164.
[92] A. Bistolfi, M.B. Turell, Y.L. Lee, A. Bellare, Tensile and Tribological Properties of High-Crystallinity Radiation Crosslinked UHMWPE, J Biomed Mater Res B. 90B (2009) 137-144.
[93] K.S. Simis, A. Bistolfi, A. Bellare, L.A. Pruitt, The combined effects of crosslinking and high crystallinity on the microstructural and mechanical properties of ultra high molecular weight polyethylene, Biomaterials. 27 (2006) 1688-1694.
[94] M.B. Turell, A. Bellare, A study of the nanostructure and tensile properties of ultra-high molecular weight polyethylene, Biomaterials. 25 (2004) 3389-3398.
[95] A.B. Hmelo, Nondestructive Evaluation of Millimeter Scale Engineered Structures Using Synchrotron X-Ray Microtomography, J X-Ray Sci Technol. 4 (1994) 290-300.
[96] B.P. Flannery, H.W. Deckman, W.G. Roberge, K.L. Damico, 3-Dimensional X-Ray Microtomography, Science. 237 (1987) 1439-1444.
[97] K.H.A. Janssens, F.C.V. Adams, A. Rindby, Microscopic X-ray Fluorescence Analysis, Jon Wiley & Sons, Chichester, 2000.

[98] V. Baryshev, G. Kulipanov, A. Skrinsky, X-ray fluorescent elemental analysis, in Handbook of Synchrotron Radiation, North-Holland, Amsterdam, 1991.
[99] S.G. Gurman, EXAFS and structural studies of glasses, in Applications of Synchrotron Radiation, Blackie, Glasgow, 1990.
[100] E.A. Stern, S.M. Heald, Basic principles and appllications of EXAFS, in Handbook of Synchrotron Radiation, North-Holland, Amsterdam, 1983.
[101] J.H. Hubbell, S.M. Seltzer, Tables of X-Ray Mass Attenuation Coefficients and Mass Energy-Absorption Coefficients, in, National Institute of Standards and Technology (NIST), 2007.
[102] D. Haeffner, High Energy X-rays Applicaitons, in, National School for Neutron and X-ray Scattering, Argonne National Lab, 2009.
[103] M.T. Hutchings, P.J. Withers, T.M. Holden, T. Lorentzen, Introduction to the characterization of residual stress by neutron diffraction, Taylor & Francis Group, LLC, 2005.
[104] J. Almer, M. Oden, G. Hakansson, Microstructure, stress and mechanical properties of arc-evaporated Cr-C-N coatings, Thin Solid Films. 385 (2001) 190-197.
[105] J. Almer, M. Oden, G. Hakansson, Microstructure and thermal stability of arc-evaporated Cr-C-N coatings, Philos Mag. 84 (2004) 611-630.
[106] J. Almer, M. Oden, L. Hultman, G. Hakansson, Microstructural evolution during tempering of arc-evaporated Cr-N coatings, J Vac Sci Technol A. 18 (2000) 121-130.
[107] C.C. Aydiner, D.W. Brown, N.A. Mara, J. Almer, A. Misra, In situ X-ray investigation of freestanding nanoscale Cu-Nb multilayers under tensile load, Appl Phys Lett. 94 (2009) 031906.
[108] C.C. Aydiner, D.W. Brown, A. Misra, N.A. Mara, Y.C. Wang, J.J. Wall, J. Almer, Residual strain and texture in free-standing nanoscale Cu-Nb multilayers, J Appl Phys. 102 (2007) 083514.
[109] E. Maire, A. Owen, J.Y. Buffiere, P.J. Withers, A synchrotron X-ray study of a Ti/SiCf composite during in situ straining, Acta Materialia. 49 (2001) 153-163.
[110] A. Wanner, D.C. Dunand, Synchrotron X-ray study of bulk lattice strains in externally loaded Cu-Mo composites, Metall Mater Trans A. 31 (2000) 2949-2962.
[111] J.D. Almer, S.R. Stock, Internal strains and stresses measured in cortical bone via high-energy X-ray diffraction, J Struct Biol. 152 (2005) 14-27.
[112] X. Pan, Tensile Fracture Mechansims of Ferritic/Martensitic Structural Materials, in: Department of Nuclear, Plasma and Radiological Engineering, University of Illinois at Urbana-Champaign, Urbana, 2008.
[113] I.C. Noyan, J.B. Cohen, Residual Stress, Measurement by Diffraction and Interpretation, Springer-Verlag, New York, 1987.
[114] R.W. Hertzberg, Deformation and fracture mechanics of engineering materials, 4th edition, John Wiley & Sons, New York, 1996.
[115] E. Macherauch, K. K.H., Origin, measurement and evaluation of residual stresses, in: Proceedings of the International Conference on Residual Stresses, Garmisch-Partenkirchen, FRG, 1986, pp. 167-174.
[116] R. Kurtz, Recent progress on development of vanadium alloys for fusion, J Nucl Mater. 329-333 (2004) 47-55.
[117] F. Sket, A. Isaac, K. Dzieciol, G. Sauthoff, A. Borbely, A.R. Pyzalla, In situ tomographic investigation of brass during high-temperature creep, Scripta Mater. 59 (2008) 558-561.
[118] F. Beckmann, R. Grupp, A. Haibel, M. Huppmann, M. Noethe, A. Pyzalla, W. Reimers, A. Schreyer, R. Zettler, In-situ synchrotron X-ray microtomography studies

of microstructure and damage evolution in engineering materials, Adv Eng Mater. 9 (2007) 939-950.
[119] F. Sket, K. Dzieciol, A. Isaac, A. Borbely, A.R. Pyzalla, Tomographic method for evaluation of apparent activation energy of steady-state creep, Mat Sci Eng a-Struct. 527 (2010) 2112-2120.
[120] K.S. Cheong, K.J. Stevens, Y. Suzuki, K. Uesugi, A. Takeuchi, The effects of microstructure on creep behaviour-A study through synchrotron X-ray tomography, Mat Sci Eng a-Struct. 513-14 (2009) 222-227.
[121] A. Pyzalla, B. Camin, T. Buslaps, M. Di Michiel, H. Kaminski, A. Kottar, A. Pernack, W. Reimers, Simultaneous tomography and diffraction analysis of creep damage, Science. 308 (2005) 92-95.
[122] L. Tan, K. Sridharan, T.R. Allen, R.K. Nanstad, D.A. McClintock, Microstructure tailoring for property improvements by grain boundary engineering, J Nucl Mater. 374 (2008) 270-280.
[123] M.S. Rahman, G. Priyadarshan, K.S. Raja, C. Nesbitt, M. Misra, Characterization of high temperature deformation behavior of INCONEL 617, Mech Mater. 41 (2009) 261-270.
[124] R.E. Reed-Hill, R. Abbaschian, Physical Metallurgy Principles, 3rd ed., CL-Engineering, 1991.
[125] G.E. Dieter, Mechanical Metallurgy, 3rd ed., McGraw-Hill, 1988.
[126] L. Tan, K. Sridharan, T.R. Allen, Effect of thermomechanical processing on grain boundary character distribution of a Ni-based superalloy, J Nucl Mater. 371 (2007) 171-175.
[127] F. Montheillet, J.-P. Thomas, Dynamic Recrystallization of Low Stacking Fault Energy Metals, Springer, Netherlands, 2004.
[128] T.S. Srivatsan, C.W. Meyers, J.T. Berry, A method for determining the tensile properties and anisotropy of aluminum alloys, Journal of Testing and evaluation. 15 (1987) 196-204.
[129] K. Mo, G. Lovicu, H.-M. Tung, X. Chen, J. Stubbins, In-plane anisotropy in microstructure and mechanical behavior of Alloy 617 following high temperature aging, in: TMS 2010 Supplemental Proceedings, Seattle, 2010, pp. 491-498.
[130] A. Day, P. Trimby, CHANNEL 5 Manual, HKL Technology, 2004.
[131] K. Mo, G. Lovicu, H.-M. Tung, X. Chen, J. Stubbins, high temperature aging and corrosion study on Alloy 617 and Alloy 230, J Eng Gas Turb Power. 133 (2011) 052908.
[132] K. Mo, G. Lovicu, H.-M. Tung, X. Chen, J. Stubbins, microstructural evolution of Alloy 617 and Alloy 230 following high temperature aging, in: ASME 2010 Pressure Vessels & Piping Division / K-PVP Conference, Bellevue, Washington, USA, 2010, 25847.
[133] H.Y. Hunsicker, New Graphic Method for Analysis of Hot Deformation and Effects on Directional Properties, T Metall Soc Aime. 245 (1969) 29.
[134] T.C. Totemeier, T.M. Lillo, Effect of orientation on the tensile and creep properties of coarse-grained INCONEL alloy MA754, Metall Mater Trans A. 36A (2005) 785-795.
[135] M.A. Meyer, K.K. Chawla, Mechanical Behavior of Materials, Cambridge University Press, New York, 2008.
[136] G.F.V. Voort, G.M. Lucas, E.P. Manilova, Metallography and Microstructures of Heat-Resistant Alloys, ASM Handbook. 9 (2004) 820–859.

[137] J.K. Benz, J.H. Kim, R.G. Ballinger, Effect of Oxygen Potential on Crack Growth in Alloys for Advanced Energy Systems, J Eng Gas Turb Power. 132 (2010) 102901.
[138] ASTM B 168–08, 2008.
[139] R. Mignogna, C. Dantonio, R. Maciag, Mukherje.K, Mechanical Behavior of 6063-Aluminum, Metall Trans. 1 (1970) 1771.
[140] http://cst-www.nrl.navy.mil/lattice/.
[141] K.H. Kuo, C.L. Jia, Crystallography of M23C6 and M6C Precipitated in a Low-Alloy Steel, Acta Metallurgica. 33 (1985) 991-996.
[142] N. Stoloff, Wrought and P/M Superalloys, ASM handbook.
[143] H.Y. Bi, H. Kokawa, Z.J. Wang, M. Shimada, Y.S. Sato, Suppression of chromium depletion by grain boundary structural change during twin-induced grain boundary engineering of 304 stainless steel, Scripta Mater. 49 (2003) 219-223.
[144] J.W. Christian, The Theory of Transformations in Metals and Alloys - Part I: Equilibrium and General Kinetic Theory, Pergamon, 1975.
[145] K.M. Ralls, T.H. Courtney, J. Wulff, Introduction to Materials Science and Engineering, John Wiley and Sons, New York, 1976.
[146] E. Gilbert, J. Bates, Dependence of irradiation creep on temperature and atom displacements in 20% cold worked type 316 stainless steel, J Nucl Mater. (1977) 204-209.
[147] J. Vitek, D. Braski, J. Horak, Effect of preinjected helium on the response of v-20ti pressurized tubes to neutron irradiation, J Nucl Mater. (1986) 982-986.
[148] H. Tsai, H. Matsui, M. Billone, R. Strain, D. Smith, Irradiation creep of vanadium-base alloys, J Nucl Mater. 258-263 (1998) 1471-1475.
[149] V. Hauk, Structural and Residual Stress Analysis by Nondestructive Methods, Elsevier, 1997.
[150] J.D. Eshelby, The Determination of the Elastic Field of an Ellipsoidal Inclusion, and Related Problems, Proc R Soc Lon Ser-A. 241 (1957) 376-396.
[151] H. Pottebohm, G. Neite, E. Nembach, Elastic Properties (the Stiffness Constants, the Shear Modulus and the Dislocation Line Energy and Tension) of Ni-Al Solid-Solutions and of the Nimonic Alloy Pe16, Mater Sci Eng. 60 (1983) 189-194.
[152] B. Clausen, T. Lorentzen, T. Leffers, Self-consistent modelling of the plastic deformation of FCC polycrystals and its implications for diffraction measurements of internal stresses, Acta Materialia. 46 (1998) 3087-3098.
[153] Y.F. Li, Y.M. Gao, Z.J. Fan, B. Xiao, Q.W. Yue, T. Min, S.Q. Ma, First-principles study on the stability and mechanical property of eta M3W3C (M=Fe, Co, Ni) compounds, Physica B-Condensed Matter. 405 (2010) 1011-1017.
[154] L. Mishnaevsky, U. Weber, S. Schmauder, Numerical analysis of the effect of microstructures of particle-reinforced metallic materials on the crack growth and fracture resistance, Int J Fracture. 125 (2004) 33-50.
[155] B. Clausen, T. Lorentzen, M.A.M. Bourke, M.R. Daymond, Lattice strain evolution during uniaxial tensile loading of stainless steel, Mat Sci Eng a-Struct. 259 (1999) 17-24.
[156] M. Li, T. Nagasaka, D. Hoelzer, M. Grossbeck, S. Zinkle, T. Muroga, K. Fukumoto, H. Matsui, M. Narui, Biaxial thermal creep of two heats of V4Cr4Ti at 700 and 800°C in a liquid lithium environment, J Nucl Mater. 367-370 (2007) 788-793.
[157] E.R. Gilbert, L.D. Blackburn, Creep Deformation of 20 Percent Cold-Worked Type 316 Stainless-Steel, J Eng Mater-T Asme. 99 (1977) 168-180.

AUTHOR'S BIOGRAPHY

Kun Mo was born in Guangzhou, Guangdong Province, P. R. China on August 11, 1981. He received his Bachelor of Science degree in Nuclear Engineering from Xi'an Jiaotong University in July 2004. He then received his Master of Science degree in Nuclear Engineering from Korea Advanced Institute of Science and Technology in July 2006. Kun then enrolled as a graduate student pursuing his Ph.D. in the department of Nuclear, Plasma and Radiological Engineering at the University of Illinois at Urbana-Champaign.